

AD-A150 123

PSEUDOSPECTRAL CALCULATIONS OF TWO-DIMENSIONAL  
 TRANSONIC FLOW (TASK 1) NU. (U) FLOW INDUSTRIES INC  
 KENT WA W H JOU ET AL. SEP 84 TN-215 AFOSR-TR-84-1174  
 F49620-82-C-0022 F/G 20/4

1/1

UNCLASSIFIED

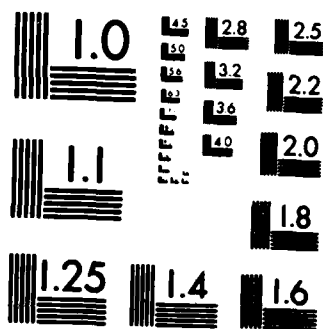
F/G 20/4

NL

44

END

• **MEMBER**



MICROCOPY RESOLUTION TEST CHART  
NATIONAL BUREAU OF STANDARDS 1963-A

AD-A150 123

AD-A150 123

3

Progress Report for  
Contract No. F49620-82-C-0022

**TASK 1. PSEUDOSPECTRAL CALCULATIONS OF TWO-  
DIMENSIONAL TRANSONIC FLOW**

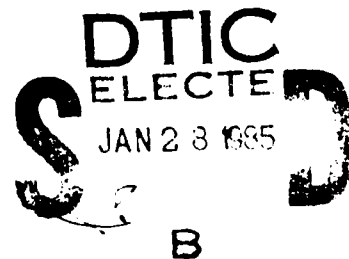
**TASK 2. NUMERICAL INVESTIGATION OF VTOL  
AERODYNAMICS**

September 1984

Submitted to  
Air Force Office of Scientific Research



Flow Industries, Inc.  
Research and Technology Division  
21414-68th Avenue South  
Kent, Washington 98032  
(206) 872-8500  
TWX: 910-447-2762



DISTRIBUTION STATEMENT A  
Approved for public release;  
Distribution Unlimited

# REPORT DOCUMENTATION PAGE

1a. REPORT SECURITY CLASSIFICATION UNCLASSIFIED			1b. RESTRICTIVE MARKINGS		
2a. SECURITY CLASSIFICATION AUTHORITY			3. DISTRIBUTION/AVAILABILITY OF REPORT Approved for Public Release; Distirbution Unlimited.		
2b. DECLASSIFICATION/DOWNGRADING SCHEDULE			4. PERFORMING ORGANIZATION REPORT NUMBER(S)		
5. MONITORING ORGANIZATION REPORT NUMBER(S) AFOSR-TR- 84-1174			6a. NAME OF PERFORMING ORGANIZATION FLOW INDUSTRIES, INC		
6b. OFFICE SYMBOL (If applicable)			7a. NAME OF MONITORING ORGANIZATION AFOSR/NA		
6c. ADDRESS (City, State and ZIP Code) RESEARCH & TECHNOLOGY DIVISION 21414 68th AVENUE SOUTH KENT, WA 98032			7b. ADDRESS (City, State and ZIP Code) Bolling AFB, DC 20332		
8a. NAME OF FUNDING/SPONSORING ORGANIZATION AIR FORCE OFFICE OF SCIENTIFIC RESEARCH		8b. OFFICE SYMBOL (If applicable) AFOSR		9. PROCUREMENT INSTRUMENT IDENTIFICATION NUMBER F49620-82-C-0022	
8c. ADDRESS (City, State and ZIP Code) BOLLING AFB, DC 20332		10. SOURCE OF FUNDING NOS.			
		PROGRAM ELEMENT NO. 61102F		PROJECT NO. 2307	TASK NO. A1
				WORK UNIT NO.	
11. TITLE (Include Security Classification) TASK 1. PSEUDOSPECTRAL CALCULATIONS OF TWO-DIMENSIONAL TRANSONIC FLOW TASK 2. NUMERICAL INVESTIGATION OF VTOL AERODYNAMICS (UNCLASSIFIED)					
12. PERSONAL AUTHOR(S) JOU, WEN-HUEI: METCALFE, R W					
13a. TYPE OF REPORT FINAL		13b. TIME COVERED FROM 22DEC81 TO 21DEC83		14. DATE OF REPORT (Yr., Mo., Day) 1984, September	
15. PAGE COUNT 54					
16. SUPPLEMENTARY NOTATION					
17. COSATI CODES			18. SUBJECT TERMS (Continue on reverse if necessary and identify by block number)		
FIELD	GROUP	SUB. GR.	TRANSONIC FLOW		
			SPECTRAL METHODS		
			JET IMPINGING FLOWS		
19. ABSTRACT (Continue on reverse if necessary and identify by block number) The status of the research performed under AFOSR contract F49620-82-C-0022 is reported in two Flow Research Technical Notes. "Pseudospectral Calculations of Two-Dimensional Transonic Flow" and "A Numerical Investigation of VTOL Aerodynamics." The formulation of the problem, the method of solution, and numerically obtained results are presented for each case.					
20. DISTRIBUTION/AVAILABILITY OF ABSTRACT UNCLASSIFIED/UNLIMITED <input checked="" type="checkbox"/> SAME AS RPT. <input type="checkbox"/> DTIC USERS <input type="checkbox"/>			21. ABSTRACT SECURITY CLASSIFICATION UNCLASSIFIED		
22a. NAME OF RESPONSIBLE INDIVIDUAL Dr James D Wilson			22b. TELEPHONE NUMBER (Include Area Code) 202/767-4935		22c. OFFICE SYMBOL AFOSR/NA

# Foreword

The year-end progress on Contract No. F49620-82-C-0022 for the Air Force Office of Scientific Research is reported in this document. The work for Task 1 is described in "Pseudospectral Calculations of Two-Dimensional Transonic Flow," Technical Note No. 215, which is provided first. A description of the Task 2 work, "A Numerical Investigation of VTOL Aerodynamics," Technical Note No. 216, is included next.

Accession For	
NTIS GRA&I	<input checked="" type="checkbox"/>
DTIC TAB	<input type="checkbox"/>
Unannounced	<input type="checkbox"/>
Justification	
By	
Distribution/	
Availability Codes	
Dist	Avail and/or Special
A-1	

AIR FORCE OFFICE OF SCIENTIFIC RESEARCH (AFSC)  
 NOTICE OF TRANSFER OF RIGHTS  
 This technology is being transferred and is  
 approved for release under the provisions of  
 Distribution Category A-190-12.  
 MATTHEW J. H. [illegible]  
 Chief, Technical Information Division



PSEUDOSPECTRAL CALCULATIONS OF  
TWO-DIMENSIONAL TRANSONIC FLOW\*

by  
Wen-Huei Jou  
R. W. Metcalfe

September 1984

\*This work is supported by the Air Force Office of Scientific Research and the  
Office of Naval Research under Contract No. F49620-82-C-0022.

Table of Contents

	Page
List of Figures	ii
1. Introduction	1
2. Basic Approach	2
2.1 Governing Equations	2
2.2 Numerical Scheme	2
2.3 Filtering	3
2.4 Boundary Conditions	4
2.5 Convergence Acceleration	5
3. Computed Results for Hybrid Scheme	7
4. Full Spectral Scheme	9
5. Conclusions	11
References	12
Figures	13
Appendix: Pseudospectral Calculations of Two-Dimensional Transonic Flow	17

List of Figures

	Page
Figure 1. Pressure Distribution for a Subcritical Flow Over a Cylinder at Mach 0.39	13
Figure 2. Pressure Distribution for a Supercritical Flow Over a Cylinder at Mach 0.45	14
Figure 3. Pressure Distribution on a Karman-Trefftz Airfoil at Mach 0.75 Using a 64x24 Grid (350 Steps)	15
Figure 4. Comparison of Results with a Finite Volume Scheme for a Karman-Trefftz Airfoil at Mach 0.75	16



## 1. Introduction

In recent years, there has been strong interest in applying pseudospectral methods to various flow problems. Some examples of these applications are collected in a recently published book by Voight, Gottlieb, and Hussaini (1984). One of the current areas of interest is the calculation of compressible flows with shock waves. Gottlieb, Lustman, and Orszag (1981) have investigated the one-dimensional shock tube problem using a pseudospectral method and reported the ability of capturing the shock within one grid point. Gottlieb, Lustman, and Streett (1982) have reported work on two problems in this area. The first is the solution of Euler equations for oblique shock reflection from a flat plate. By using a sparse  $8 \times 8$  computational grid, they have shown that it is possible to capture the shock wave within one grid point and that the treatment of boundary conditions is extremely crucial to the construction of a stable scheme. The second problem is the solution of a full potential equation for transonic flow past an airfoil. An airfoil is mapped to a circle. In the circumferential direction, a Fourier series is used, while Chebyshev expansion is used in the radial direction. In order to stabilize the calculation, an artificial viscosity is used in the governing equation. Gottlieb et al. (1982) has shown that in a subsonic flow, a highly accurate solution can be obtained by using a sparse grid of  $32 \times 8$  grid points. In the transonic case with shocks, the shock wave spans across three grid points and, hence, is not accurate enough if a sparse grid is used. The problem chosen by Gottlieb et al. (1982) for the solution of the Euler equations is, unfortunately, not a good one. The region between the oblique shock is a constant state. Aside from capturing the shock wave, their research yields no information about the accuracy of the method in the region of smooth variation away from the shock wave. Their work on potential flows has shown that the incorporation of conventional artificial viscosity into the spectral method will cause deterioration of the accuracy and thus defeat the purpose of using a spectral method.

In the present work, we have chosen the realistic problem of transonic flow over an airfoil to study the application of a spectral method to compressible flows with shock waves. Part of the findings of the present work have been reported in a conference paper (Jou, Jameson, and Metcalfe, 1983), which is included in this report as an appendix.

## 2. Basic Approach

### 2.1 Governing Equations

The basic approach is to map the exterior of an airfoil to the interior of a circle. Polar coordinates in the mapped plane will be used. Spectral decomposition of the solution can be used in the mapped plane. To serve this purpose, the Euler equations in the mapped plane are written in fully conservative form by using both physical and contravariant velocities. These equations are

$$\frac{\partial}{\partial t} (\vec{q}) + \frac{\partial}{\partial X} (\vec{F}) + \frac{\partial}{\partial Y} (\vec{G}) = 0 \quad (1)$$

where

$$\vec{q} = J \begin{bmatrix} \rho \\ \rho u \\ \rho v \\ E \end{bmatrix}; \quad \vec{F} = \begin{bmatrix} \rho U \\ \rho u U + y_Y P / \gamma M_\infty^2 \\ \rho v U - x_Y P / \gamma M_\infty^2 \\ \rho H U \end{bmatrix}; \quad \vec{G} = \begin{bmatrix} \rho V \\ \rho u V - y_X P / \gamma M_\infty^2 \\ \rho v V + x_X P / \gamma M_\infty^2 \\ \rho H V \end{bmatrix};$$

$$\begin{bmatrix} U \\ V \end{bmatrix} = \begin{bmatrix} y_Y & -x_Y \\ -y_X & x_X \end{bmatrix} \begin{bmatrix} u \\ v \end{bmatrix}; \quad H = [(\gamma - 1)P + E]/\rho;$$

(x,y) are Cartesian coordinates in the physical plane, (X,Y) are polar coordinates in the mapped plane,  $\rho$  is the density, (u,v) are velocity components, (U,V) are unscaled contravariant velocity components, E is the energy, H is the specific enthalpy, P is the pressure, J is the Jacobian of the transformation,  $M_\infty$  is the free-stream Mach number, and  $\gamma$  is the specific heat ratio. P,  $\rho$ , and the velocity vector (u,v) are nondimensionalized by their values at the free-stream condition, E and H are nondimensionalized by the free-stream internal energy  $\rho_\infty C_v T_\infty$ , and other variables at the free-stream condition are computed from these variables.

The physical boundary conditions are defined by the solid-wall condition on the airfoil surface and the fact that the disturbances generated by the airfoil propagate outward to infinity. The numerical implementation of these physical boundary conditions will be discussed later.

### 2.2 Numerical Scheme

A computational mesh is created by equally dividing the (X,Y) coordinates in the mapped plane. In the mapped plane, the spatial derivatives in X at

each mesh point are evaluated by application of a fast Fourier transform. The derivatives in Y are evaluated by second-order central finite differences. Evaluation of the elements in the transformation matrices  $(x_X, x_Y, y_X, y_Y)$  is performed in the same manner. The singularity of the transformation at the trailing edge is avoided by placing it between two mesh points.

By using this method of evaluating spatial derivatives, the governing equations are converted to a system of ordinary differential equations in time. These equations can be solved numerically by using any of a variety of well-developed techniques for the solution of ordinary differential equations. An approximate fourth-order Runge-Kutta scheme is used in this work. The algorithm is given by the following equations:

$$\vec{q}^{(n)} = \vec{q}^0 + \frac{1}{(5-n)} \vec{R}^{(n-1)} ; n = 1, \dots, 4 \quad (2)$$

where  $\vec{q}$  represents the flow variables at the mesh points,  $\vec{R}$  represents the terms with spatial derivatives in the equations, and  $n$  denotes the Runge-Kutta step. For a linear wave equation, this scheme has been shown to be stable for a CFL number less than 2.8 (Jameson, Schmidt, and Turkel, 1981) for a finite difference scheme, and is stable for our hybrid scheme with a CFL number less than or equal to 2. Following Jameson et al., a local time step that is restricted by the CFL number is used. Because of this, no physical interpretation should be given to the transient solutions.

### 2.3 Filtering

Filtering is required in suppressing the Gibbs error. A Schumann filter used by Gottlieb et al. (1982) and given by the following formula has been applied every 35 time steps at a CFL number of 3.5 (see Section 2.5, Convergence Acceleration).

$$q_K = 0.25(q_{K+1} + 2q_K + q_{K-1}); K = i, j \quad (3)$$

where  $i$  and  $j$  denote indices of the discrete points in the X and Y directions, respectively. At the shock wave, one-sided filtering in the X direction is applied to preserve the sharpness of the shock wave. The Schumann filter is equivalent to a first-order artificial viscosity. However, the filter is applied only every 35 time steps. The order of the error is higher than first order. No high-mode smoothing (Gottlieb et al., 1982) has been applied.

We have experimented with other filtering methods, such as derivative smoothing and artificial viscosity. The former is a low-pass filter in the wave number space when evaluating derivatives spectrally. It is expected to yield a smoother residue and thus stabilize the calculations. Numerical experiments do not favor this approach, as the filter fails to stabilize the computations. As to the artificial viscosity, the shock wave is smeared in the computations, which defeats the nondissipative nature of the spectral scheme.

#### 2.4 Boundary Conditions

The numerical implementation of boundary conditions for a hyperbolic system of partial differential equations is an active research subject in itself. Essentially, on a boundary  $Y_0$ , there are four characteristics that correspond to the speeds  $q_n$ ,  $q_t$ ,  $q_n - c$  and  $q_n + c$ . The respective characteristic variables are  $p - c_o^2 \rho$ ,  $q_t$ ,  $p - \rho_o c_o q_n$ , and  $p + \rho_o c_o q_n$ , where the subscript o stands for the quantities at the previous time step. Only the characteristic variables carried on the outgoing characteristics from the interior of the fluid domain can be computed from the governing equations. The characteristic variables carried on the incoming characteristics must be replaced by the appropriate boundary conditions. The flow quantities can then be recovered from the combination of the boundary conditions and the outgoing characteristic variables.

On the solid surface  $Y = 0$ , there is only one incoming characteristic. Let  $(M, N)$  be the momentum along the surface and normal to the surface, respectively, and  $\Delta Q$  be the symbol for the temporal change of physical quantities  $Q$  as computed by the interior formula, with the subscript c denoting the quantities computed by the interior formula. The following formulae for the physical quantities at the boundary points can then be given.

$$\Delta P = \Delta E + \gamma(\gamma-1)M_\infty^2 \left( -\frac{M}{\rho} \Delta M + \frac{1}{2} \frac{M^2}{\rho^2} \Delta \rho \right) \quad (4)$$

$$P_c = P_o + \Delta P \quad (5)$$

$$\left( \frac{M}{\rho} \right)_c = M_o / \rho_o + (\Delta M - \Delta \rho \cdot M_o / \rho_o) / \rho_o \quad (6)$$

$$\rho_c = \rho_o + \Delta\rho \quad (7)$$

$$P^{(n)} = P_c - \gamma M_\infty^2 \left( \Delta N \cdot c_o \right) \quad (8)$$

$$\rho^{(n)} = \rho_c + \frac{1}{\gamma M_\infty^2} (P^{(n)} - P_c) / c_o^2 \quad (9)$$

$$M^{(n)} = \rho^{(n)} \cdot (M/\rho)_c \quad (10)$$

$$N^{(n)} = 0 \quad (11)$$

$$E^{(n)} = P^{(n)} + \frac{1}{2} \gamma(\gamma-1) M_\infty^2 \left[ M^{(n)} \right]^2 / \rho^{(n)} \quad (12)$$

where the superscript n stands for the newly advanced quantities, and all velocities are nondimensionalized by the free-stream velocity.

At the far field boundary, the treatment is essentially the same as that used by Jameson et al. (1981) except that the "extrapolated" quantities as defined in that paper are those computed by the interior computations.

## 2.5 Convergence Acceleration

To increase the stability of the time-stepping scheme, an additional "residue-smoothing" process (Jameson and Baker, 1983) has been implemented. After the residue R has been evaluated at every mesh point, the residues are smoothed by a linear transformation defined as follows:

$$\bar{R} = (1 - \epsilon \delta_X^2)^{-1} (1 - \epsilon \delta_Y^2)^{-1} R \quad (13)$$

where  $\delta_X$  and  $\delta_Y$  are conventional finite difference operators in X and Y, and  $\epsilon$  is the parameter for the residue-averaging process. The new modified residue field  $\bar{R}$  is used to advance the solution in time. This process alters the time-dependent solution without changing its steady state. To bring out the essentials of the residue-averaging process, a simple wave equation is considered:

$$\phi_t + c\phi_x = 0 \quad (14)$$

The residue-averaging process as described is equivalent, to the lowest order, to adding an additional term to the original simple wave equation and converting it to the following equation:

$$\phi_t + c\phi_x - \epsilon(\Delta x)^2 \phi_{txx} = 0 \quad (15)$$

The dispersion relation for this equation can be given as

$$\frac{\omega}{k} = \frac{c}{1 + \epsilon k^2 (\Delta x)^2} \quad (16)$$

where  $\omega$  is the frequency and  $k$  is the wave number. By increasing the parameter  $\epsilon$ , the wave speed for the high wave number component is substantially increased. This decrease in wave speed for the dangerous short waves contributes to the substantial increase in the time step. In fact, Equation (15) is the linearized form of a model equation for long dispersive waves discussed by Benjamin, Bona, and Mahony (1972), who pointed out the numerical advantage of this equation over the Korteweg-de-Vries equation. Other means of manipulating the dispersion relation to gain stability have been suggested (e.g., Gottlieb and Turkel, 1980). However, these methods do not recover the original equation in steady state, although the error is of higher order. The residue-averaging process substantially extends the stability boundary. A CFL number of 3.5 has been used without any difficulty.

### 3. Computed Results for Hybrid Scheme

The initial effort employed a hybrid spectral/finite difference discretization to gain some experience with the problem. In the circumferential direction, the variables are expanded in a Fourier series because of the periodic nature of the problem. In the radial direction, a central finite difference scheme is used. This hybrid scheme is designed to answer some questions in applying the pseudospectral method to transonic flows. The application of the pseudospectral method to a realistic airfoil shape can be demonstrated by this scheme. Since we expect that the shock wave will be normal to the airfoil surface, the discontinuity is mainly in the X direction. Adequate resolution of the shock wave can be achieved and the question of convergence of the spectral series can be answered using the hybrid scheme. Other properties, such as the time-stepping scheme, convergence acceleration, and the filtering technique, can also be studied with the hybrid scheme. We shall use a Karman-Trefftz airfoil for this work because of its simple analytical mapping from the physical plane to the interior of the circle. The method can easily be extended to an airfoil of arbitrary shape by using a truncated complex series to map the profile to a circle.

For testing the solution algorithm, flows around a circular cylinder are computed. The pressure distribution for a subcritical flow with  $M_\infty = 0.39$  is given in Figure 1. The computation is performed on a  $64 \times 24$  grid (64 points in the circumferential direction, 24 points radially). It has been computed without filtering. A supercritical case with  $M_\infty = 0.45$  is also computed, and the results are shown in Figure 2. Filtering is performed every 35 time steps with a CFL number of 3.5. The results agree with a finite volume calculation by Jameson et al. (1981). The shock wave has no internal structure and is sharply defined.

A Karman-Trefftz airfoil with the following transformation from the mapped plane  $\zeta$  to the physical plane  $z$  is chosen for calculations.

$$\frac{z}{\kappa L} = \frac{(1+L\zeta)^\kappa + (1-L\zeta)^\kappa}{(1+L\zeta)^\kappa - (1-L\zeta)^\kappa} ; \kappa = 1.9 \quad (17)$$

$$L = (1 - \eta_0^2)^{1/2} - \xi_0 ; \zeta_0 = (\xi_0, \eta_0) = (-0.1, 0) \quad (18)$$

Supercritical non-lifting flows with  $M_\infty = 0.75$  are computed on a  $64 \times 24$  grid. The results are shown in Figure 3, together with the results from a finite volume calculation. The hybrid calculation shows again a sharply defined shock wave. The agreement between the two calculations is very good. In particular, the positions of the shock as defined by the midpoint of the structure show close agreement. There are discrepancies immediately behind the shock wave, however, and the source of these discrepancies is not clear. The pressure ratio across the shock wave using the pseudospectral calculation has been checked against that using the Rankine-Hugoniot relation based on the upstream Mach number. The error is less than 4 percent.

To demonstrate the convergence of the Fourier series, the same case is computed on a  $32 \times 24$  grid. The results are shown in Figure 4, together with the results of calculations on a denser mesh using a finite volume calculation. The accuracy of the  $32 \times 24$  calculation is quite good. The shock resolution of the sparse mesh calculation is comparable to that of the  $64 \times 24$  finite volume calculation. As expected, the finite volume calculation on the sparse grid does not produce acceptable results.



#### 4. Full Spectral Scheme

To carry the work further, we have attempted to construct a full spectral method. Instead of using a finite difference method for the radial direction in the transformed circular plane, we have used a Chebyshev polynomial expansion for that direction.

We immediately encountered difficulties, however, in using the Chebyshev spectral method. The first difficulty is the stability problem. Chebyshev collocation points are defined as

$$y = \frac{1}{2} \left[ 1 - \cos \pi \frac{(J-1)}{N} \right] \quad (19)$$

where  $N+1 \geq J \geq 1$  is the computational coordinate and  $1 \geq y \geq 0$  is the physical space. It is easy to verify that the spacing of the grid points at the end points is asymptotically

$$\Delta y \sim 0 \left( \frac{1}{N^2} \right) \quad (20)$$

For viscous problems, the end points are usually on the solid surface, where the flow velocity vanishes. The time steps can maintain a reasonable size even though the grid spacing is small, since

$$\Delta t \sim \text{CFL} \left( \frac{\Delta y}{u} \right) \quad (21)$$

In the present case,

$$\Delta t \sim \text{CFL} \left( \frac{\Delta y}{|u|+c} \right) \quad (22)$$

where  $c$  is the speed of sound. The small grid size near the end points forces

$$\Delta t \sim \frac{1}{N^2} \quad (23)$$

The solution will take an excessively large number of time steps to develop. Also, because of large variations in the grid spacing, the local time step approach used successfully in the hybrid method does not seem to apply.

An attempt to stretch the Chebyshev grid to achieve a more uniform grid spacing also failed. The accuracy near the end points deteriorates, which affects the accurate application of boundary conditions. This deterioration of accuracy in a stretched grid can be understood by taking the extreme example of restoration to a uniform grid. Let

$$\eta = \frac{1}{2} (1 - \cos \pi y) \quad (24)$$

where the computational space  $\eta$  is divided into Chebyshev collocation points and the corresponding  $y$  coordinate is uniform. By the chain rule, we have

$$\frac{\partial}{\partial y} = \frac{d\eta}{dy} \frac{\partial}{\partial \eta} \quad (25)$$

$$\frac{d\eta}{dy} = \frac{\pi}{2} \sin \pi y \quad (26)$$

Since  $d\eta/dy$  approaches zero at the end points, accurate evaluation of the derivative at the end points is not possible.

We currently plan to investigate two other methods. The first is to discard the Chebyshev method and attempt the Fourier polynomial subtraction method (Gottlieb and Orszag, 1977). The second is to develop an implicit method to circumvent the stability problem.

## 5. Conclusions

The hybrid method shows promise for the use of spectral methods to accurately resolve the shock wave in a realistic problem. However, the filtering of the solution certainly deteriorates the accuracy. Furthermore, for complex three-dimensional problems, it is difficult to identify a supersonic-supersonic shock. Present means of identifying shock waves by the sonic condition do not apply there. Unlike the finite difference method, the residue of a spectral method does not decrease with the number of time steps. At present, the number of supersonic points is used as the indicator of convergence.

The full spectral method using a Chebyshev expansion also presents difficulties. Further investigations of alternative methods are required to assess the merit of a full spectral scheme.

References

- Benjamin, T. B., Bona, J. L., and Mahony, J. J. (1972) "Model Equations for Long Waves in Non-Linear Dispersive Systems," Phil. Trans. Roy. Soc. London (Ser. A.), 272, pp. 47-78.
- Gottlieb, D., Lustman, L., and Streett, C. L. (1982) "Spectral Methods for Two-Dimensional Shocks," ICASE rep. 82-38.
- Gottlieb, D., Lustman, L., and Orszag, S. A. (1981) "Spectral Calculations of One-Dimensional Inviscid Compressible Flows," SIAM J. Sci. Stat. Comput., 2, 3, pp. 296-310.
- Gottlieb, D., and Turkel, E. (1980) "On Time Discretization for Spectral Methods," Stud. Appl. Math., 63, pp. 67-86.
- Gottlieb, D., and Orszag, S. (1977) "Numerical Analysis of Spectral Methods: Theory and Applications," NSF-CBMS Monograph No. 26, Society of Industrial and Applied Mathematics.
- Jameson, A., and Baker, T. (1983) "Solution of the Euler Equations for Complex Configurations," AIAA paper 83-1929.
- Jameson, A., Schmidt, W., and Turkel, E. (1981) "Numerical Solutions of the Euler Equations by Finite Volume Methods Using Runge-Kutta Time-Stepping Schemes," AIAA paper 81-1259.
- Jou, W. H., Jameson, A., and Metcalfe, R. W. (1983) "Pseudospectral Calculations of Two-Dimensional Transonic Flow," Proceedings of Fifth GAMM Conference on Numerical Methods in Fluid Mechanics, Rome, Italy, October 5-7.
- Voight, R. G., Gottlieb, D., and Hussaini, M. Y. (1984) Spectral Methods for Partial Differential Equations, Society for Industrial and Applied Mathematics, Philadelphia, 267 pp.

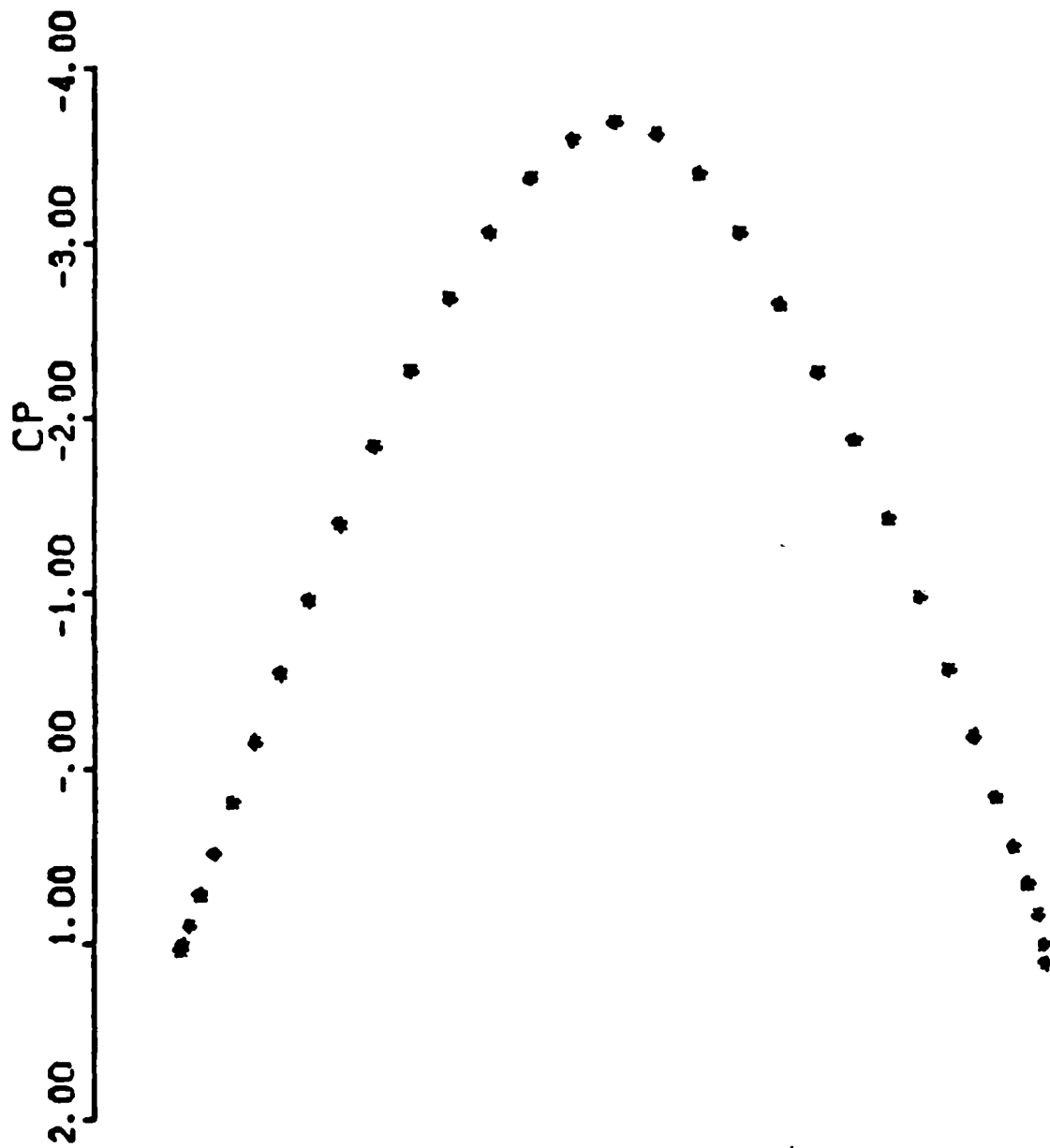


Figure 1. Pressure Distribution for a Subcritical Flow Over a Cylinder at Mach 0.39

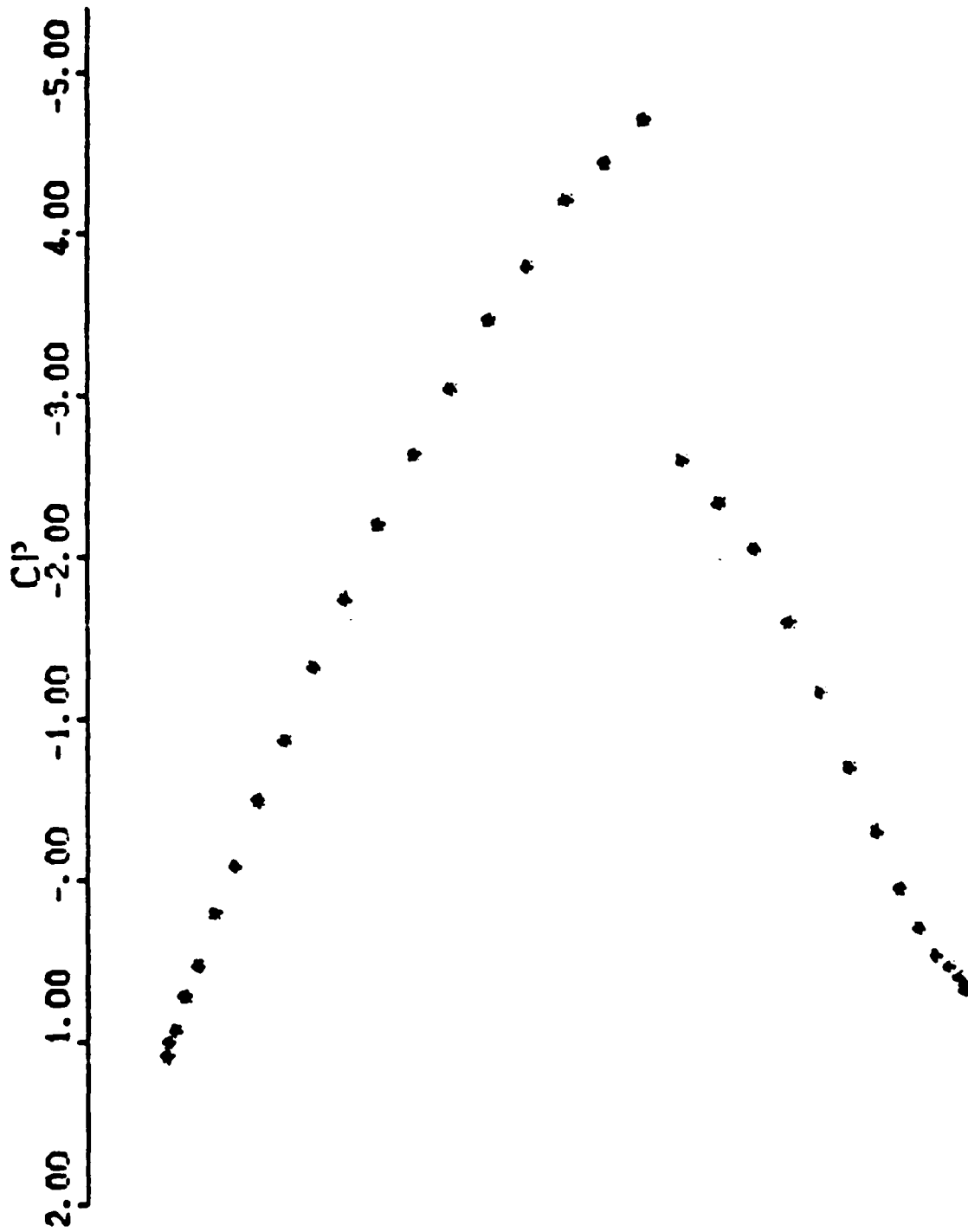
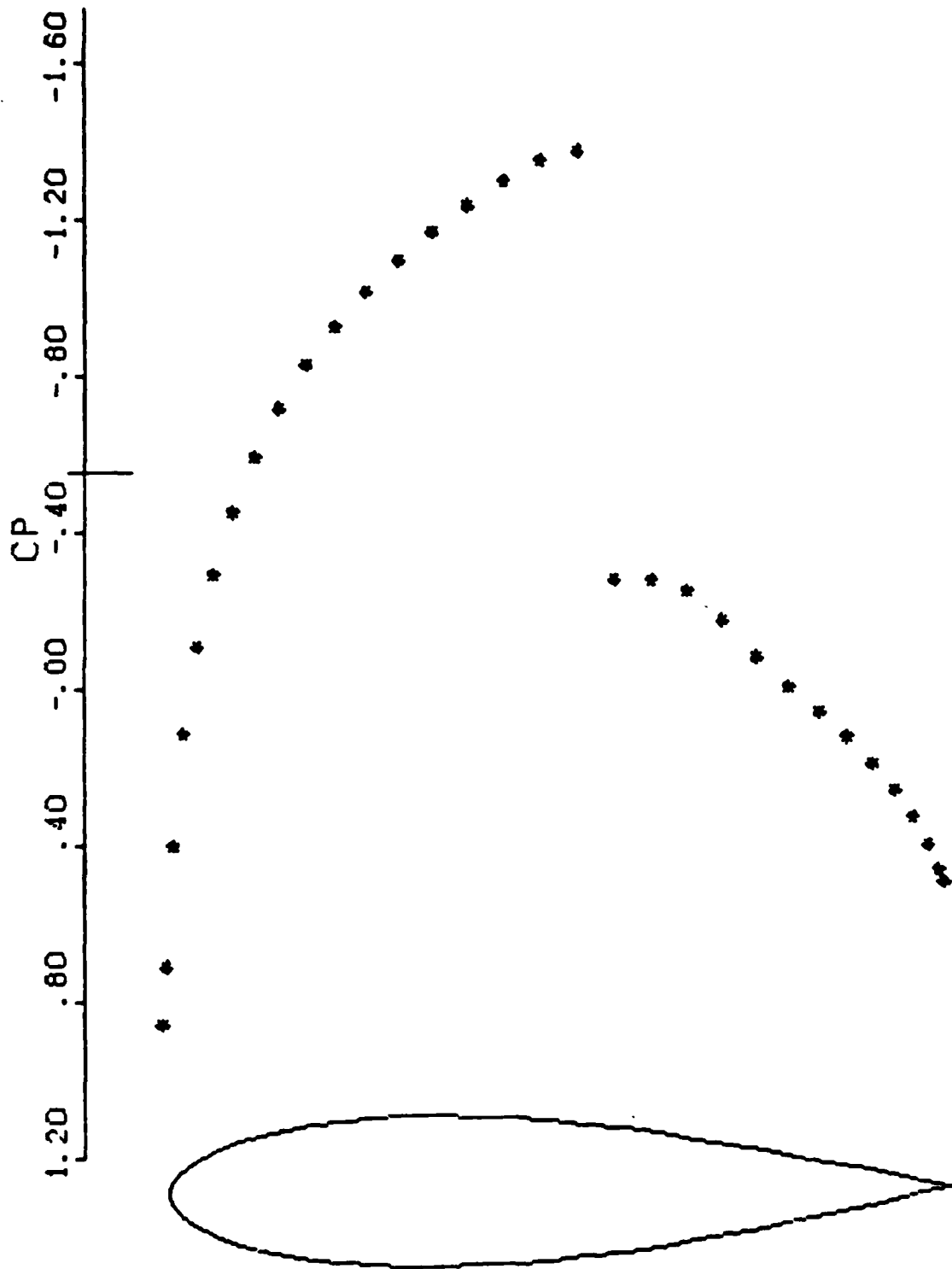


Figure 2. Pressure Distribution for a Supercritical Flow Over a Cylinder at Mach 0.45



**Figure 3. Pressure Distribution on a Karman-Trefftz Airfoil at Mach 0.75 Using a  $64 \times 24$  Grid (350 Steps)**

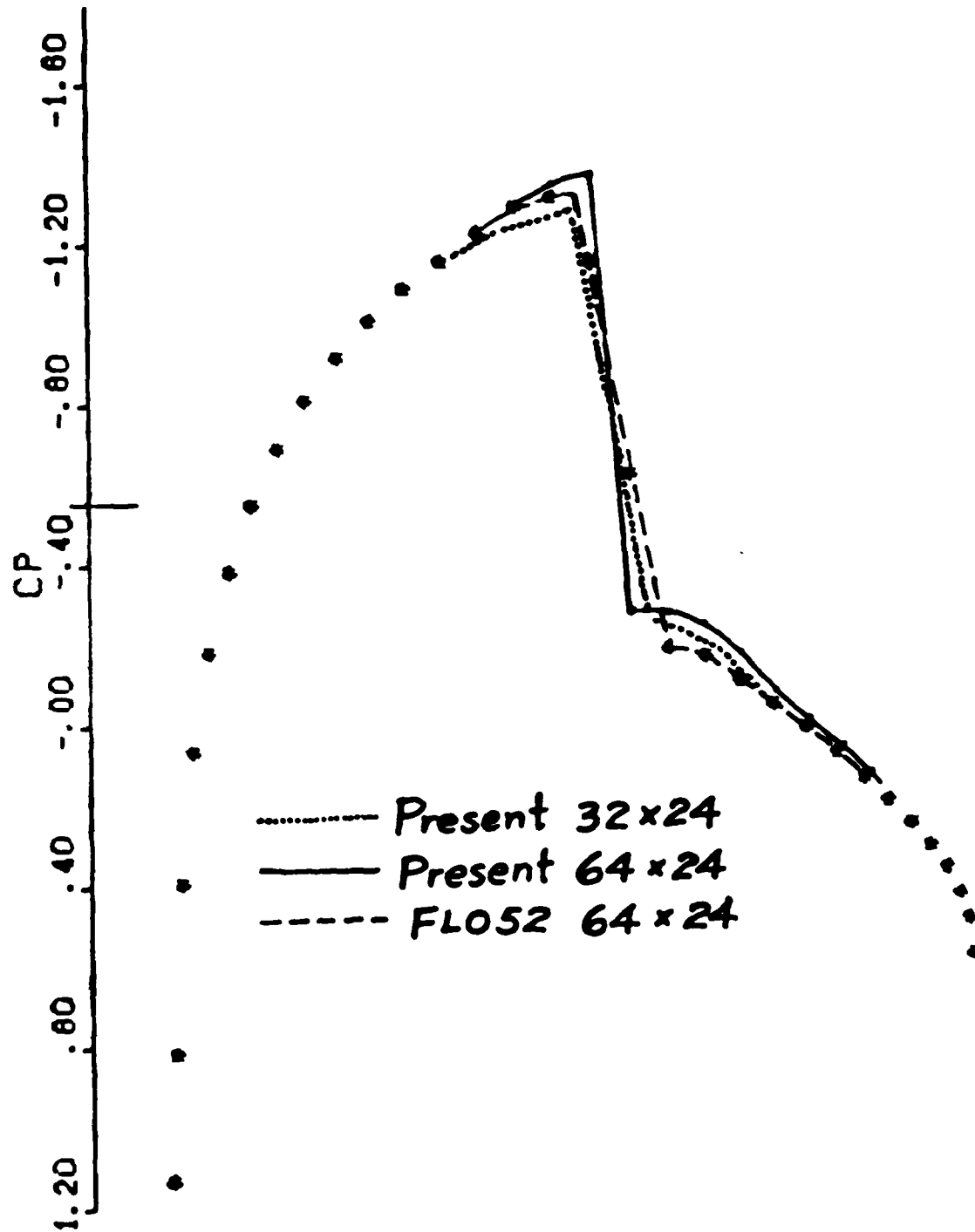


Figure 4. Comparison of Results with a Finite Volume Scheme for a Karman-Trefftz Airfoil at Mach 0.75



Appendix  
"Pseudospectral Calculations of  
Two-Dimensional Transonic Flow"

(Presented at Fifth  
GAMM Conference on Numerical Methods  
in Fluid Mechanics, Rome, Italy,  
October 5-7, 1983.)

# PSEUDOSPECTRAL CALCULATIONS OF TWO-DIMENSIONAL TRANSONIC FLOW

Wen-Huei Jou

Flow Research Company, Kent, Washington, U.S.A.

Antony Jameson

Princeton University, Princeton, New Jersey, U.S.A.

Ralph Metcalfe

Flow Research Company, Kent, Washington, U.S.A.

## SUMMARY

A hybrid pseudospectral-finite difference scheme is used to calculate transonic flow over a two-dimensional object using the Euler equations. The exterior of the object is mapped to the interior of a circle. The flow field variables are discretized using a Fourier series in the circumferential direction, while a central finite difference scheme is used in the radial direction. We used a four-stage Runge-Kutta scheme including a filter and a residue-smoothing process. Transonic flows over a circular cylinder as well as a Karman-Trefftz airfoil were computed. The results are compared to those from finite volume calculations. It is found that the pseudospectral calculations are able to produce shocks with no internal structure, and fewer grid points are needed to obtain the required accuracy.

## INTRODUCTION

In recent years, there has been strong interest in computations of transonic flows using the time-dependent Euler equations. This interest stems in part from the possibility of shock-generated vorticity in the flow field and in part from the interest in numerical methods for a nonlinear hyperbolic system. Most of the numerical methods are finite difference in nature and are second order in accuracy. To stabilize the computation and to smooth the dispersive error for unsteady computations, either artificial dissipative terms are added to the equations or a built-in dissipative mechanism is included in the numerical scheme. These dissipative terms usually cause the shock wave to span across three to four grid points. To capture a shock with reasonable accuracy, one is forced to use fairly dense grid distributions over the region where the shock wave is expected to be.

The pseudospectral method is an alternative to the finite difference method. It has been applied successfully to many smoothly varying flows. The numerical analysis of the method has been given in detail by Gottlieb and Orszag in a monograph [1]. Because of its high rate of convergence, the method usually requires relatively few terms of the basis functions for accurate computations. In addition to the spatial accuracy, the dispersive error for unsteady computations is also minimized.

Recently, efforts have been made to apply the pseudospectral method to flows with shock waves. Gottlieb, Lustman, and Orszag [2] have demonstrated the feasibility of the pseudospectral method through the solution of a one-dimensional shock

tube problem. By using the shock-capturing technique, they showed that the shock wave can be resolved within one grid point. The Gibbs phenomenon error due to the discontinuity can be filtered to improve the accuracy. Gottlieb, Lustman, and Streett [3] have attempted the two-dimensional problem of the reflection of an oblique shock from a wall. The results from this investigation are encouraging. Using a fairly sparse grid, they showed that the shock wave can be resolved within one grid point. The accuracy of the solution as compared to the exact solution is reasonable considering the sparseness of the grid points.

In the present work, we shall consider steady transonic flows around an airfoil by solving the Euler equations. We shall address problems of applying the pseudospectral method to flows around a complex geometry, including the development of a time-stepping scheme, and enhancement of the stability by residue averaging. Numerical experimentation has been used to confirm convergence with a small number of basis functions, and also the capability to treat shock waves with the aid of filtering.

#### GOVERNING EQUATIONS AND BASIC APPROACH

The basic approach is to map the exterior of an airfoil to the interior of a circle. Polar coordinates in the mapped plane will be used. Spectral decomposition of the solution can be used in the mapped plane. To serve this purpose, the Euler equations in the mapped plane are written in fully conservative form by using both physical and contravariant velocities. These equations are

$$\frac{\partial}{\partial t} (\vec{Q}) + \frac{\partial}{\partial X} (\vec{F}) + \frac{\partial}{\partial Y} (\vec{G}) = 0 \quad (1)$$

where

$$\vec{Q} = J \begin{bmatrix} \rho \\ \rho u \\ \rho v \\ E \end{bmatrix} ; \quad \vec{F} = \begin{bmatrix} \rho U \\ \rho u U + y_Y P / \gamma M_\infty^2 \\ \rho v U - x_Y P / \gamma M_\infty^2 \\ \rho H U \end{bmatrix} ; \quad \vec{G} = \begin{bmatrix} \rho V \\ \rho u V - y_X P / \gamma M_\infty^2 \\ \rho v V + x_X P / \gamma M_\infty^2 \\ \rho H V \end{bmatrix} ;$$

$$\begin{bmatrix} U \\ V \end{bmatrix} = \begin{bmatrix} y_Y & -x_Y \\ -y_X & x_X \end{bmatrix} \begin{bmatrix} u \\ v \end{bmatrix} ; \quad H = [(\gamma - 1)P + E] / \rho ;$$

(x,y) are Cartesian coordinates in the physical plane, (X,Y) are polar coordinates in the mapped plane,  $\rho$  is the density, (u,v) are velocity components, (U,V) are unscaled contravariant velocity components, E is the energy, H is the specific enthalpy, P is the pressure, J is the Jacobian of the transformation,  $M_\infty$  is the free-stream Mach number, and  $\gamma$  is the specific heat ratio. P,  $\rho$  and the velocity vector (u,v) are nondimensionalized by their values at the free-stream condition, E and H are nondimensionalized by the free-stream internal energy  $\rho_\infty C_v T_\infty$ , and other variables at the free-stream condition are computed from these variables.

The physical boundary conditions are defined by the solid-wall condition on the airfoil surface and the fact that the

disturbances generated by the airfoil propagate outward to infinity. The numerical implementation of these physical boundary conditions will be discussed later.

This initial effort employed a hybrid spectral-finite difference discretization to gain some experience with the problem. In the circumferential direction, the variables are expanded in a Fourier series because of the periodic nature of the problem. In the radial direction, a central finite difference scheme is used. This hybrid scheme is designed to answer some questions in applying the pseudospectral method to transonic flows. The application of the pseudospectral method to a realistic airfoil shape can be demonstrated by this scheme. Since we expect that the shock wave will be normal to the airfoil surface, the discontinuity is mainly in the X direction. Adequate resolution of the shock wave can be achieved and the question of convergence of the spectral series can be answered using the hybrid scheme. Other properties, such as the time-stepping scheme, convergence acceleration, and the filtering technique can also be studied with the hybrid scheme. We shall use a Karman-Trefftz airfoil for this work because of its simple analytical mapping from the physical plane to the interior of the circle. The method can easily be extended to an airfoil of arbitrary shape by using a truncated complex series to map the profile to a circle.

#### NUMERICAL SCHEME

A computational mesh is created by equally dividing the (X,Y) coordinates in the mapped plane. In the mapped plane, the spatial derivatives in X at each mesh point are evaluated by application of a fast Fourier transform. The derivatives in Y are evaluated by second-order central finite differences. Evaluation of the elements in the transformation matrices ( $x_x, x_y, y_x, y_y$ ) is performed in the same manner. The singularity of the transformation at the trailing edge is avoided by placing it between two mesh points.

By using this method of evaluating spatial derivatives, the governing equations are converted to a system of ordinary differential equations in time. These equations can be solved numerically by using any of a variety of well-developed techniques for the solution of ordinary differential equations. An approximate fourth-order Runge-Kutta scheme is used in this work. The algorithm is given by the following equations:

$$\vec{q}^{(n)} = \vec{q}^0 + \frac{1}{(5-n)} \vec{R}^{(n-1)} ; n = 1, \dots, 4 \quad (2)$$

where  $\vec{q}$  represents the flow variables at the mesh points,  $\vec{R}$  represents the terms with spatial derivatives in the equations, and  $n$  denotes the Runge-Kutta step. This scheme has been shown to be stable for a CFL number less than 2.8 [4] for a finite difference scheme, and is stable for our hybrid scheme with a CFL number less than or equal to 2. Following Jameson, Schmidt, and Turkel [4], a local time step that is restricted by the CFL number is used. Because of this, no physical interpretation should be given to the transient solutions.

## FILTERING

Filtering is required in suppressing the Gibbs error. A Schumann filter used by Gottlieb, Lustman, and Streett [3] and given by the following formula has been applied every 35 time steps at a CFL number of 3.5 (see later section on convergence acceleration).

$$q_K = 0.25(q_{K+1} + 2q_K + q_{K-1}); K = i, j \quad (3)$$

where  $i$  and  $j$  denote indices of the discrete points in the  $X$  and  $Y$  directions, respectively. At the shock wave, one-sided filtering in the  $X$  direction is applied to preserve the sharpness of the shock wave. The Schumann filter is equivalent to a first-order artificial viscosity. However, the filter is applied only every 35 time steps. The order of the error is higher than first order. No high-mode smoothing [3] has been applied.

## BOUNDARY CONDITIONS

The numerical implementation of boundary conditions for a hyperbolic system of partial differential equations is an active research subject in itself. Essentially, on a boundary  $Y_0$ , there are four characteristics that correspond to the speeds  $q_n$ ,  $q_t$ ,  $q_n - c$  and  $q_n + c$ . The respective characteristic variables are  $p - c_0^2 \rho$ ,  $q_t$ ,  $p - \rho_0 c_0 q_n$ , and  $p + \rho_0 c_0 q_n$ , where the subscript  $0$  stands for the quantities at the previous time step. Only the characteristic variables carried on the outgoing characteristics from the interior of the fluid domain can be computed from the governing equations. The characteristic variables carried on the incoming characteristics must be replaced by the appropriate boundary conditions. The flow quantities can then be recovered from the combination of the boundary conditions and the outgoing characteristic variables.

On the solid surface  $Y = 0$ , there is only one incoming characteristic. Let  $(M, N)$  be the momentum along the surface and normal to the surface, respectively, and  $\Delta Q$  be the symbol for the temporal change of physical quantities  $Q$  as computed by the interior formula, with the subscript  $c$  denoting the quantities computed by the interior formula. The following formulae for the physical quantities at the boundary points can then be given.

$$\Delta P = \Delta E + \gamma(\gamma-1)M_\infty^2 \left( -\frac{M}{\rho} \Delta M + \frac{1}{2} \frac{M^2}{\rho^2} \Delta \rho \right) \quad (4)$$

$$P_c = P_0 + \Delta P \quad (5)$$

$$\left( \frac{M}{\rho} \right)_c = M_0/\rho_0 + (\Delta M - \Delta \rho \cdot M_0/\rho_0)/\rho_0 \quad (6)$$

$$\rho_c = \rho_0 + \Delta \rho \quad (7)$$

$$P^{(n)} = P_c - \gamma M_\infty^2 \left( \Delta N \cdot c_0 \right) \quad (8)$$

$$\rho^{(n)} = \rho_c + \frac{1}{\gamma M_\infty^2} (P^{(n)} - P_c)/c_0^2 \quad (9)$$

$$M^{(n)} = \rho^{(n)} \cdot (M/\rho)_c \quad (10)$$

$$N^{(n)} = 0 \quad (11)$$

$$E^{(n)} = P^{(n)} + \frac{1}{2} \gamma(\gamma-1) M_\infty^2 \left[ M^{(n)} \right]^2 / \rho^{(n)} \quad (12)$$

where the superscript  $n$  stands for the newly advanced quantities, and all velocities are nondimensionalized by the free-stream velocity.

At the far field boundary, the treatment is essentially the same as that used by Jameson, Schmidt, and Turkel [4] except that the "extrapolated" quantities as defined in that paper are those computed by the interior computations.

#### CONVERGENCE ACCELERATION

To increase the stability of the time-stepping scheme, an additional "residue-smoothing" process [5] has been implemented. After the residue  $R$  has been evaluated at every mesh point, the residues are smoothed by a linear transformation defined as follows:

$$\bar{R} = (1 - \epsilon \delta_X^2)^{-1} (1 - \epsilon \delta_Y^2)^{-1} R \quad (13)$$

where  $\delta_X$  and  $\delta_Y$  are conventional finite difference operators in  $X$  and  $Y$ , and  $\epsilon$  is the parameter for the residue-averaging process. The new modified residue field  $\bar{R}$  is used to advance the solution in time. This process alters the time-dependent solution without changing its steady state. To bring out the essentials of the residue-averaging process, a simple wave equation is considered:

$$\phi_t + c\phi_x = 0 \quad (14)$$

The residue-averaging process as described is equivalent, to the lowest order, to adding an additional term to the original simple wave equation and converting it to the following equation:

$$\phi_t + c\phi_x - \epsilon(\Delta x)^2 \phi_{txx} = 0 \quad (15)$$

The dispersion relation for this equation can be given as

$$\frac{\omega}{k} = \frac{c}{1 + \epsilon k^2 (\Delta x)^2} \quad (16)$$

where  $\omega$  is the frequency and  $k$  is the wave number. By increasing the parameter  $\epsilon$ , the wave speed for the high wave number component is substantially increased. This decrease in wave speed for the dangerous short waves contributes to the substantial increase in the time step. In fact, Equation (15) is the linearized form of a model equation for long dispersive waves

discussed by Benjamin, Bona, and Mahony [6], who pointed out the numerical advantage of this equation over the Korteweg-de-Vries equation. Other means of manipulating the dispersion relation to gain stability have been suggested (e.g., [7]). However, these methods do not recover the original equation in steady state, although the error is of higher order. The residue-averaging process substantially extends the stability boundary. A CFL number of 3.5 has been used without any difficulty.

### COMPUTED RESULTS

For testing the solution algorithm, flows around a circular cylinder are computed. The pressure distribution for a subcritical flow with  $M_\infty = 0.39$  is given in Figure 1. The computation is performed on a 64x24 grid (64 points in the circumferential direction, 24 points radially). It has been computed without filtering. A supercritical case with  $M_\infty = 0.45$  is also computed, and the results are shown in Figure 2. Filtering is performed every 35 time steps with a CFL number of 3.5. The results agree with a finite volume calculation by Jameson, Schmidt, and Turkel, [4]. The shock wave has no internal structure and is sharply defined.

A Karman-Trefftz airfoil with the following transformation from the mapped plane  $\zeta$  to the physical plane  $z$  is chosen for calculations.

$$\frac{z}{\kappa L} = \frac{(1+L\zeta)^\kappa + (1-L\zeta)^\kappa}{(1+L\zeta)^\kappa + (1-L\zeta)^\kappa} ; \kappa = 1.9 \quad (17)$$

$$L = (1 - \eta_0^2)^{1/2} - \xi_0 ; \zeta_0 = (\xi_0, \eta_0) = (-0.1, 0) \quad (18)$$

Supercritical non-lifting flows with  $M_\infty = 0.75$  are computed on a 64x24 grid. The results are shown in Figure 3, together with the results from a finite volume calculation. The hybrid calculation shows again a sharply defined shock wave. The agreement between the two calculations is very good. In particular, the positions of the shock as defined by the midpoint of the structure show close agreement. There are discrepancies immediately behind the shock wave, however. The source of these discrepancies is not clear. The pressure ratio across the shock wave using the pseudospectral calculation has been checked against that using the Rankine-Hugoniot relation based on the upstream Mach number. The error is less than 4 percent.

To demonstrate the convergence of the Fourier series, the same case is computed on a 32x24 grid. The results are shown in Figure 4, together with the results of calculations on a denser mesh using a finite volume calculation. The accuracy of the 32x24 calculation is quite good. The shock resolution of the sparse mesh calculation is comparable to that of the 64x24 finite volume calculation. As expected, the finite volume calculation on the sparse grid does not produce acceptable results.

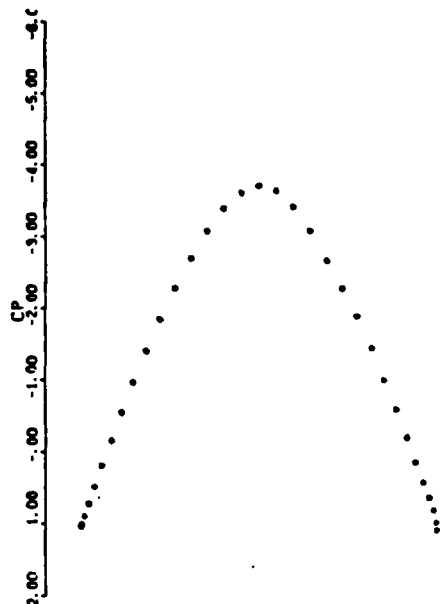


Figure 1. Pressure distribution for a subcritical flow over a cylinder at Mach 0.39

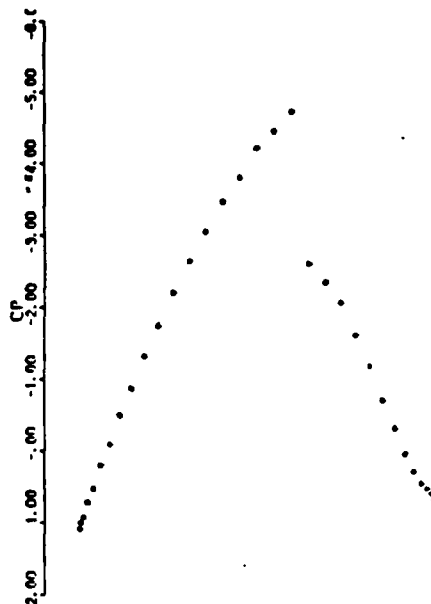


Figure 2. Pressure distribution for a supercritical flow over a cylinder at Mach 0.45

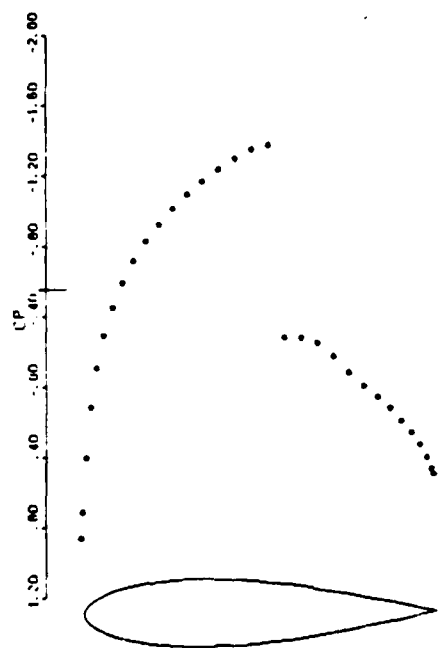


Figure 3. Pressure distribution on a Karman-Trefftz airfoil at Mach 0.75 using a 64x24 grid (350 steps)

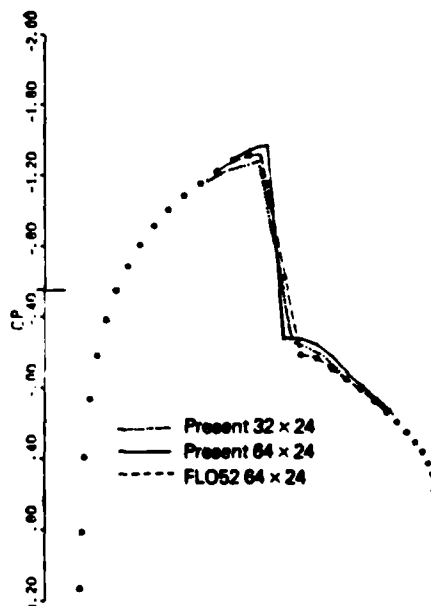


Figure 4. Comparison of results with a finite volume scheme for a Karman-Trefftz airfoil at Mach 0.75



## CONCLUSIONS AND ACKNOWLEDGEMENTS

Several conclusions can be drawn from the present investigation.

- (1) In computing flows with shock waves, the Gibbs error can be filtered to produce accurate results. Because of the rapid convergence of the Fourier series, fewer grid points are required than with the lower order difference-type scheme.
- (2) A shock wave without internal structure can be produced. This capability also contributes to the accuracy of the method in that fewer grid points are required to resolve the shock wave.
- (3) Application of the pseudospectral method to flows around a realistic geometry is possible using a mapping technique.

The authors are indebted to Mr. Morton Cooper of Flow Research Company for suggesting the problem. Discussions with Professor Steven Orszag have also been very helpful. This work was supported by the Air Force Office of Scientific Research and the Office of Naval Research under Contract No. F49620-82-C-0022.

## REFERENCES

- [1] Gottlieb, D., and Orszag, S., Numerical Analysis of Spectral Methods: Theory and Applications, NSF-CBMS Monograph No. 26, Society of Industrial and Applied Mathematics (1977).
- [2] Gottlieb, D., Lustman, L., and Orszag, S. A., "Spectral calculations of one-dimensional inviscid compressible flows," SIAM J. Sci. Stat. Comput., 2, 3 (1981) pp. 296-310.
- [3] Gottlieb, D., Lustman, L., and Streett, C. L., "Spectral methods for two-dimensional shocks," ICASE rep. 82-38 (1982).
- [4] Jameson, A., Schmidt, W., and Turkel, E., "Numerical solutions of the Euler equations by finite volume methods using Runge-Kutta time-stepping schemes," AIAA paper 81-1259 (1981).
- [5] Jameson, A., and Baker, T., "Solution of the Euler equations for complex configurations," AIAA paper 83-1929 (1983).
- [6] Benjamin, T. B., Bona, J. L., and Mahony, J. J., "Model equations for long waves in non-linear dispersive systems," Phil. Trans. Roy. Soc. London Ser. A., 272 (1972) pp. 47-78.
- [7] Gottlieb, D., and Turkel, E., "On time discretization for spectral methods," Stud. Appl. Math., 63 (1980) pp. 67-86.

NUMERICAL INVESTIGATION OF  
VTOL AERODYNAMICS\*

by  
M. H. Rizk

September 1984

Flow Industries, Inc.  
Research and Technology  
Kent, Washington 98032

\*This work is supported by the Air Force Office of Scientific Research under  
Contract No. F49620-82-C-0022.

Table of Contents

	Page
List of Figures	ii
1. Introduction	1
2. Governing Equations	3
3. Method of Solution	5
4. Numerical Examples	6
Figures	9

# List of Figures

	Page
Figure 1. Model Problem for a Hovering VTOL Aircraft	9
Figure 2. Schematic of Flow Field about a Hovering VTOL Aircraft	10
Figure 3. Example 1: Velocity Vectors in the Plane $x = x_j$	11
Figure 4. Example 1: Velocity Vectors in the Plane $x = x_f$	11
Figure 5. Example 1: Velocity Vectors in the Plane $y = y_j$	12
Figure 6. Example 1: Velocity Vectors in the Plane $y = y_d$	13
Figure 7. Example 1: Pressure Contours in the Plane $x = x_j$	14
Figure 8. Example 1: Pressure Contours in the Plane $y = y_j$	15
Figure 9. Example 1: Pressure Contours in the Plane $z = z_g$	16
Figure 10. Example 1: Pressure Contours in the Plane $z = z_a$	16
Figure 11. Example 1: x-Vorticity Component in the Plane $x = x_j$	17
Figure 12. Example 1: y-Vorticity Component in the Plane $y = y_j$	18
Figure 13. Example 2: Velocity Vectors in the Plane $x = x_j$	19
Figure 14. Example 2: Velocity Vectors in the Plane $x = x_f$	19
Figure 15. Example 2: Velocity Vectors in the Plane $y = y_j$	20
Figure 16. Example 2: Velocity Vectors in the Plane $y = y_d$	21
Figure 17. Example 2: Pressure Contours in the Plane $x = x_j$	22
Figure 18. Example 2: Pressure Contours in the Plane $y = y_j$	23
Figure 19. Example 2: Pressure Contours in the Plane $z = z_g$	24
Figure 20. Example 2: Pressure Contours in the Plane $z = z_a$	24
Figure 21. Example 2: x-Vorticity Component in the Plane $x = x_j$	25
Figure 22. Example 2: y-Vorticity Component in the Plane $y = y_j$	26
Figure 23. Example 3: Velocity Vectors in the Plane $x = x_j$	27
Figure 24. Example 3: Velocity Vectors in the Plane $x = x_f$	27
Figure 25. Example 3: Velocity Vectors in the Plane $y = y_j$	28
Figure 26. Example 3: Velocity Vectors in the Plane $y = y_d$	29
Figure 27. Example 3: Pressure Contours in the Plane $x = x_j$	30
Figure 28. Example 3: Pressure Contours in the Plane $y = y_j$	31
Figure 29. Example 3: Pressure Contours in the Plane $z = z_g$	32
Figure 30. Example 3: Pressure Contours in the Plane $z = z_a$	32
Figure 31. Example 3: x-Vorticity Component in the Plane $x = x_j$	33
Figure 32. Example 3: y-Vorticity Component in the Plane $y = y_j$	34

List of Figures

	Page
Figure 33. Example 4: Velocity Vectors in the Plane $x = x_j$	35
Figure 34. Example 4: Velocity Vectors in the Plane $x = x_f$	35
Figure 35. Example 4: Velocity Vectors in the Plane $y = y_j$	36
Figure 36. Example 4: Velocity Vectors in the Plane $y = y_d$	37
Figure 37. Example 4: Pressure Contours in the Plane $x = x_j$	38
Figure 38. Example 4: Pressure Contours in the Plane $y = y_j$	39
Figure 39. Example 4: Pressure Contours in the Plane $z = z_g$	40
Figure 40. Example 4: Pressure Contours in the Plane $z = z_a$	40
Figure 41. Example 4: x-Vorticity Component in the Plane $x = x_j$	41
Figure 42. Example 4: y-Vorticity Component in the Plane $y = y_j$	42
Figure 43. Example 5: Velocity Vectors in the Plane $x = x_j$	43
Figure 44. Example 5: Velocity Vectors in the Plane $x = x_f$	43
Figure 45. Example 5: Velocity Vectors in the Plane $y = y_j$	44
Figure 46. Example 5: Velocity Vectors in the Plane $y = y_d$	45
Figure 47. Example 5: Pressure Contours in the Plane $x = x_j$	46
Figure 48. Example 5: Pressure Contours in the Plane $y = y_j$	47
Figure 49. Example 5: Pressure Contours in the Plane $z = z_g$	48
Figure 50. Example 5: Pressure Contours in the Plane $z = z_a$	49
Figure 51. Example 5: x-Vorticity Component in the Plane $x = x_j$	50
Figure 52. Example 5: y-Vorticity Component in the Plane $y = y_j$	51
Figure 53. Initial Vortex Propagation in Example 5	52
Figure 54. Initial Vortex Propagation in Example 1	53

## 1. Introduction

Work is in progress at Flow Industries on the direct numerical simulation of complex VTOL flows using the full three-dimensional, time-dependent Navier-Stokes equations. The objective of this numerical simulation is to compute accurately the details of the flow field and to achieve a better understanding of the physics of the flow, including the role of initial turbulence in the jet, the influence of forward motion on hover aerodynamics, the collision zone and fountain characteristics, and the jet structure and entrainment process in the transitional flight regime. The results of this work can be used to evaluate the merit of various models suggested in the past or can be used to construct a new model. This work will also allow the assessment of wing-jet-ground interference effects and the accurate prediction of their associated forces and moments, which is required for the design and optimization of VTOL aircraft. This note describes the work completed at Flow in the second year of a program in which VTOL aerodynamics are being investigated numerically.

The problem under investigation is that of an infinite row of jets impinging on the ground (see Figure 1). This problem, which contains the essential features of twin jets impinging on the ground (see Figure 2), simulates the hovering configuration. The choice of a row of jets provides the periodic property of the flow field, which allows approximation of the flow properties in the periodic direction by a truncated Fourier series. The spectral method may therefore be used in the periodic direction, while finite difference approximations are used in the vertical  $z$  direction and the  $y$  direction normal to the row of jets. The jets may be inclined in the  $y$  direction, which leads to a configuration associated with an aircraft in pitch while hovering. By imposing a cross flow in the  $y$  direction, it is possible to study the effects of the aircraft's forward motion during takeoff and transition.

A computer code that solves the time-dependent Navier-Stokes equations has been developed with the purpose of numerically simulating the problem of an infinite row of jets impinging on the ground. The code presently uses finite difference approximations in all three spatial directions, and it uses a first-order time-differencing scheme. Modifications are in progress that will allow the use of the spectral method in the periodic direction and the use of

a second-order time-differencing scheme. Subgrid-scale modeling, which allows the solution of problems at high Reynolds numbers, will also be introduced into the code. Although the code is not in its final form, it has been used to obtain solutions that indicate the main features of VTOL aerodynamics.

In this note, the governing equations and the boundary conditions used in the code are summarized in Section 2. The method of solution is discussed in Section 3, and preliminary examples of solutions using the code are presented in Section 4.

## 2. Governing Equations

The governing equations are the Navier-Stokes equation

$$\underline{q}_t + (\underline{q} \cdot \nabla) \underline{q} = -\nabla p + \frac{1}{Re} \nabla^2 \underline{q} \quad (1)$$

and the continuity equation

$$\nabla \cdot \underline{q} = 0 \quad (2)$$

where  $\underline{q}$  is the velocity vector and  $p$  is the pressure. When the Reynolds number is too large to resolve numerically the entire range of energetic scales, filtering will be used to eliminate the smaller (subgrid-scale) motions. Filtering Equation (1) introduces new terms, similar to Reynolds stress terms obtained in the Reynolds-averaged equations, that contain the effect of the subgrid-scale motions on the numerically resolved motions. We plan to use standard procedures to handle these terms and will introduce them into our numerical scheme at a later date. By taking the divergence of Equation (1), the following Poisson equation governing the pressure is obtained:

$$\nabla^2 p = -\nabla \cdot [(\underline{q} \cdot \nabla) \underline{q}] - (\nabla \cdot \underline{q})_t + \frac{1}{Re} \nabla^2 (\nabla \cdot \underline{q}) \quad (3)$$

Substituting Equation (2) into Equation (3) leads to the following pressure equation:

$$\nabla^2 p = -\nabla \cdot [(\underline{q} \cdot \nabla) \underline{q}] \quad (4)$$

The system of Equations (1) and (4) is equivalent to the original system, Equations (1) and (2), and is used here instead of the original set of equations. The vector equation (1) is solved subject to the periodicity condition in the  $x$  direction; a weak outflow condition

$$\frac{\partial u}{\partial y} = \frac{\partial w}{\partial y} = 0 \quad (5)$$

with  $\partial v / \partial y$  being determined from the continuity equation, is applied at the side boundaries of the computational domain ( $y = y_B$ ,  $y = y_b$ ), and a no-slip condition is applied at the bottom boundary,  $z = z_g$ , and the top



boundary,  $z = z_a$ , outside the jet region. In the jet region, the inflow condition

$$q(x, y, z_a) = \bar{f}(x, y) \quad (6)$$

is specified. Equation (4) is solved subject to the condition

$$\frac{\partial p}{\partial y} = 0 \quad (7)$$

at the side boundaries and subject to the Neumann boundary conditions determined from Equation (1) at the top and bottom boundaries.

### 3. Method of Solution

The finite difference approximations to Equations (1) and (4) are written at the mesh points of a staggered grid. For advancing the solution from time  $t^n$  to time  $t^{n+1}$ , where  $t^n = n\Delta t$ ,  $t^{n+1} = (n+1)\Delta t$  and  $\Delta t$  is the time step, the following first-order scheme is used:

$$\underline{q}^{n+1} = \underline{q}^n + \Delta t [-(\underline{q}^n \cdot \nabla) \underline{q}^n - \nabla p^n + \frac{1}{Re} \nabla^2 \underline{q}^n] \quad (8)$$

where  $p^n$  is determined so that mass conservation is assured at time  $t^{n+1}$ .

It is determined by solving the finite difference approximation to the equation

$$\nabla^2 p^n = -\nabla \cdot [(\underline{q}^n \cdot \nabla) \underline{q}^n] \quad . \quad (9)$$

This equation is solved by using a direct (noniterative) fast Laplace equation solver.

#### 4. Numerical Examples

The examples presented here are preliminary examples that have been solved using the developed computer code. A relatively coarse numerical mesh is used, and the Reynolds number is assumed to be low enough so that filtering is not required. The results presented here are not intended to be an accurate simulation of VTOL flow configurations. Nevertheless, they do indicate the main features of these flows.

For all the examples presented here, the plane  $y = y_j$  is assumed to be a plane of symmetry. Unless otherwise stated, the computational domain is defined by (see Figure 1)

$$\begin{aligned} 0 &= x_j \leq x \leq x_f = 1 \\ -2 &= y_B \leq y \leq y_b = 2 \\ 0 &= z_g \leq z \leq z_a = 1 \end{aligned}$$

where all dimensions are normalized by the jet diameter. The jet velocity profile in the direction of the jet axis is assumed to be given by

$$Q_j(r) = 1 - \frac{r^2}{R_j^2}$$

where  $R_j$  is the jet radius,  $r$  is the distance from the jet axis and velocities are normalized by the jet maximum velocity. The Reynolds number in the examples is based on the jet diameter and the maximum jet velocity.

##### Example 1:

In this example the jet axis is assumed to be normal to the ground plane ( $\alpha = 90^\circ$ ) and there is assumed to be no cross flow ( $V = 0$ ). The Reynolds number is given by  $Re = 300$ . An  $18 \times 72 \times 18$  ( $x, y, z$ ) mesh is used.

Figures 3 through 12 show the main features of the flow generated by a row of vertical jets impinging on the ground. The velocity vectors in the planes  $x = x_j$ ,  $x = x_f$  are shown in Figures 3 and 4, respectively. The fan-shaped fountain that results from the collision of the two wall jets is apparent in Figure 4. The jet, the wall jet and the fountain are apparent in Figure 5. In both Figures 5 and 6 a downward motion exists as the plane  $x = x_j$  is approached, while an upward motion exists as the plane  $x = x_f$  is approached. However, the relative magnitudes of these motions are reversed in the two

figures. Figure 5 indicates that the downward motion in the jet is greater than the upward motion in the fountain. The plane of Figure 6 does not pass through the jet. There, the fountain upward motion is relatively stronger than the downward motion at  $x = x_j$ . Figures 7 through 10 are pressure contours that indicate high-pressure areas in the zones of jet-ground impingement, wall jet-wall jet collision and fountain impingement on the upper boundary. Figures 11 and 12 are contour plots for the vorticity components.

Example 2:

In this example the jet axis is assumed to be inclined at an angle  $\alpha = 60^\circ$  to the ground. A cross flow of  $V = 0.2$  is also assumed. The Reynolds number is given by  $Re = 300$ . An  $18 \times 72 \times 18$  ( $x, y, z$ ) mesh is used.

Figures 13 through 22 show the main features of the flow generated by a row of inclined jets impinging on the ground in a cross flow. In Figure 13 the ground vortex formed by the interaction of the cross flow and the wall jet is apparent. The effect of the cross flow on the fan-shaped fountain is shown in Figure 14, where it is no longer symmetric.

For the problem of a jet in a cross flow, two basic configurations are relevant to VTOL aerodynamics. In the first configuration, the jet impinges on the ground. The main features of this flow are indicated in Example 2. A second configuration results as the distance between the aircraft and the ground becomes large and/or as the forward aircraft speed becomes large. In this case, the jet does not impinge on the ground. This configuration is used in the following example.

Example 3:

In this example  $\alpha = 90^\circ$ ,  $V = 0.7$  and  $Re = 60$ . A  $7 \times 28 \times 14$  mesh is used. The computational domain is defined by

$$\begin{aligned} 0 &= x_j \leq x \leq x_f = 1 \\ -2 &= y_B \leq y \leq y_b = 2 \\ 0 &= z_g \leq z \leq z_a = 2 \end{aligned}$$

Figures 23 through 32 show the main features of this flow. Figure 23 indicates that the jet changes its direction before it reaches the ground. As

indicated in Figure 24, no fountain flow develops in this example since there are no wall jets. The double vortex generated by the jet-cross flow interaction is shown in Figure 26. As indicated by the pressure contours shown in Figure 27, a high-pressure region develops upstream of the jet, while a low-pressure region develops downstream of the jet in its wake.

Example 4:

This example is the same as Example 3 with the exception that  $V = 0$ . Figures 33 through 42, which show the main features of the flow for this case, thus allow comparison between the zero cross-flow case (given here) and a cross-flow case (Example 3) for the same configuration.

Example 5:

This example is similar to Example 1 ( $\alpha = 90^\circ$ ,  $V = 0$ ). However, a relatively fine computational mesh is used here, which allows the use of a relatively large Reynolds number ( $Re = 600$ ). Symmetry is assumed in the  $x$  direction in addition to the  $y$  direction. Therefore, the computational domain is defined by

$$\begin{aligned} 0 &= x_j \leq x \leq x_f = 1 \\ 0 &= y_j \leq y \leq y_b = 2 \\ 0 &= z_g \leq z \leq z_a = 1 \end{aligned}$$

A  $24 \times 48 \times 24$  computational mesh is used.

The results of this calculation are indicated in Figures 43 through 52. Qualitatively similar effects to those observed in the first example are indicated. However, certain effects, such as the propagation of the initial vortex, while observed for the high-Reynolds-number, fine-mesh calculation (see Figure 53) are not observed for the low-Reynolds-number, coarse-mesh calculation (see Figure 54).

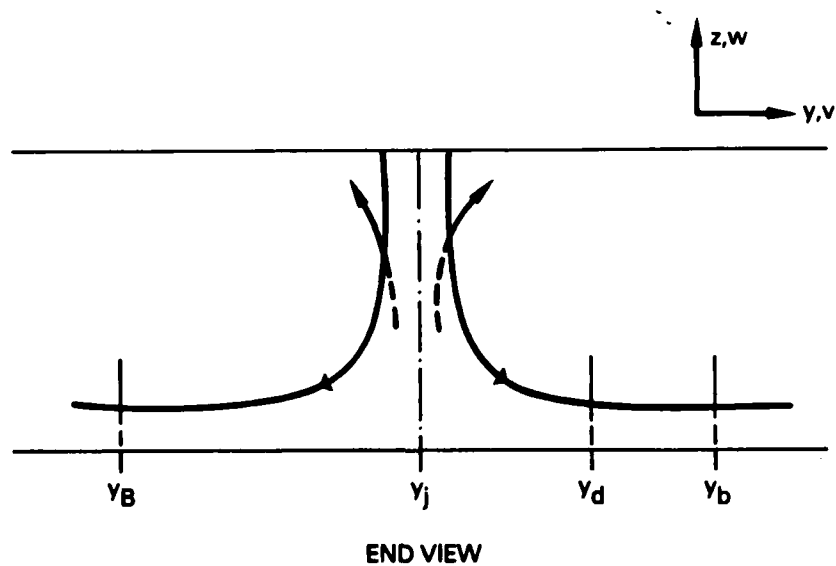
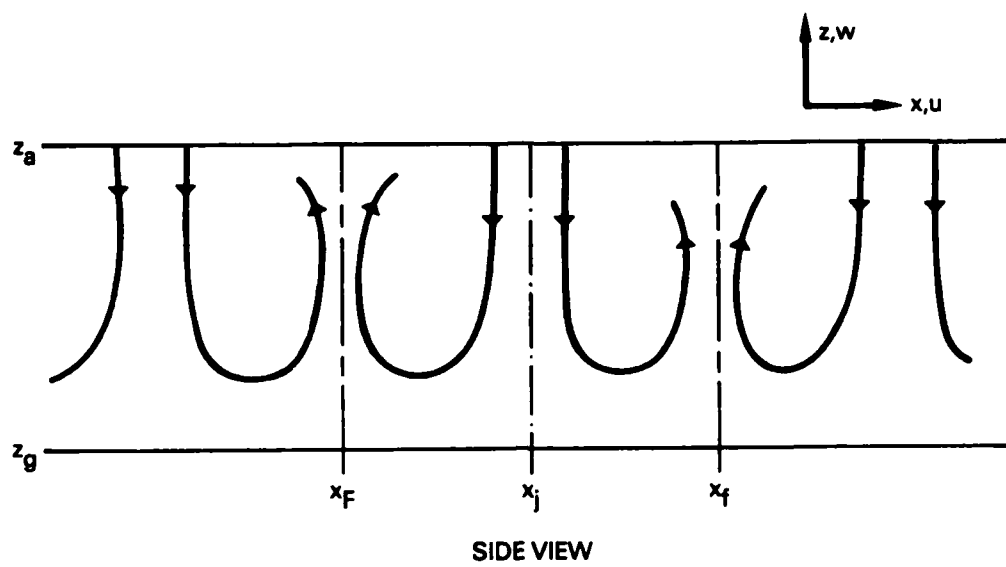


Figure 1. Model Problem for a Hovering VTOL Aircraft

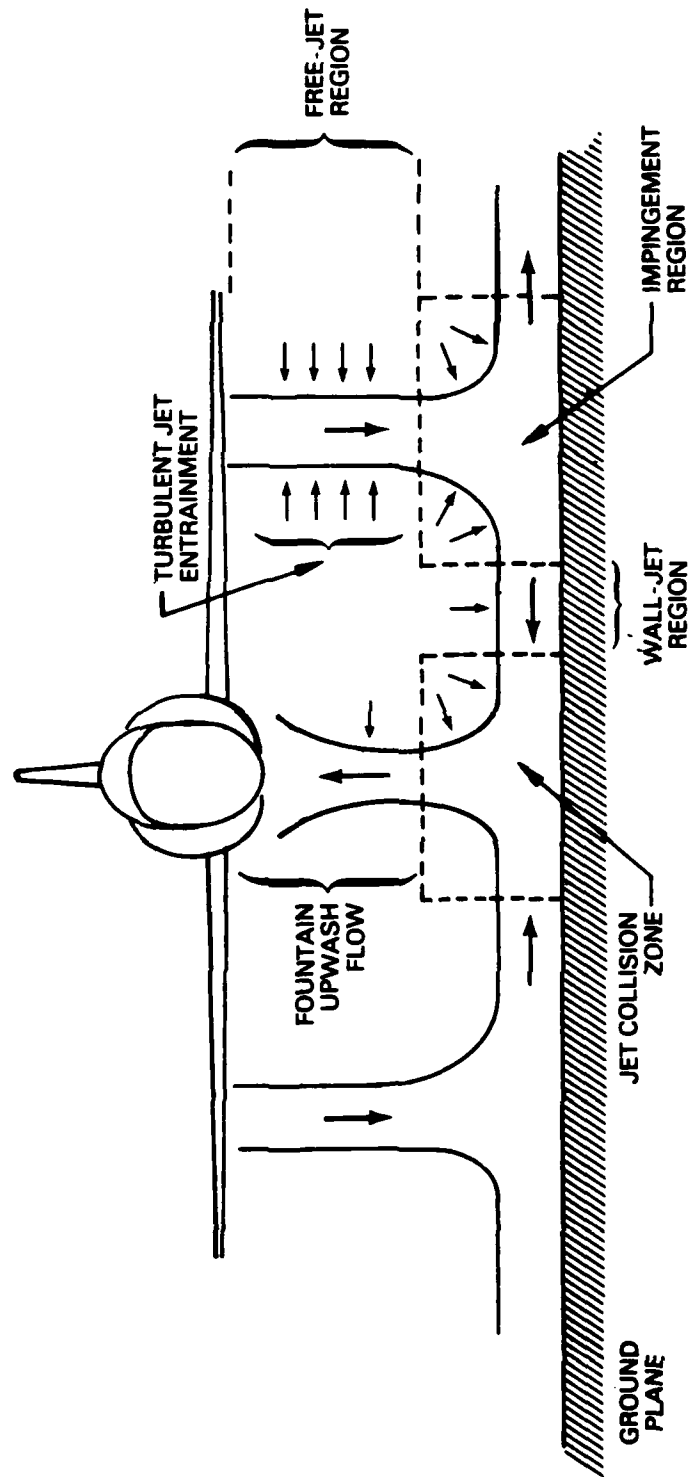


Figure 2. Schematic of Flow Field About a Hovering VTOL Aircraft

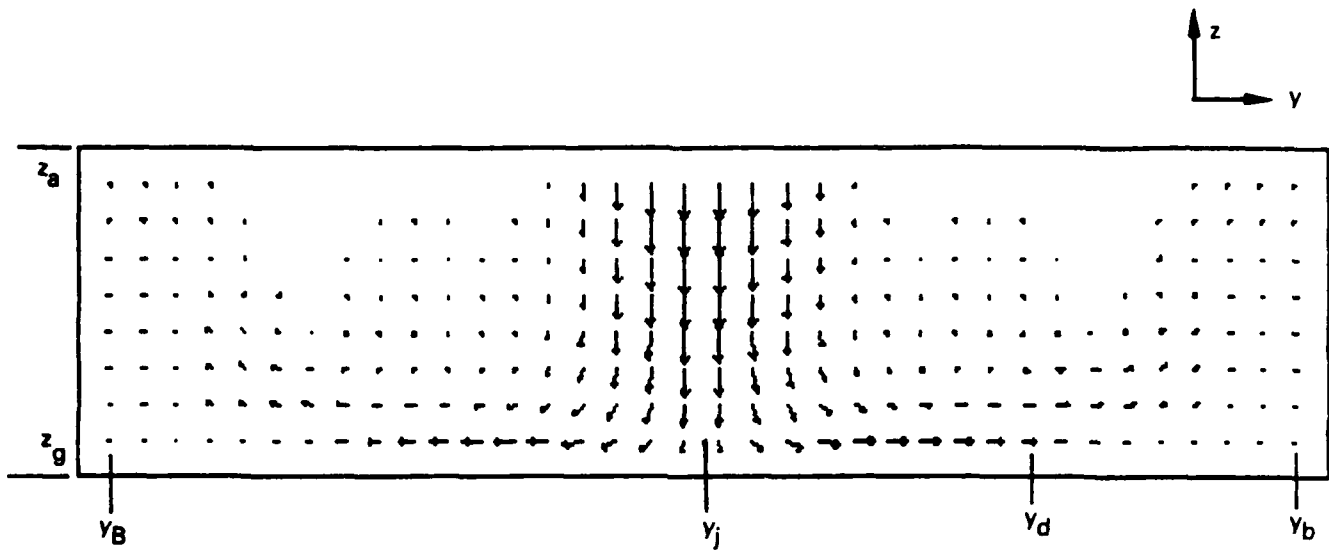


Figure 3. Example 1: Velocity Vectors in the Plane  $x = x_j$

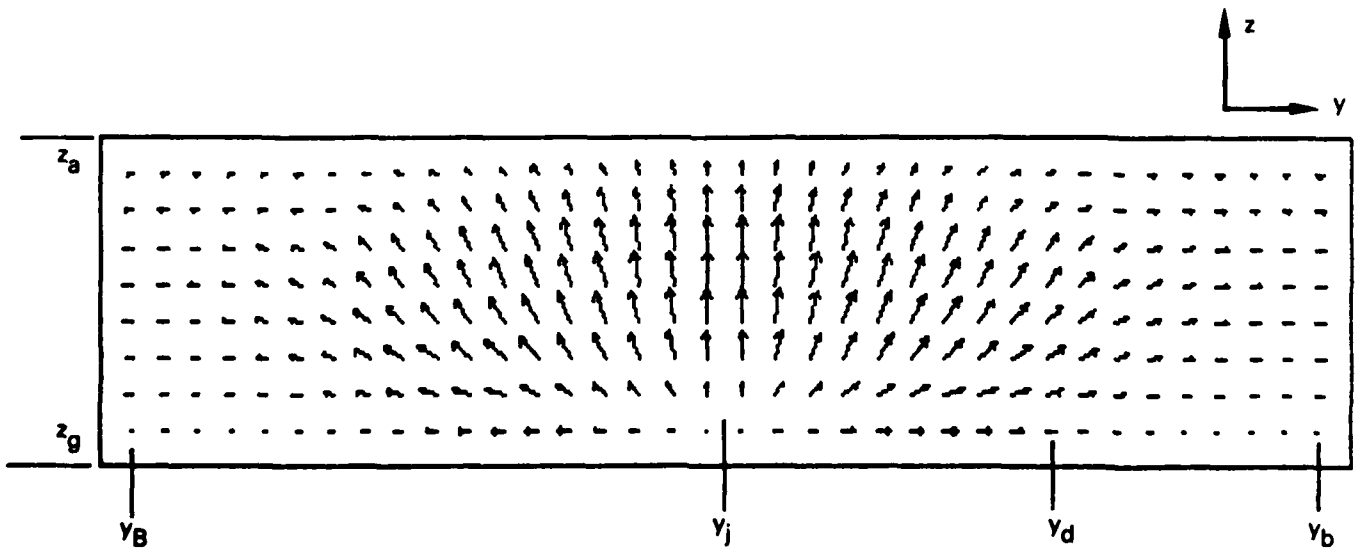


Figure 4. Example 1: Velocity Vectors in the Plane  $x = x_f$



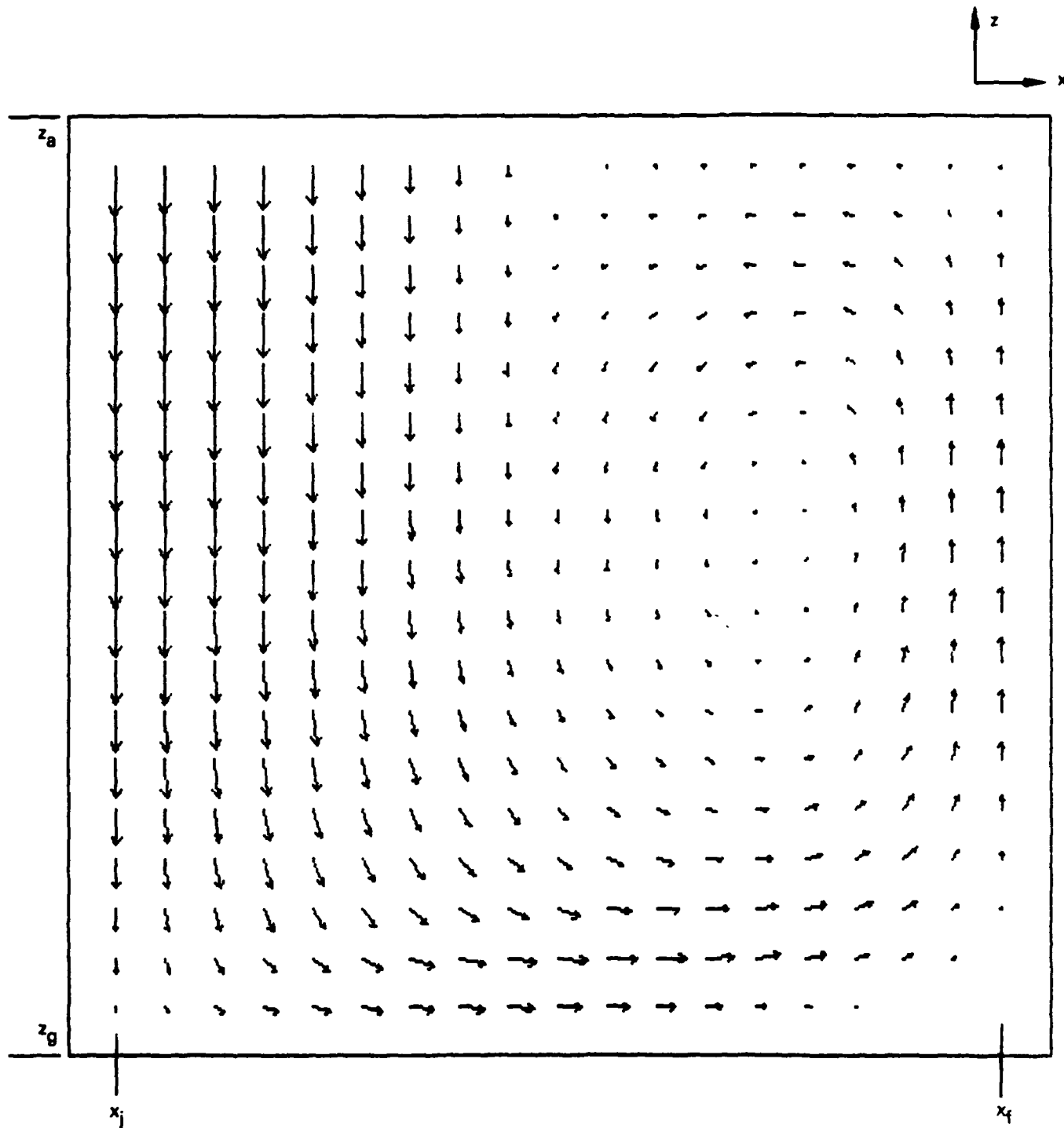


Figure 5. Example 1: Velocity Vectors in the Plane  $y = y_j$

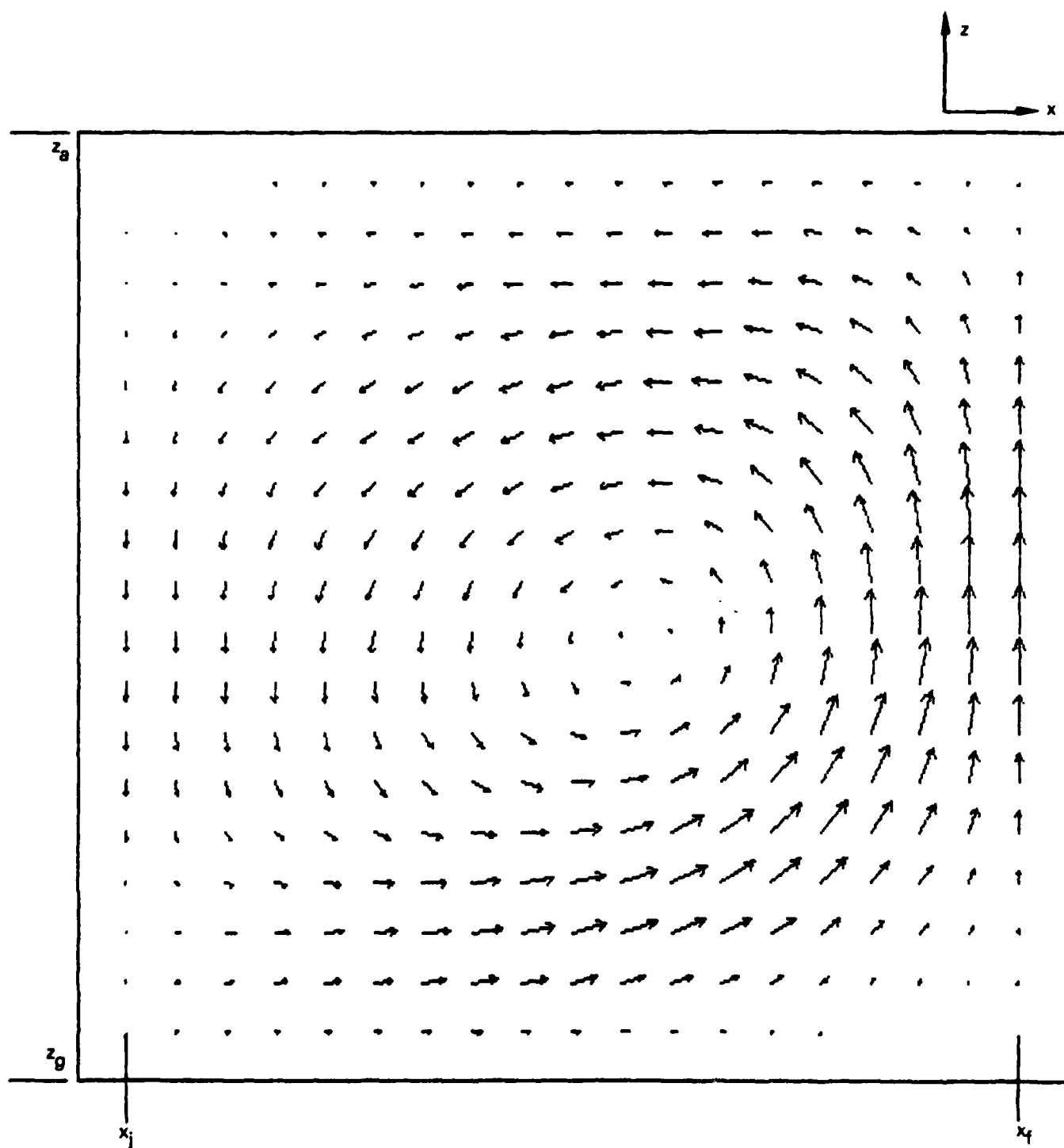


Figure 6. Example 1: Velocity Vectors in the Plane  $y = y_d$

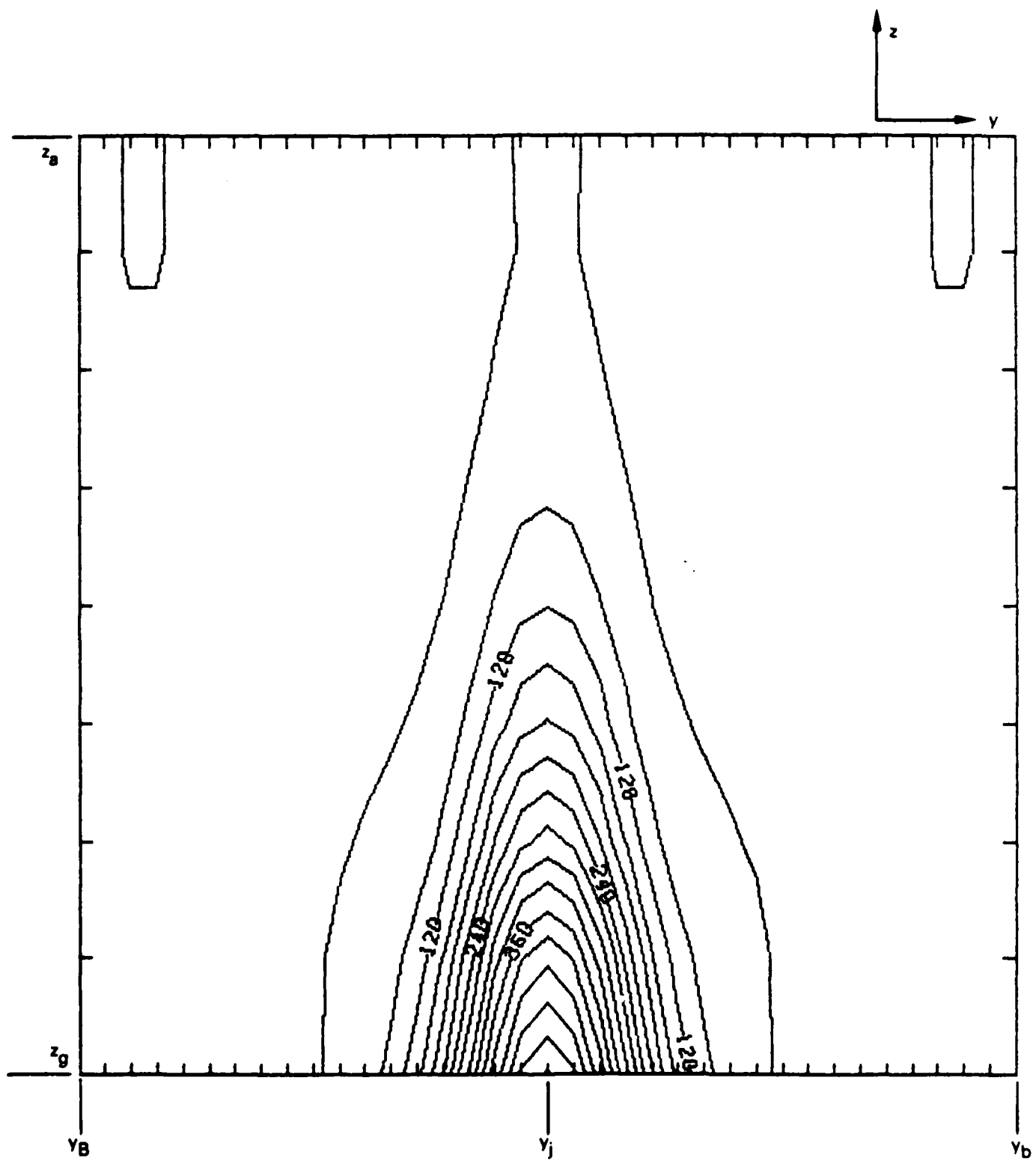


Figure 7. Example 1: Pressure Contours in the Plane  $x = x_j$

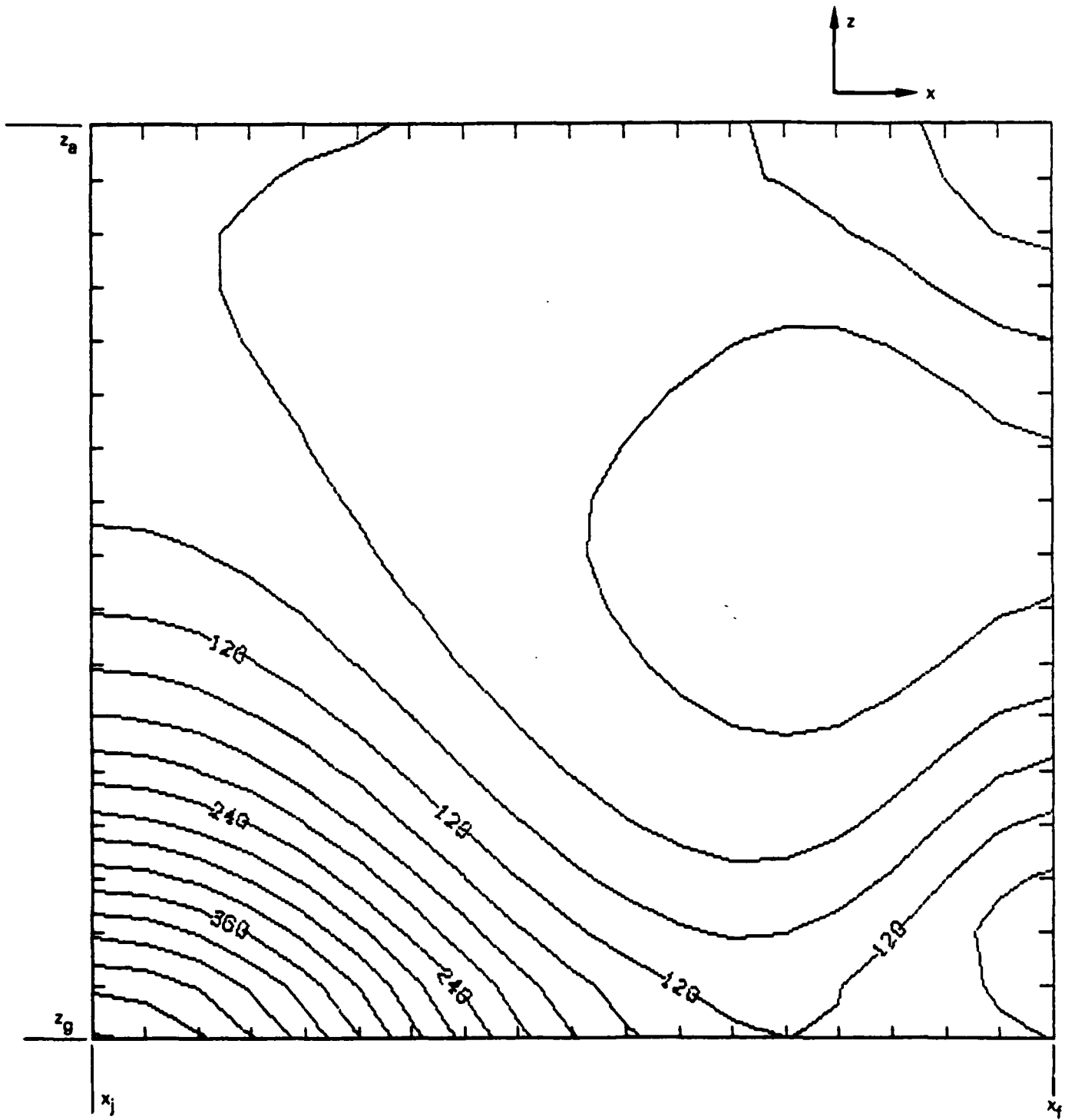


Figure 8. Example 1: Pressure Contours in the Plane  $y = y_j$

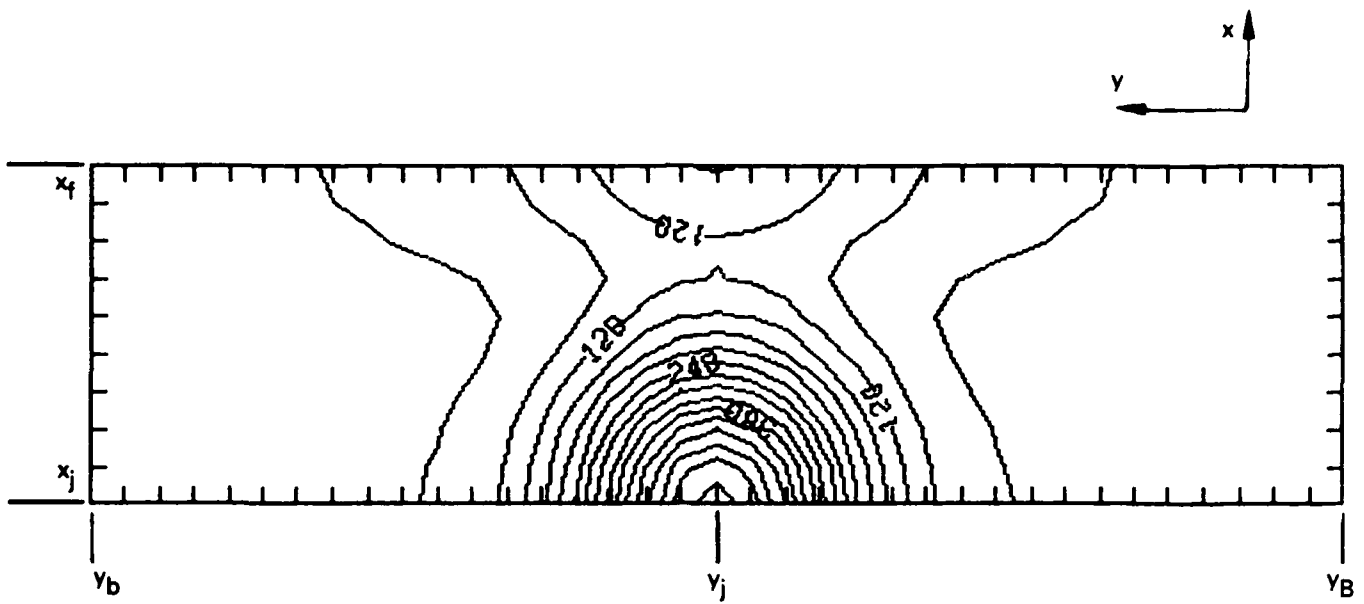


Figure 9. Example 1: Pressure Contours in the Plane  $z = z_g$

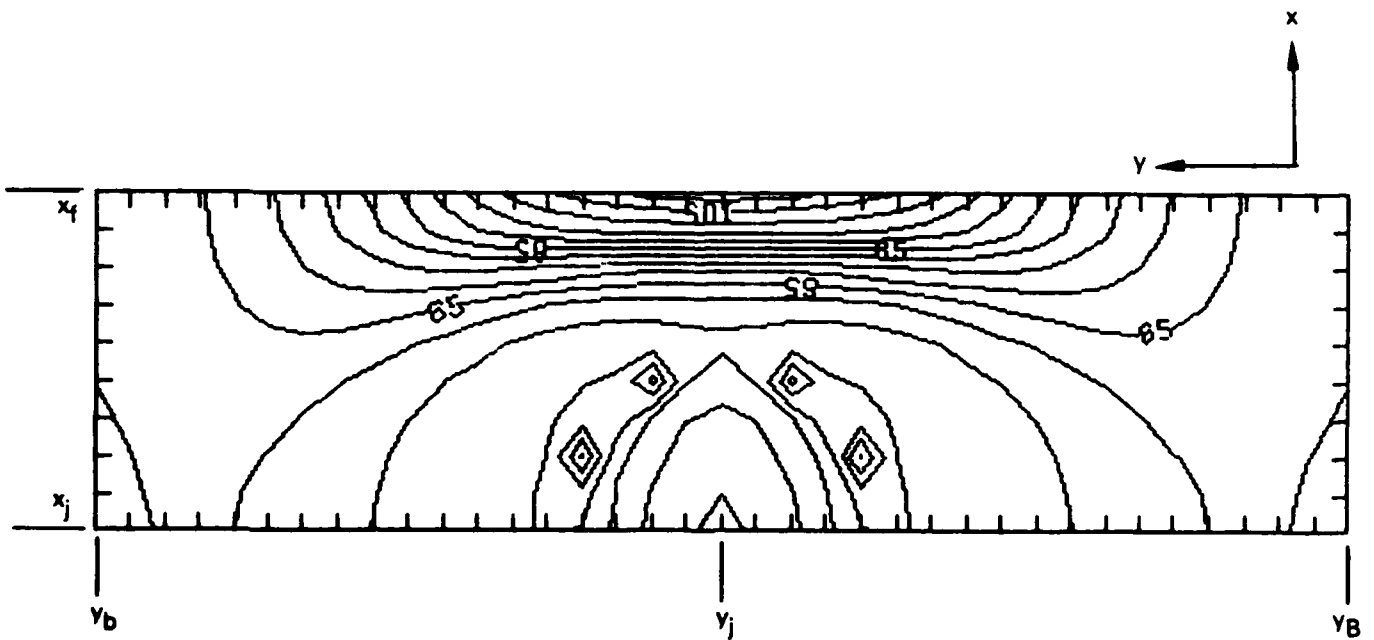


Figure 10. Example 1: Pressure Contours in the Plane  $z = z_a$

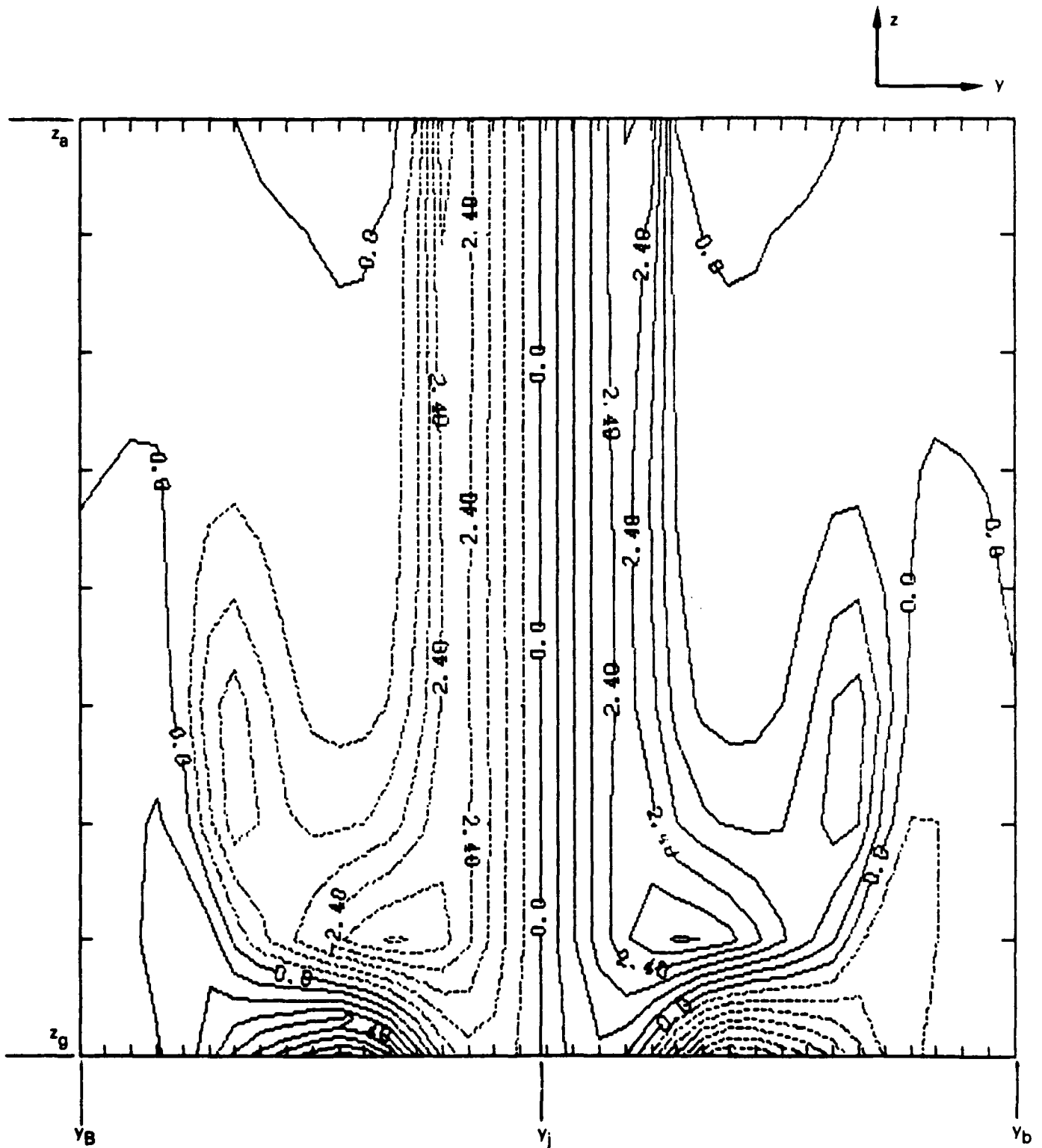


Figure 11. Example 1: x-Vorticity Component in the Plane  $x = x_j$

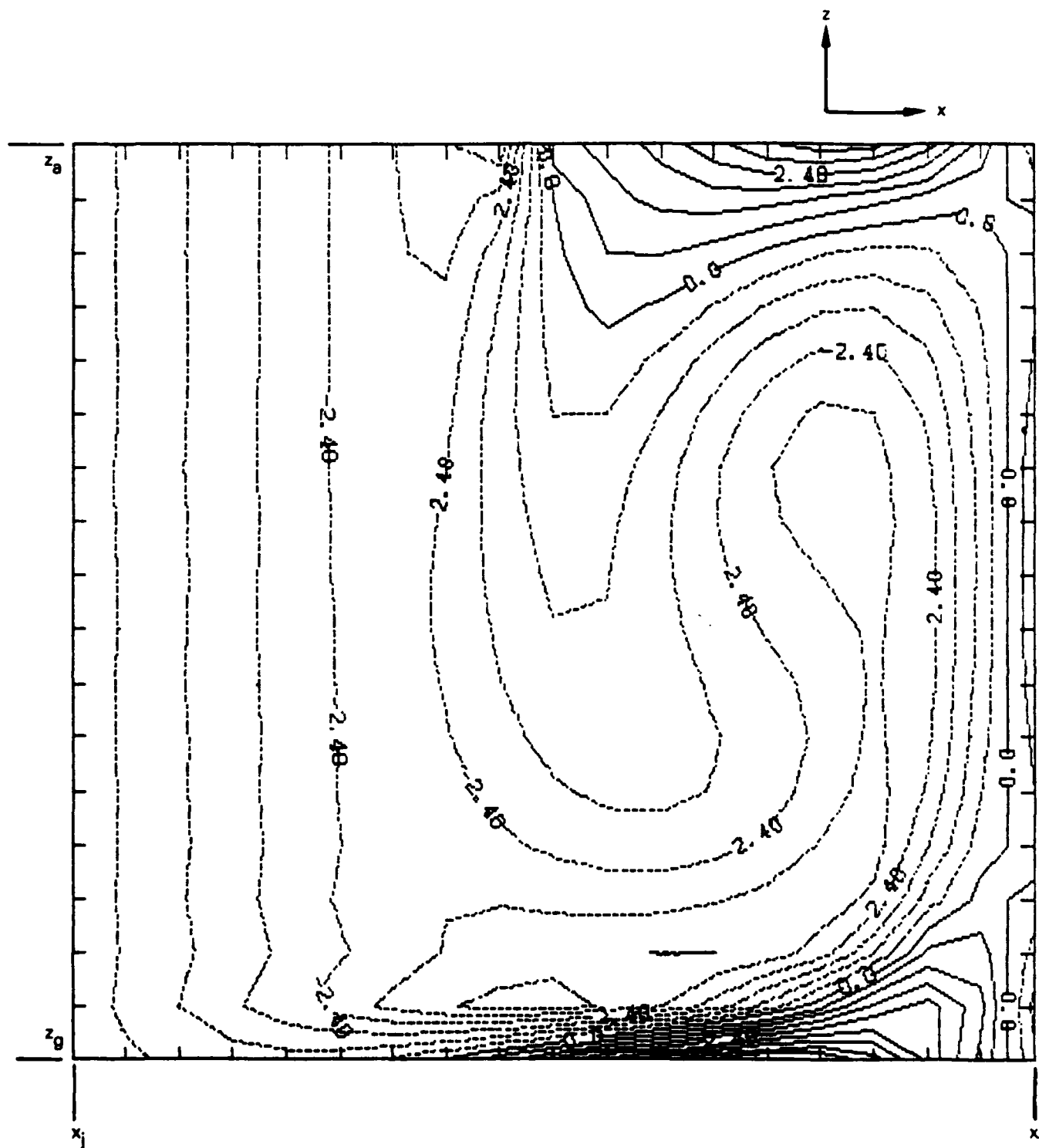


Figure 12. Example 1:  $y$ -Vorticity Component in the Plane  $y = y_j$

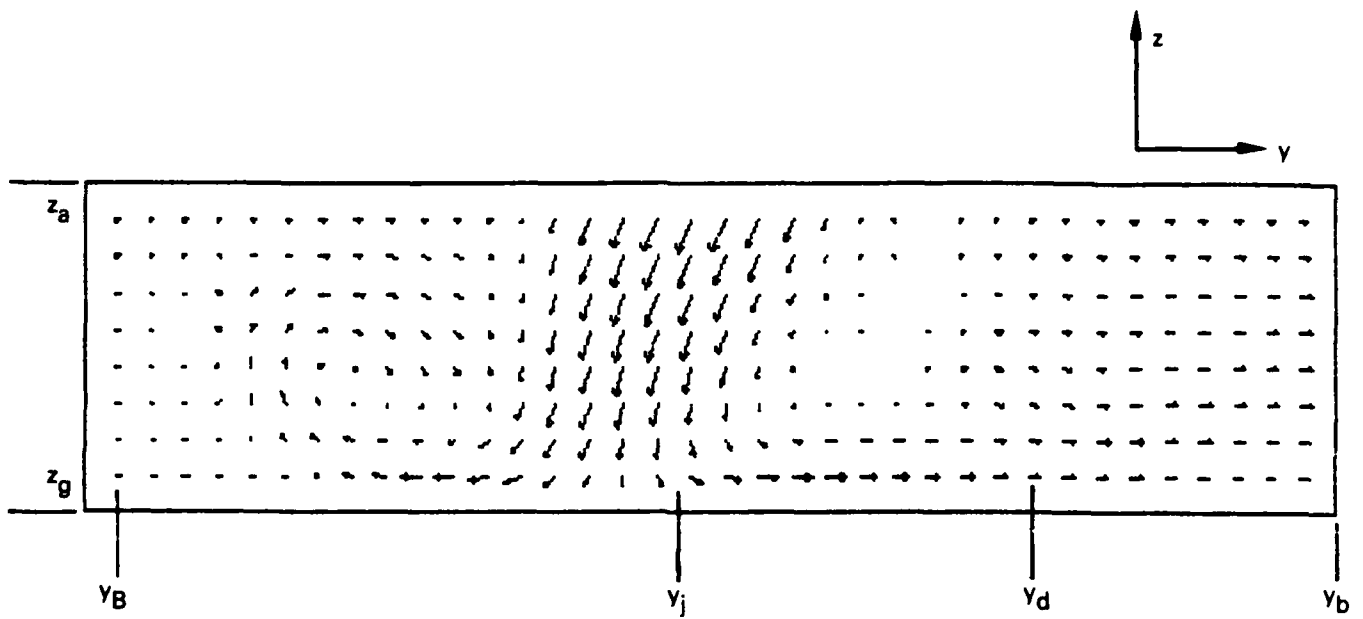


Figure 13. Example 2: Velocity Vectors in the Plane  $x = x_j$

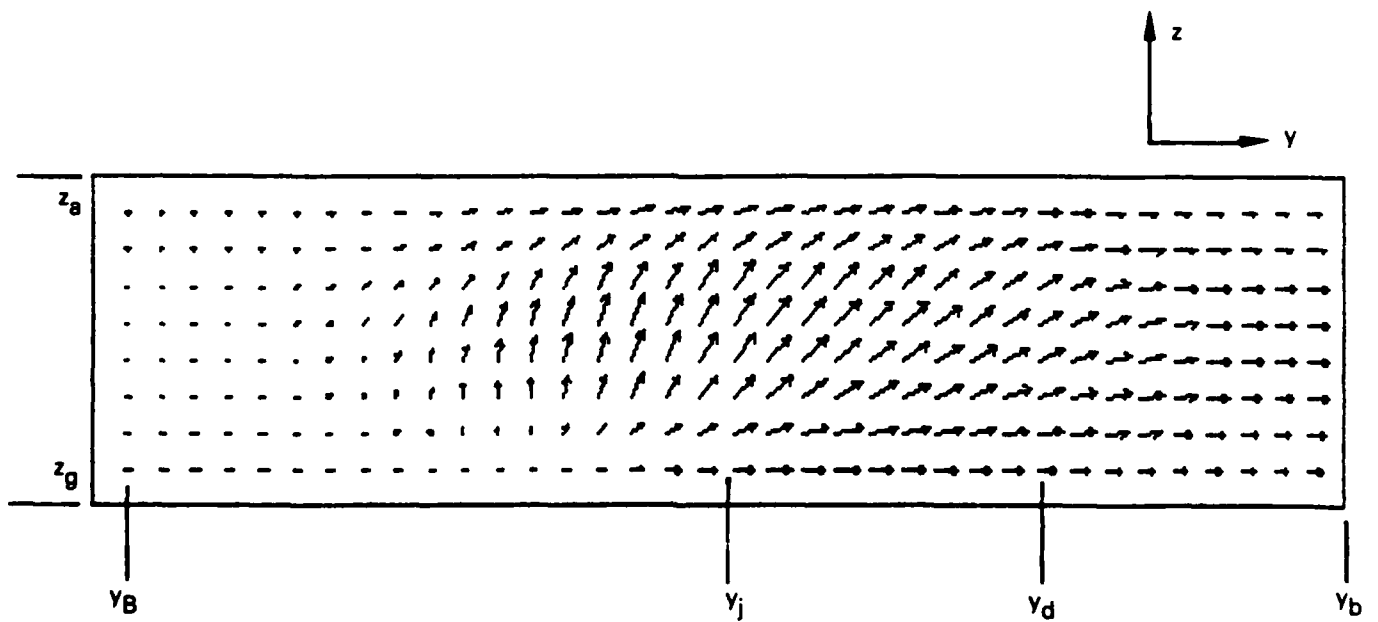


Figure 14. Example 2: Velocity Vectors in the Plane  $x = x_f$



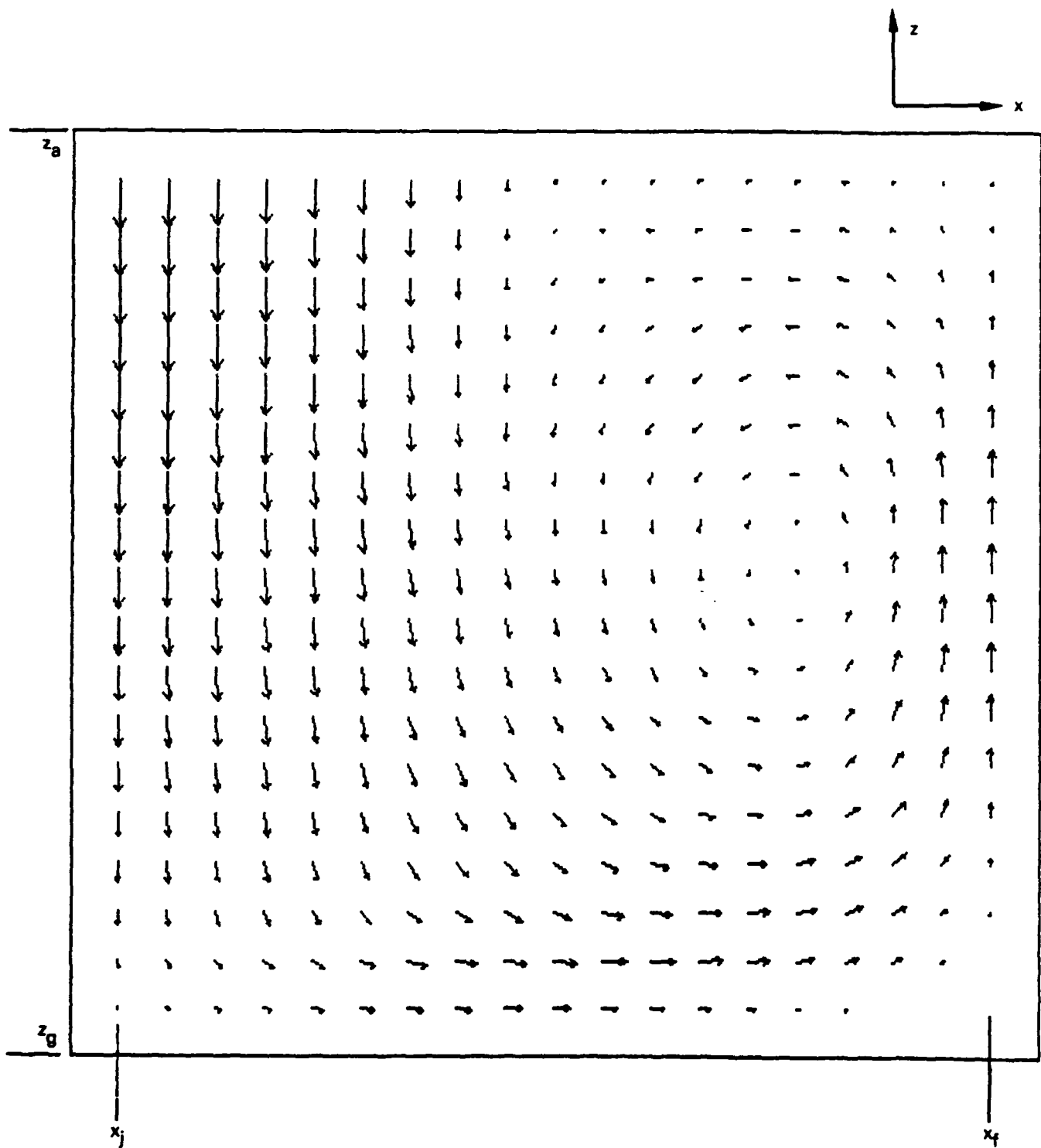


Figure 15. Example 2: Velocity Vectors in the Plane  $y = y_j$

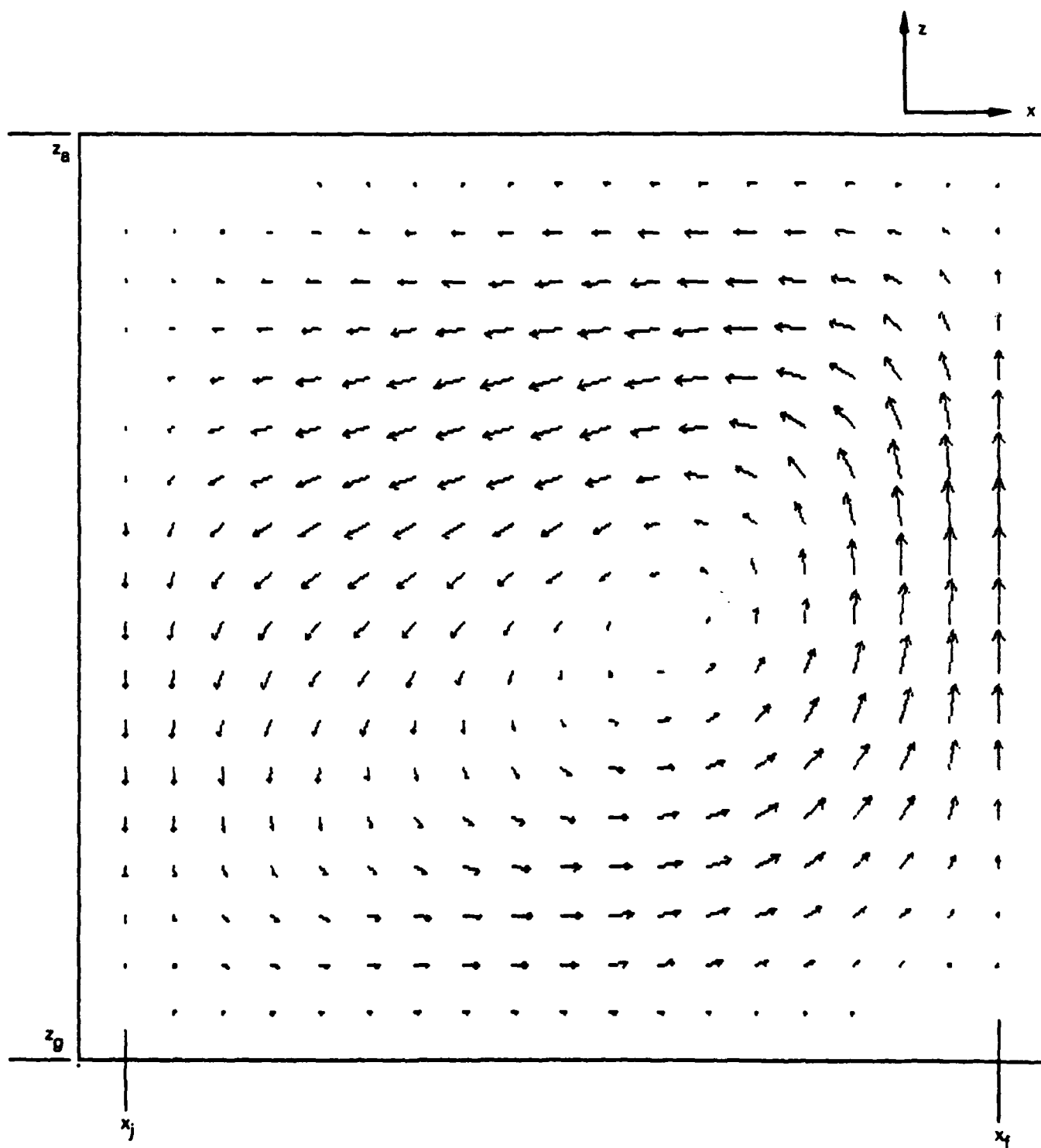


Figure 16. Example 2: Velocity Vectors in the Plane  $y = y_d$

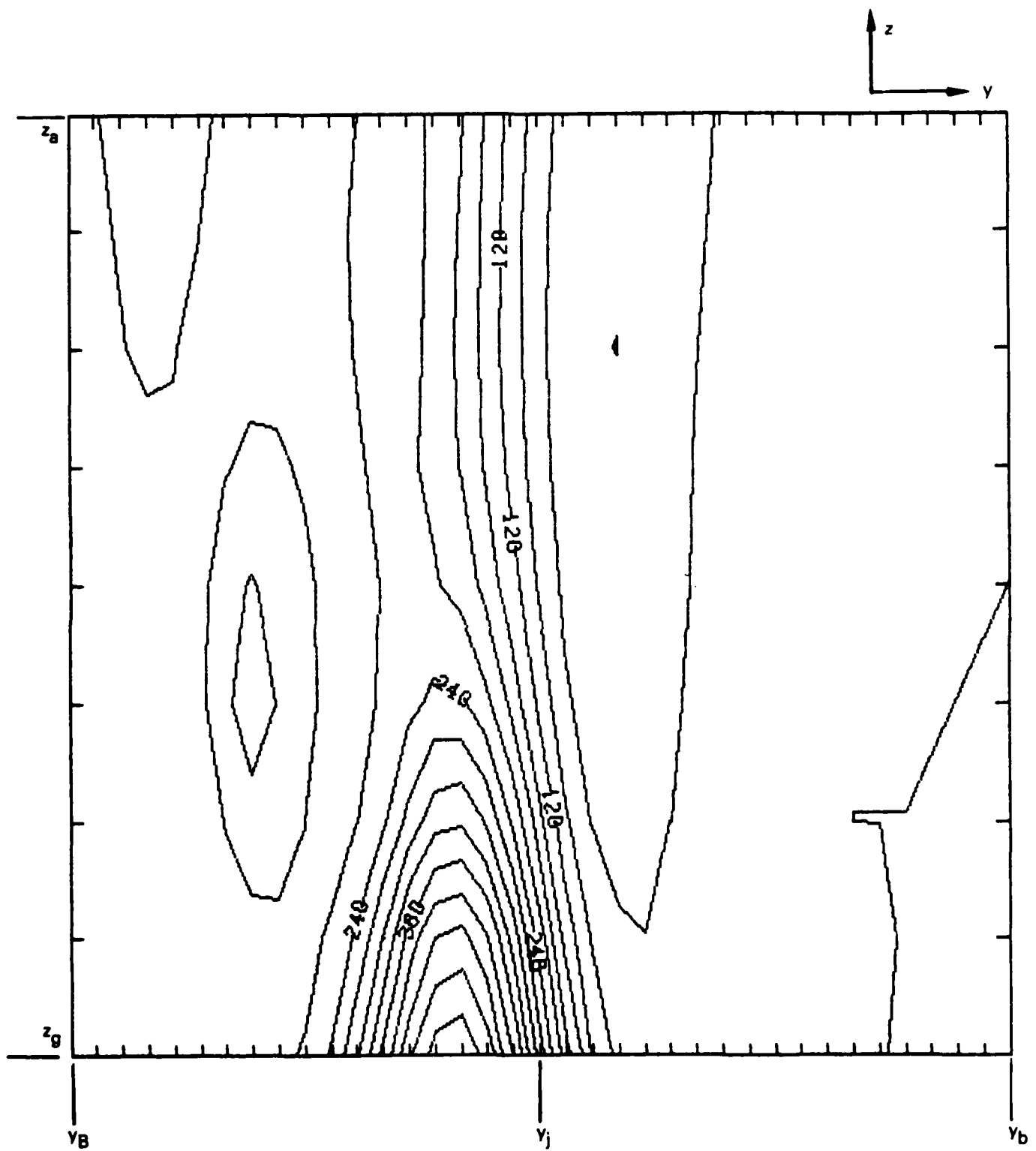


Figure 17. Example 2: Pressure Contours in the Plane  $x = x_j$

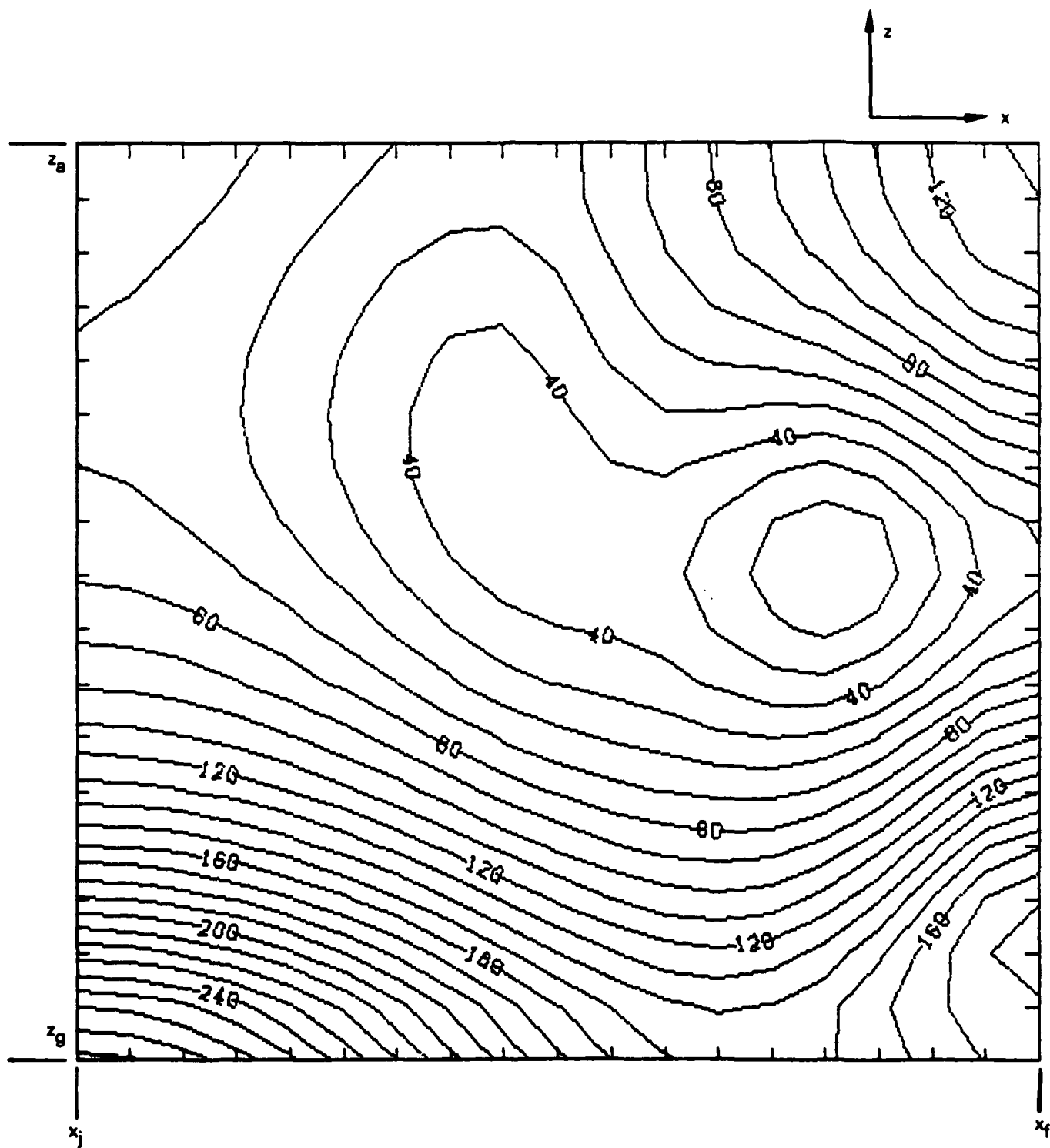


Figure 18. Example 2: Pressure Contours in the Plane  $y = y_j$

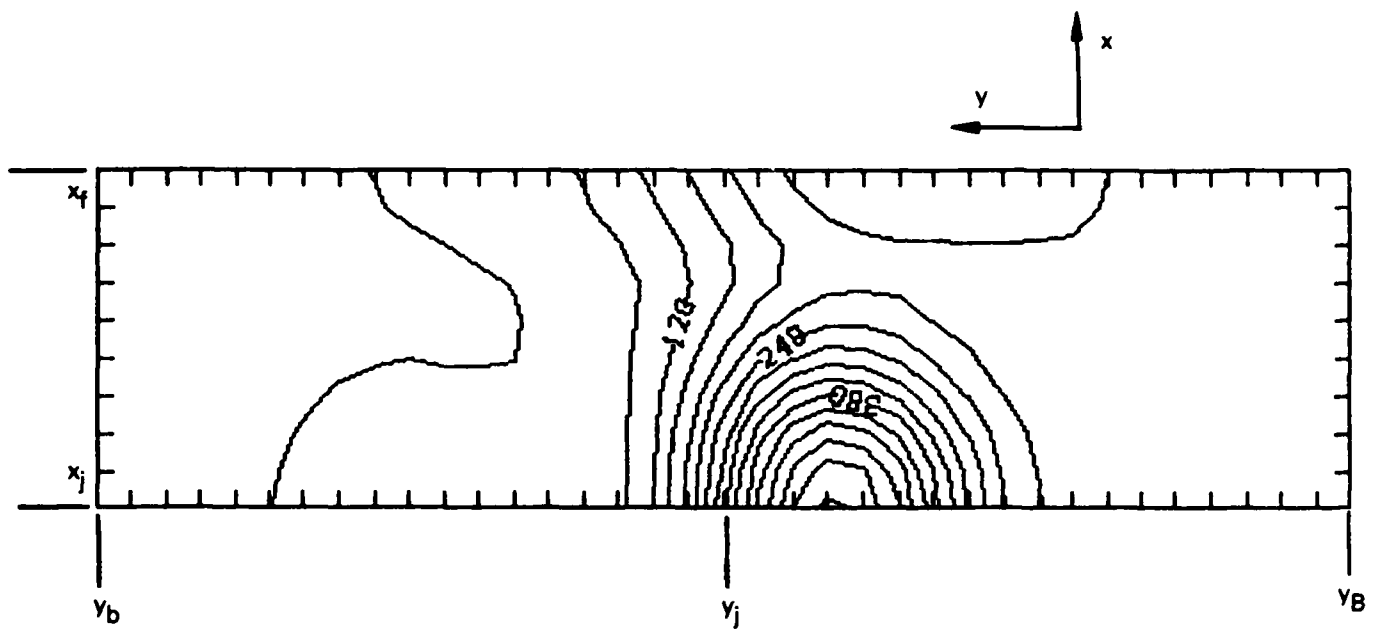


Figure 19. Example 2: Pressure Contours in the Plane  $z = z_g$

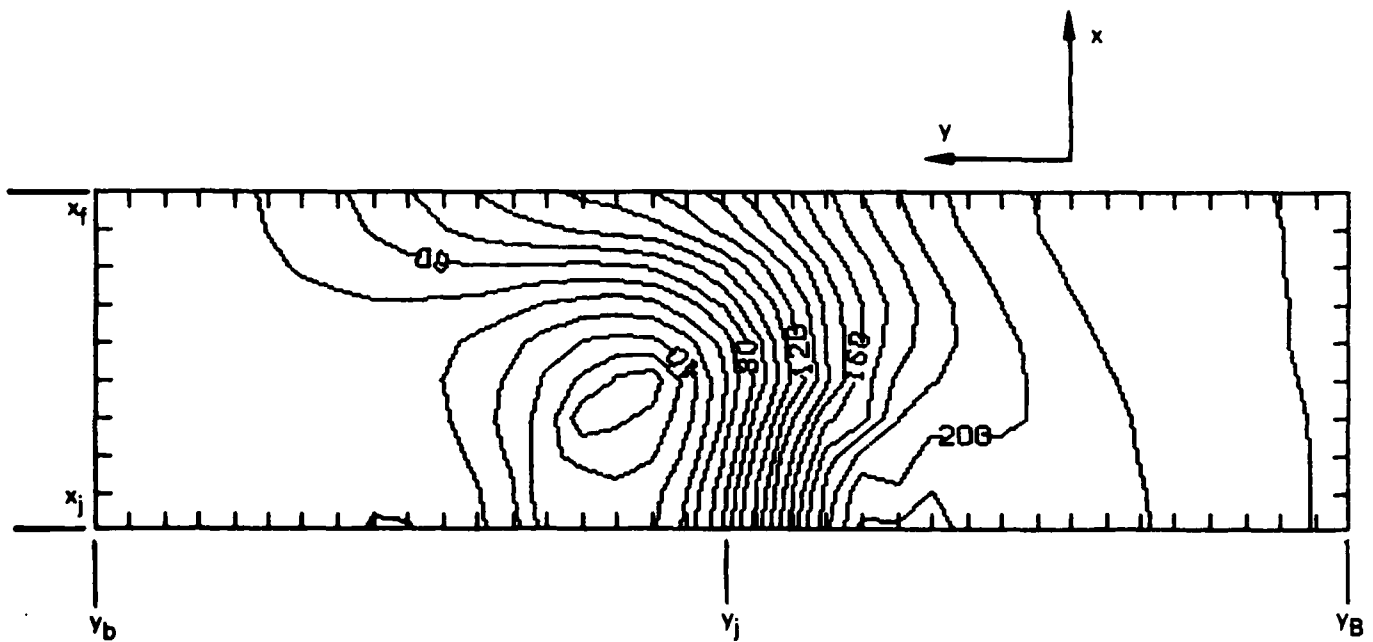


Figure 20. Example 2: Pressure Contours in the Plane  $z = z_g$

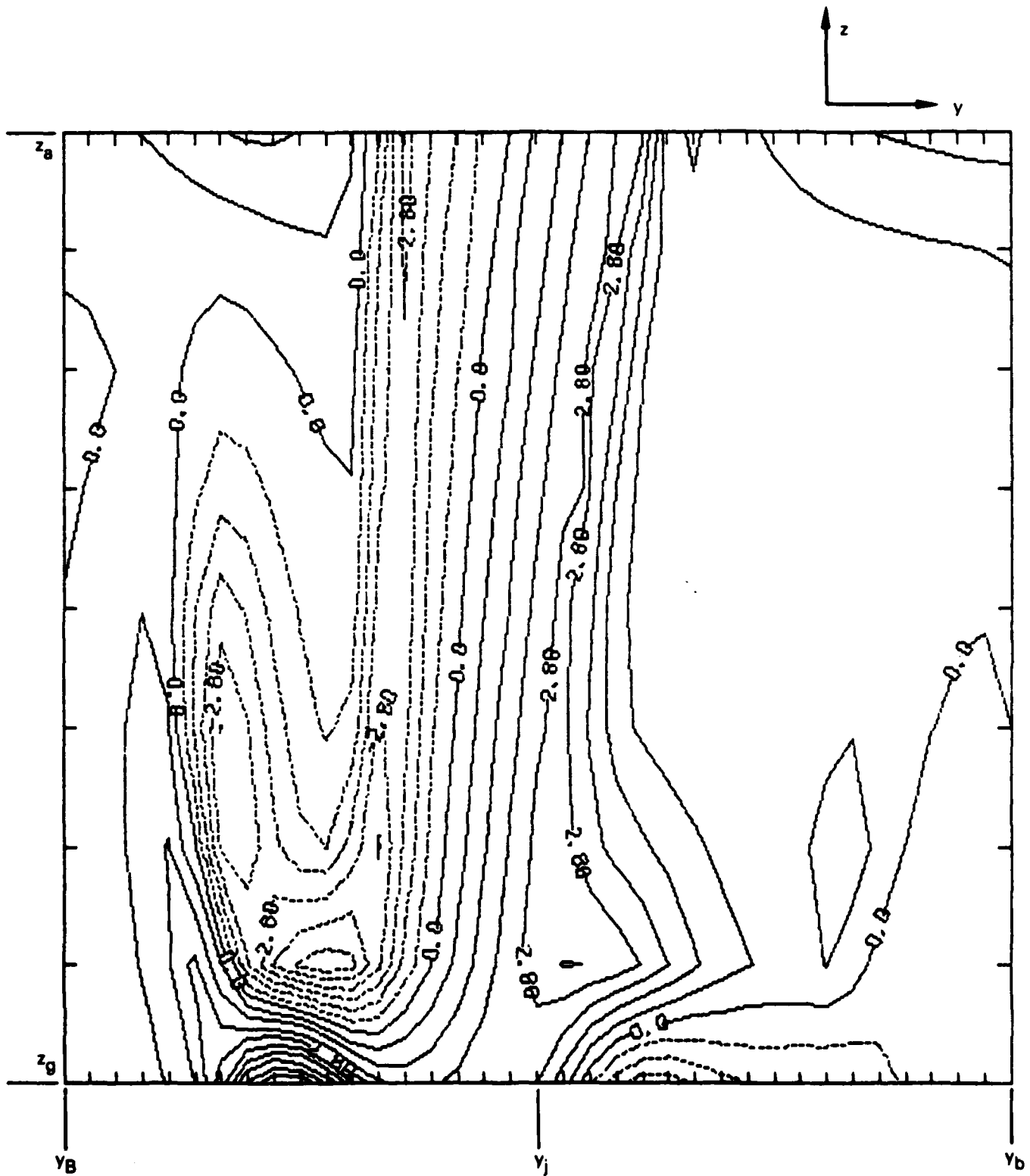


Figure 21. Example 2: x-Vorticity Component in the Plane  $x = x_j$

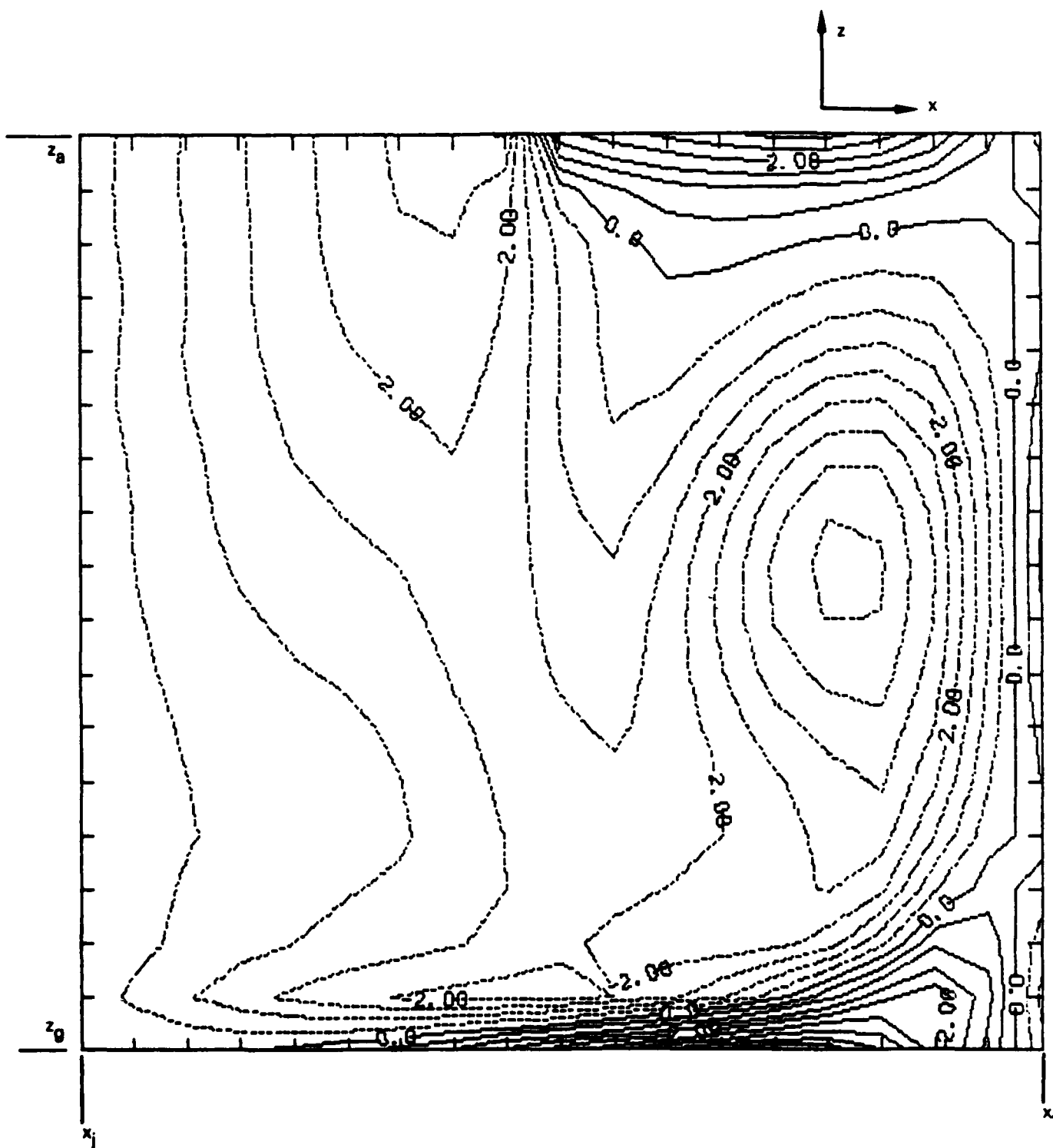


Figure 22. Example 2: y-Vorticity Component in the Plane  $y = y_j$

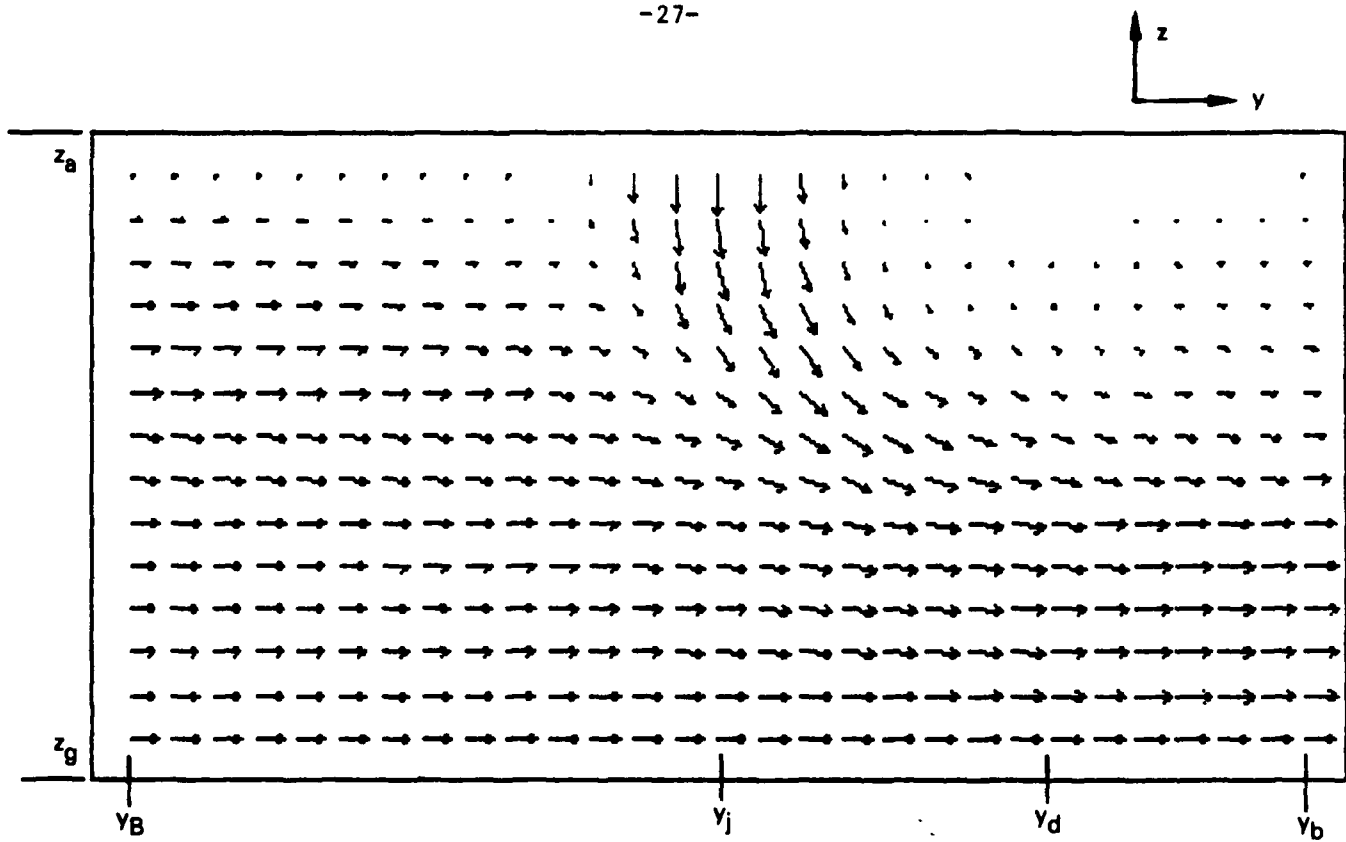


Figure 23. Example 3: Velocity Vectors in the Plane  $x = x_j$

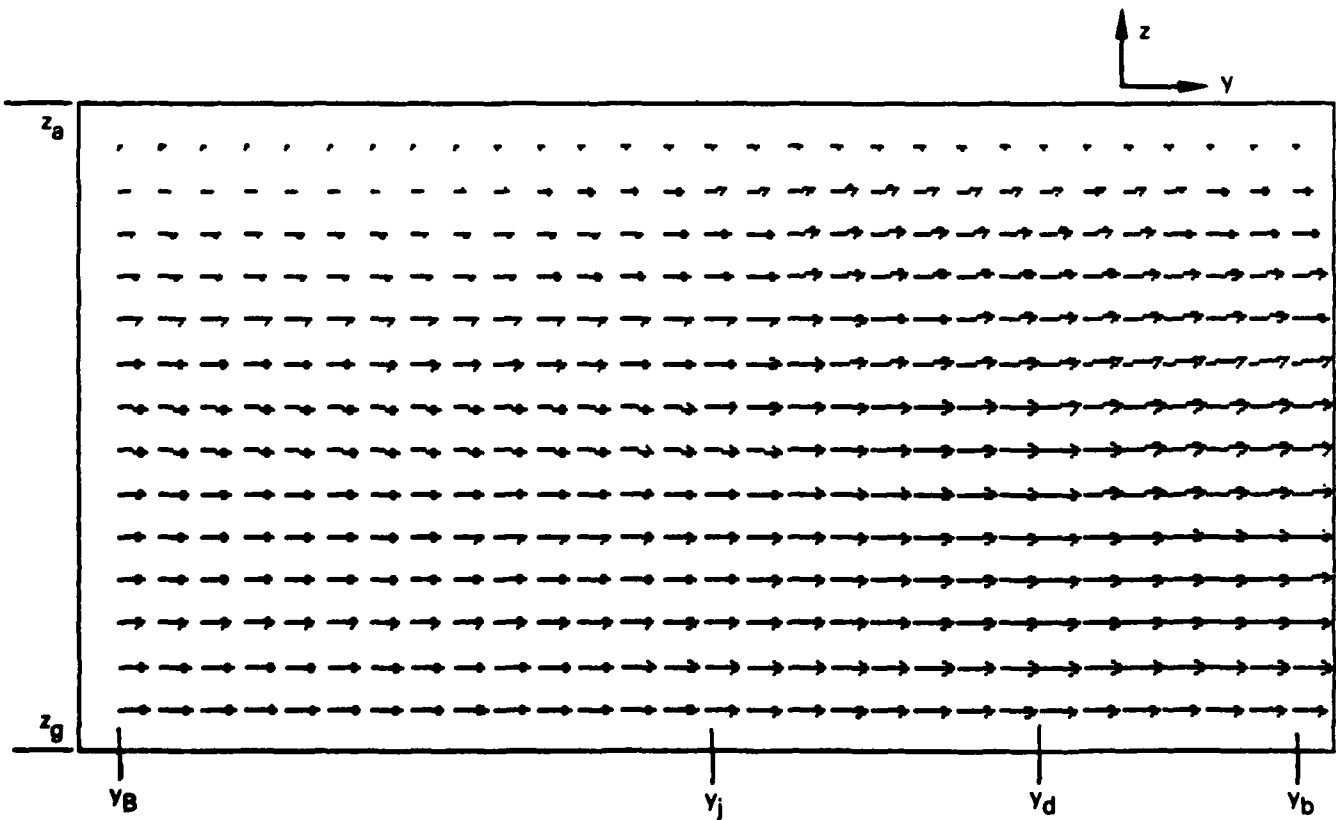


Figure 24. Example 3: Velocity Vectors in the Plane  $x = x_f$



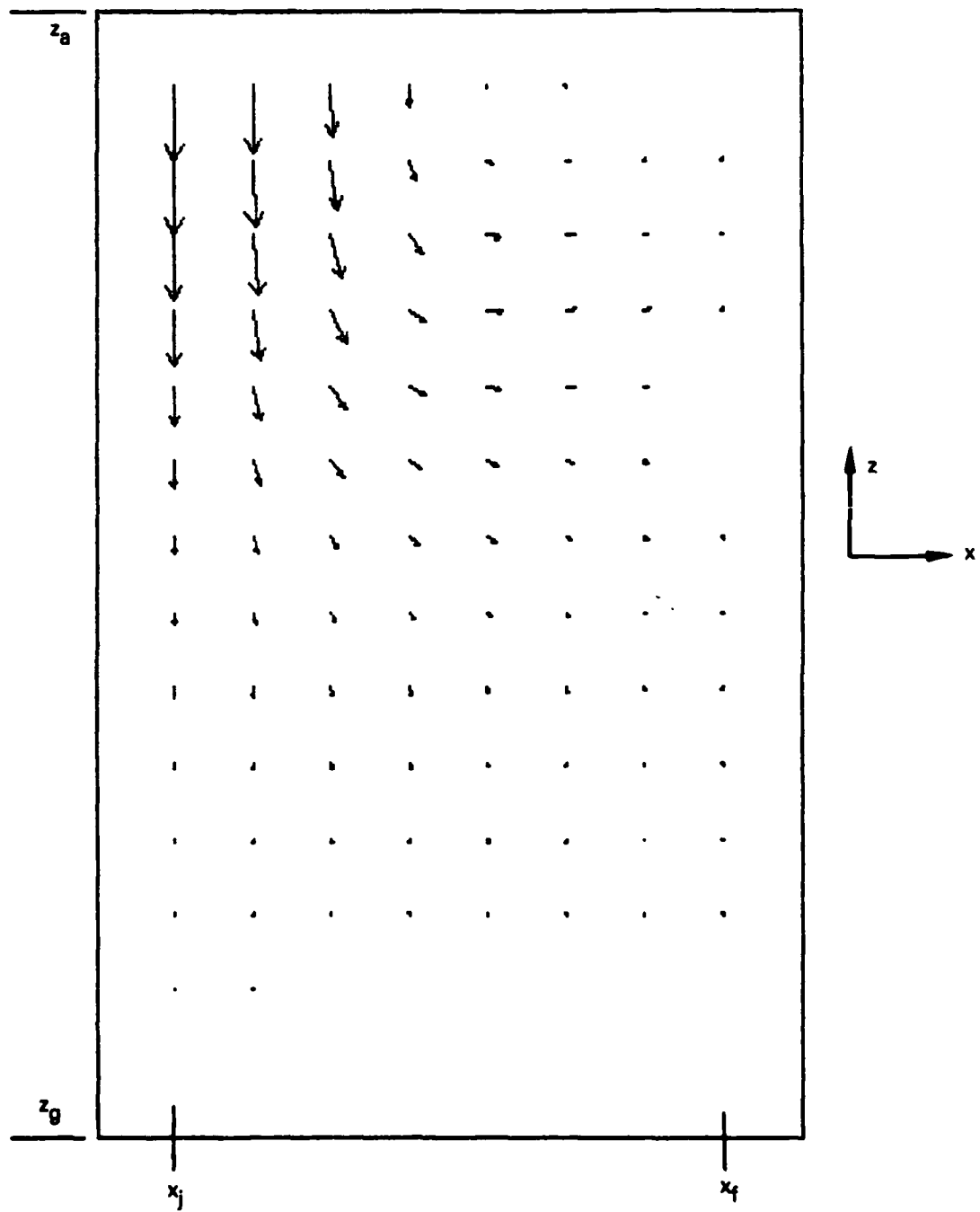


Figure 25. Example 3: Velocity Vectors in the Plane  $y = y_j$

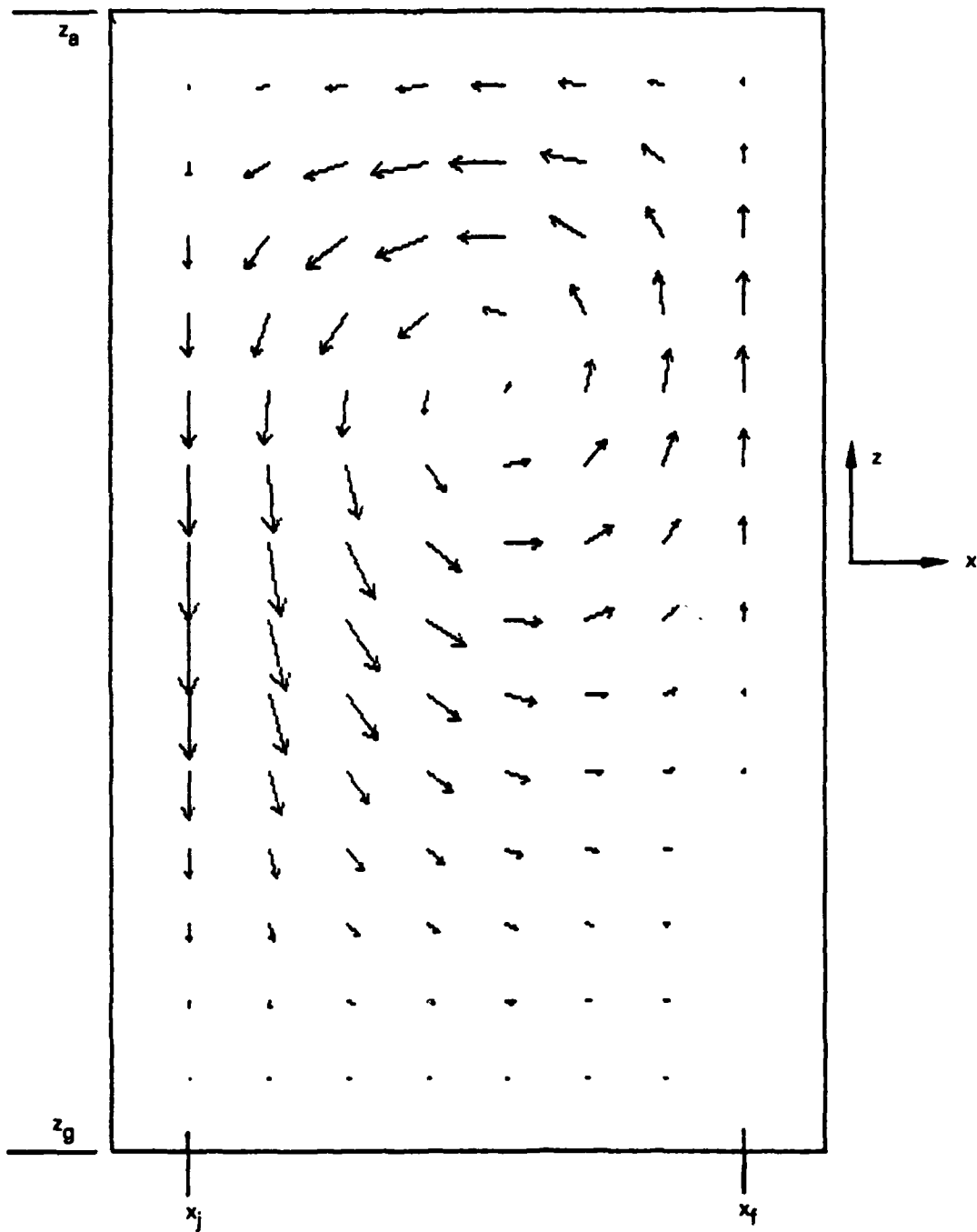


Figure 26. Example 3: Velocity Vectors in the Plane  $y = y_d$

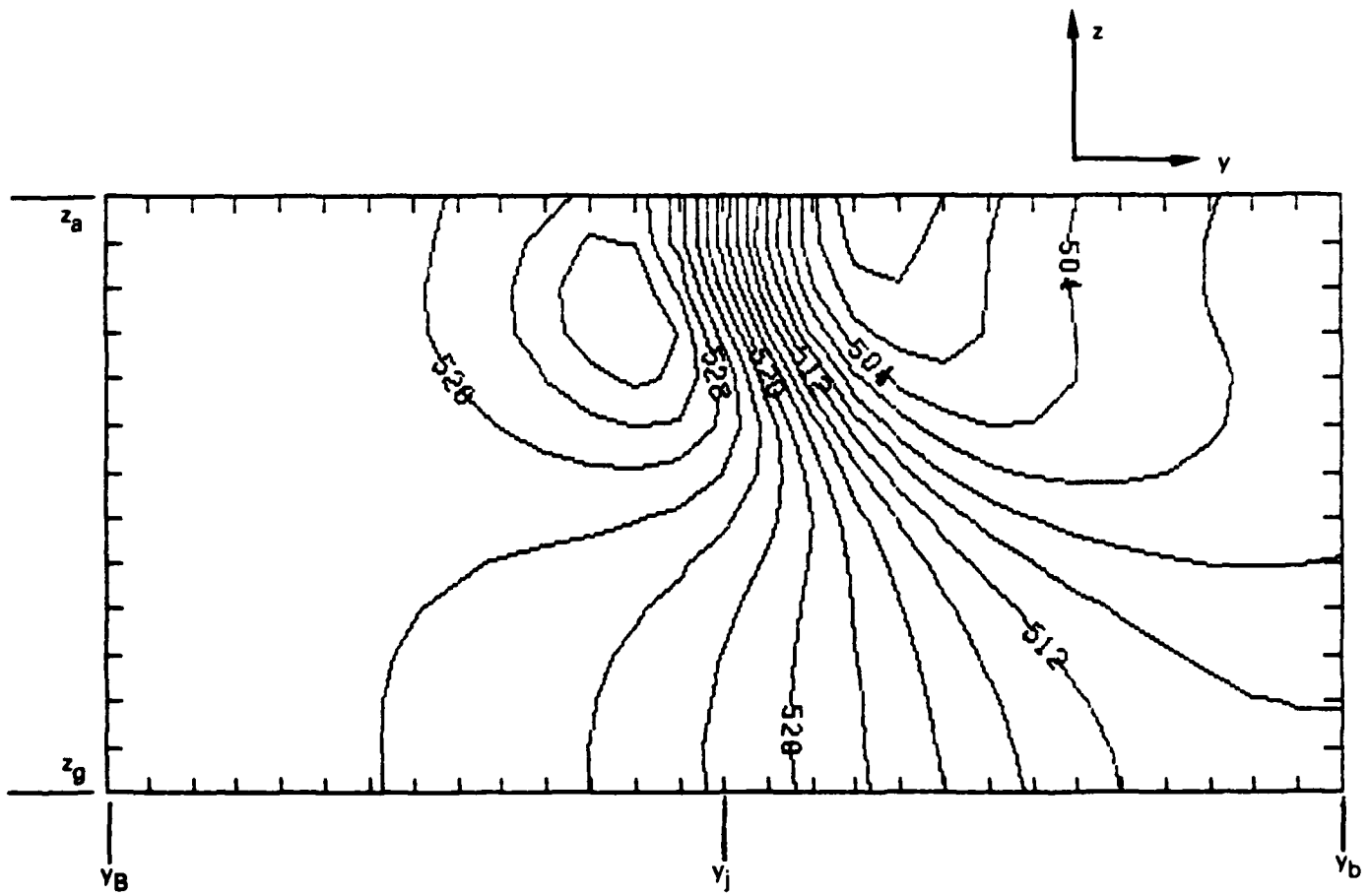


Figure 27. Example 3: Pressure Contours in the Plane  $x = x_j$

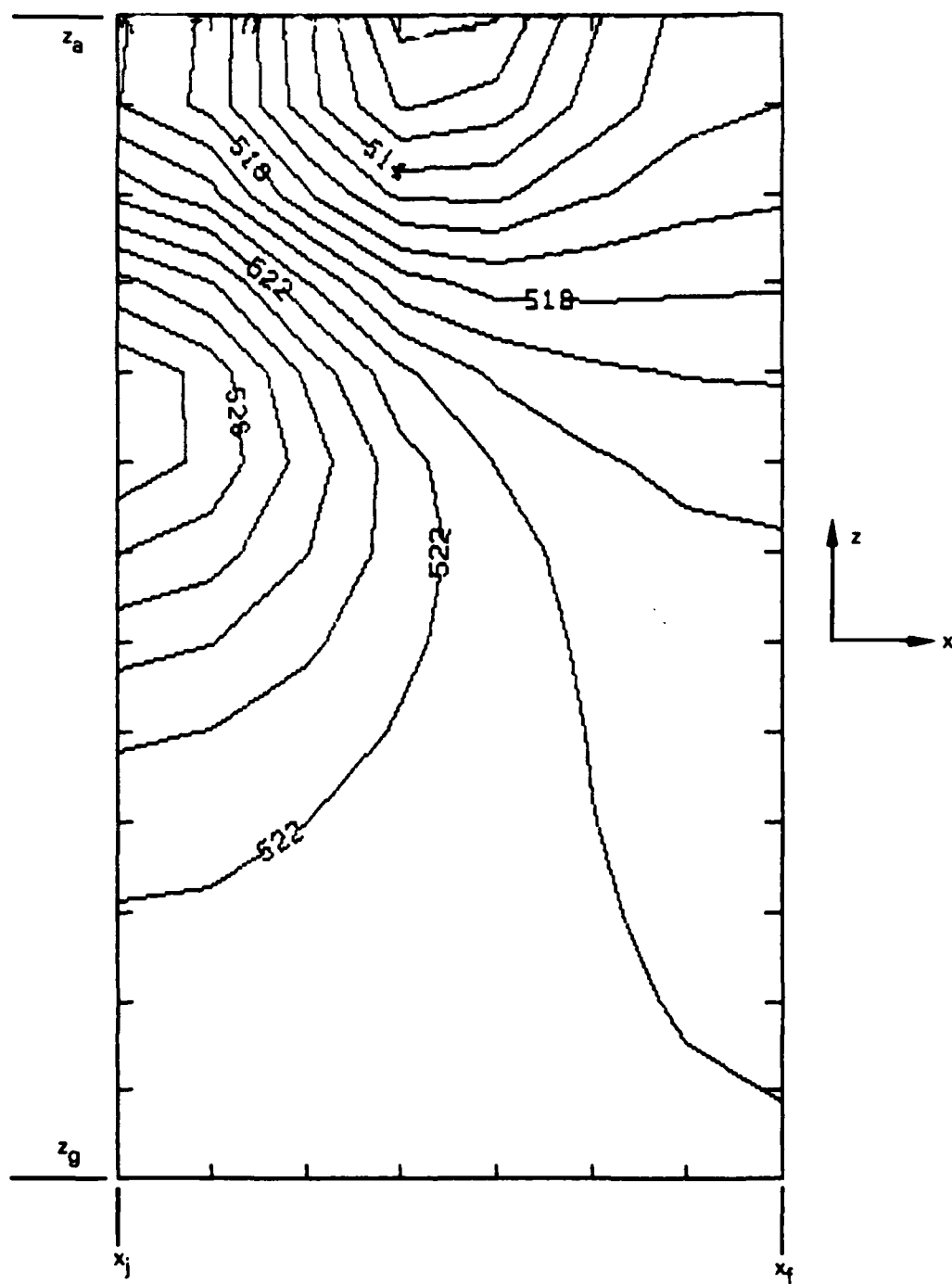


Figure 28. Example 3: Pressure Contours in the Plane  $y = y_j$

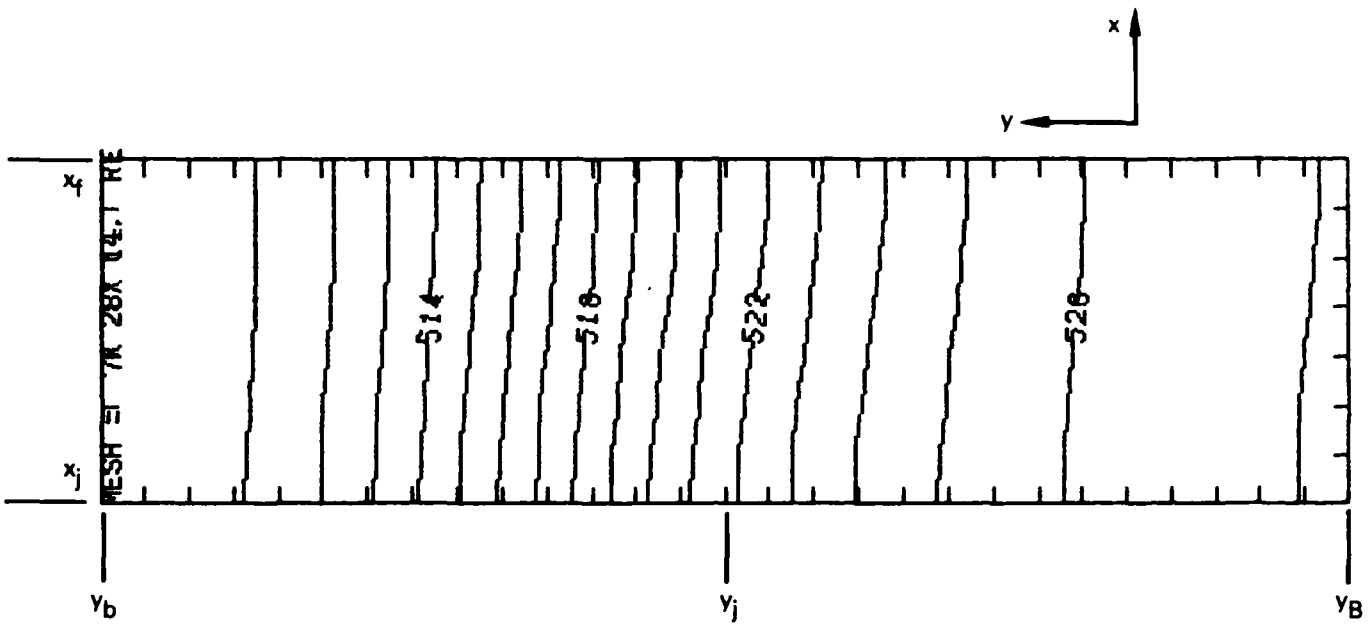


Figure 29. Example 3: Pressure Contours in the Plane  $z = z_g$

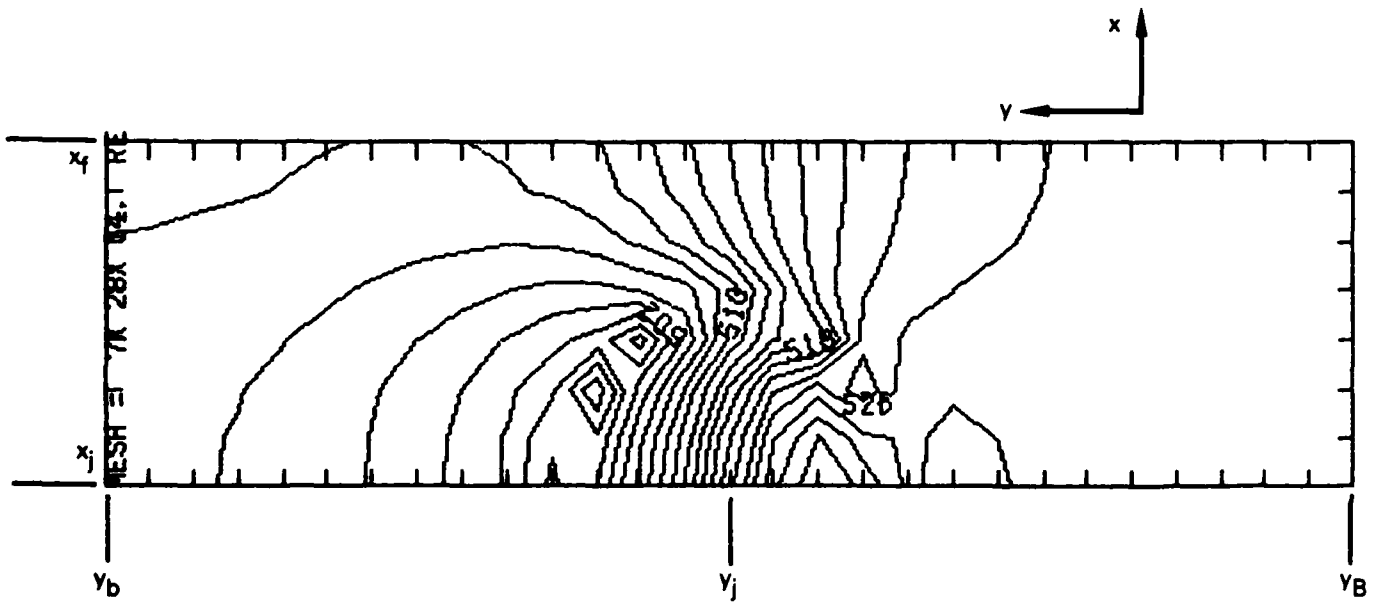


Figure 30. Example 3: Pressure Contours in the Plane  $z = z_a$

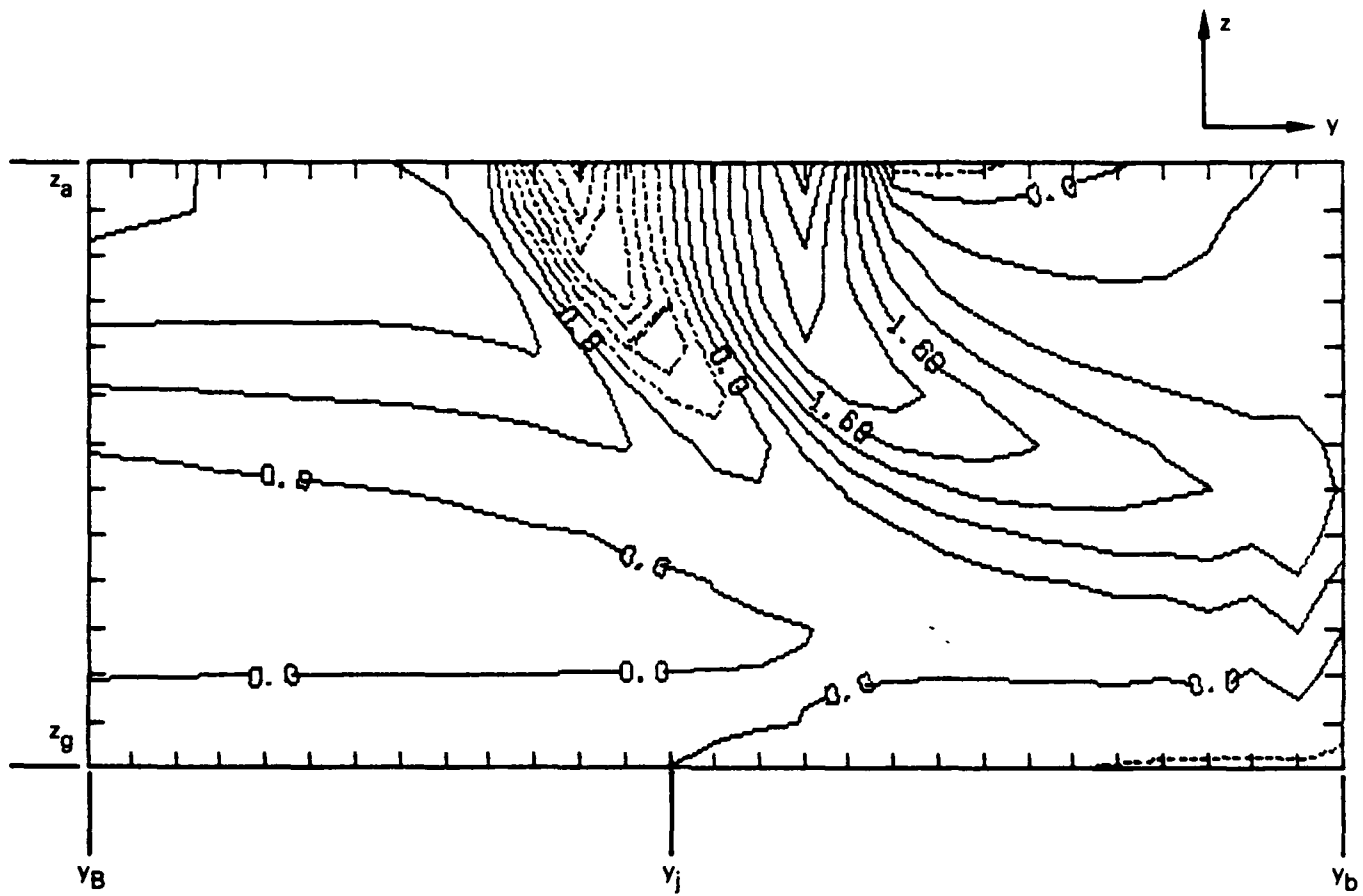


Figure 31. Example 3: x-Vorticity Component in the Plane  $x = x_j$

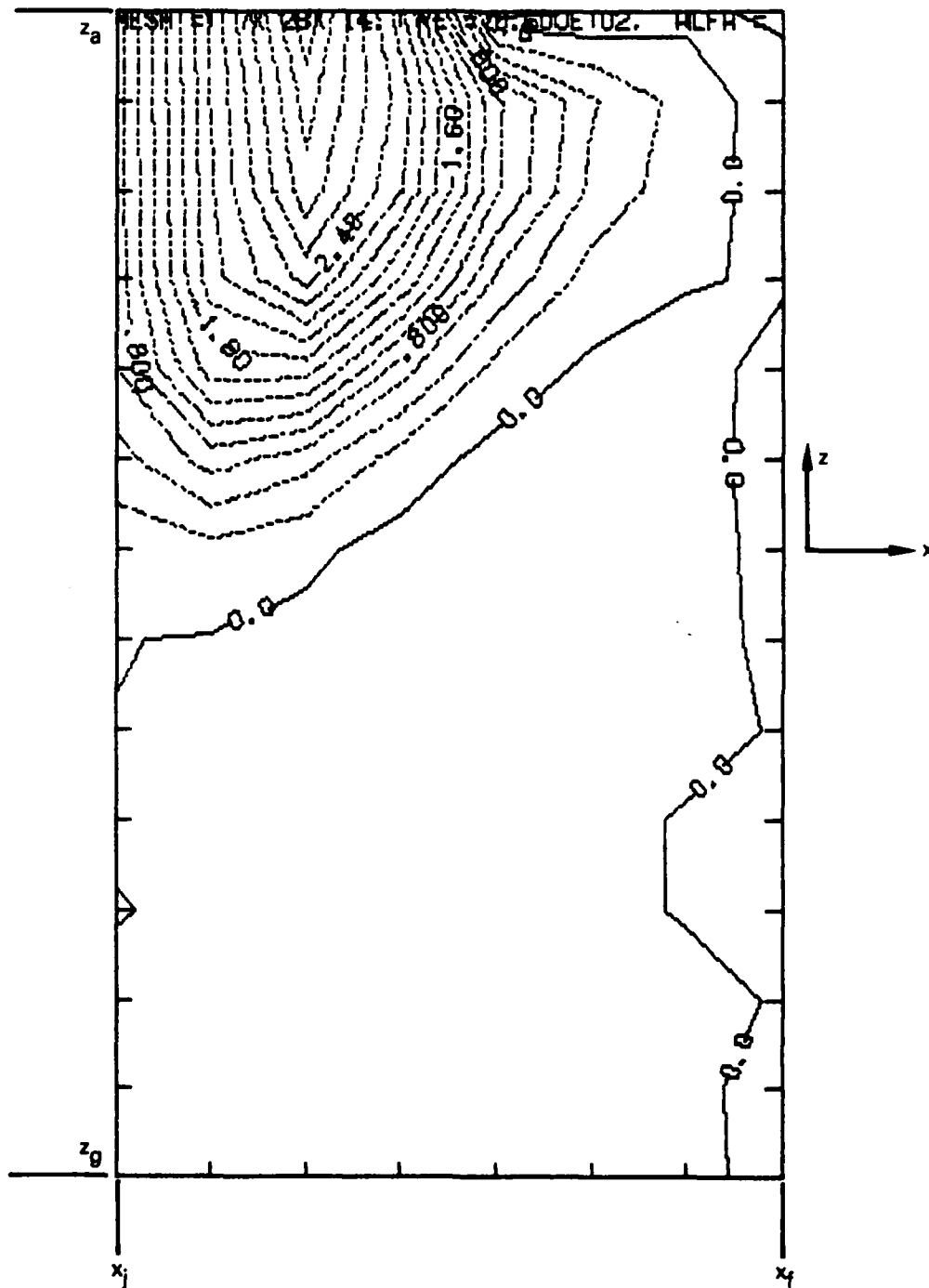


Figure 32. Example 3: y-Vorticity Component in the Plane  $y = y_j$

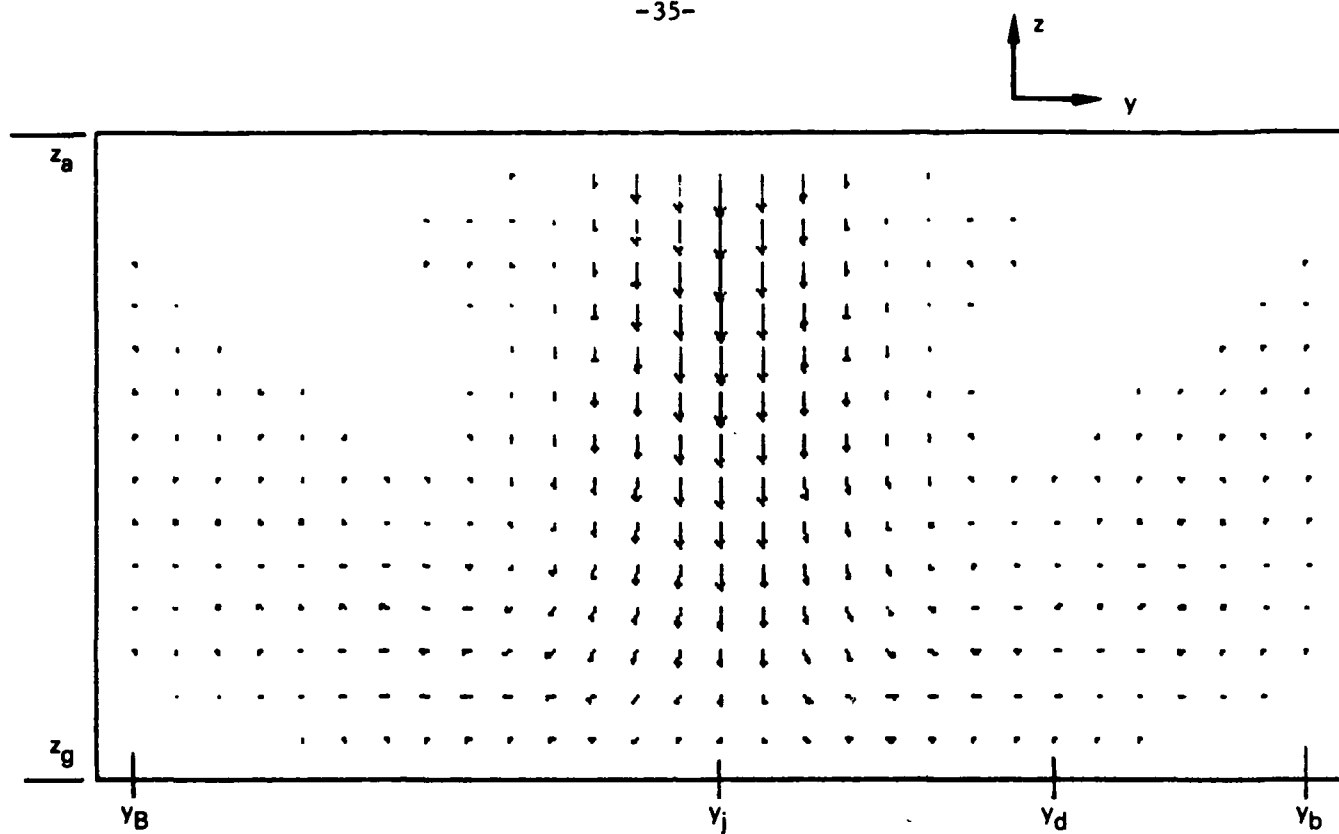


Figure 33. Example 4: Velocity Vectors in the Plane  $x = x_j$

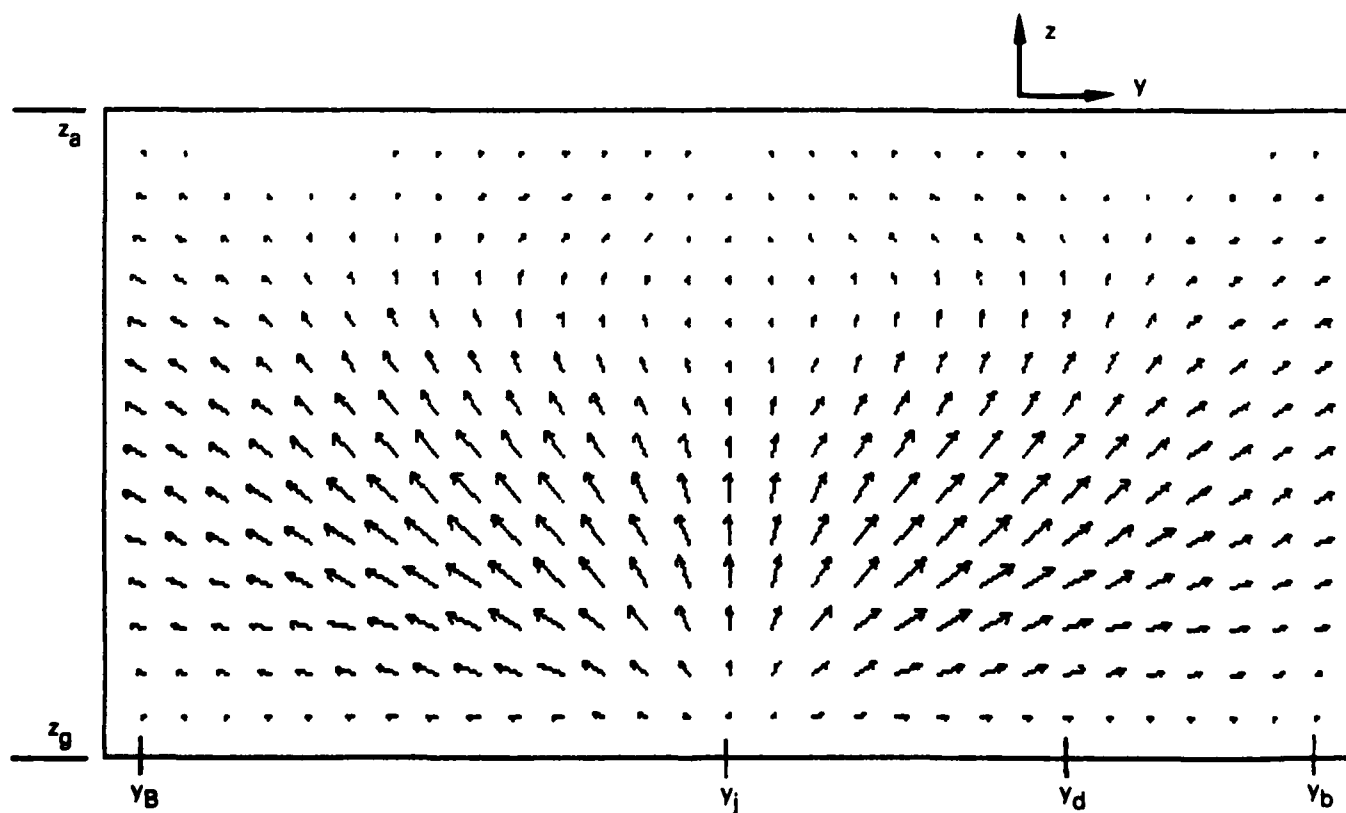


Figure 34. Example 4: Velocity Vectors in the Plane  $x = x_f$



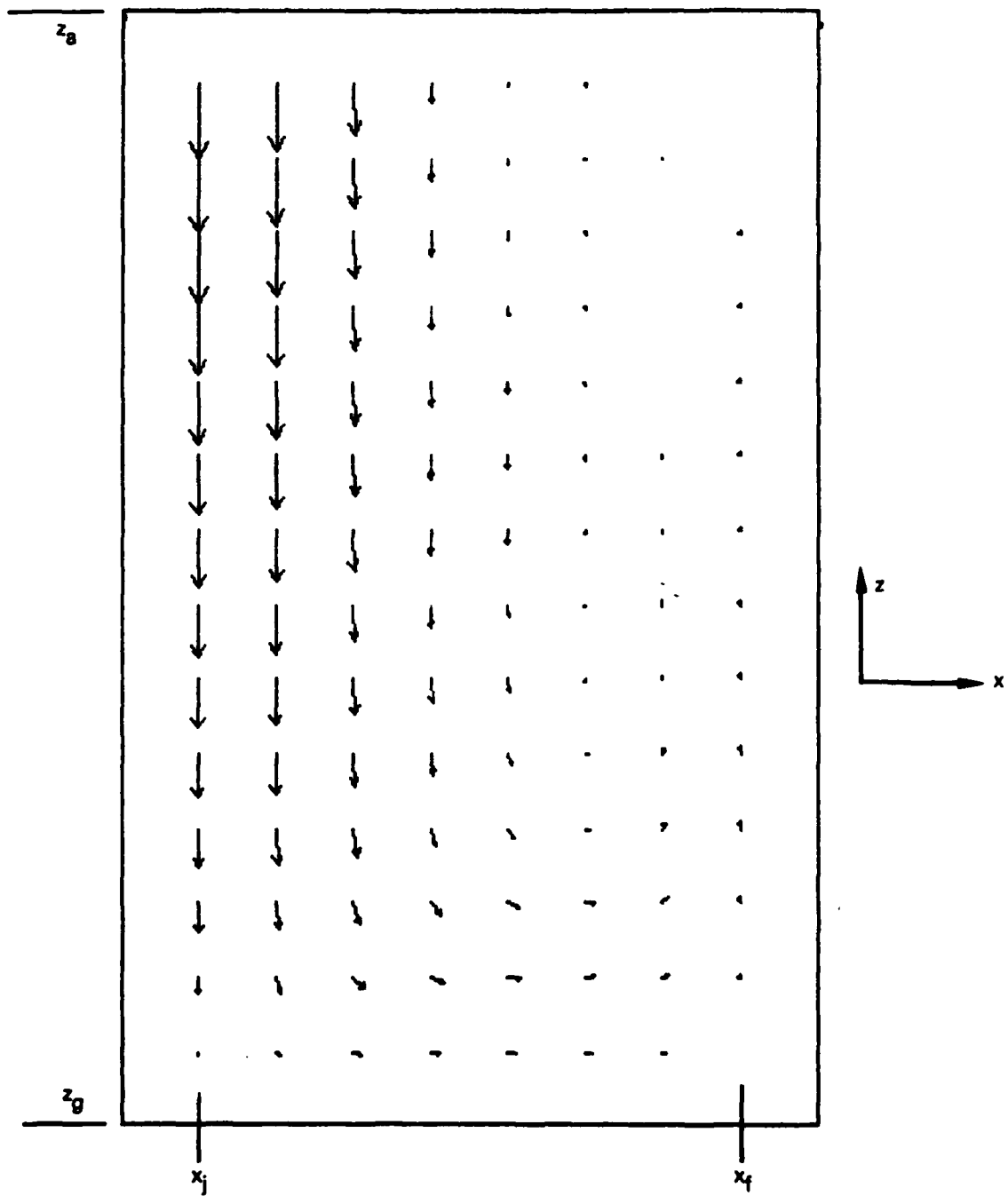


Figure 35. Example 4: Velocity Vectors in the Plane  $y = y_j$

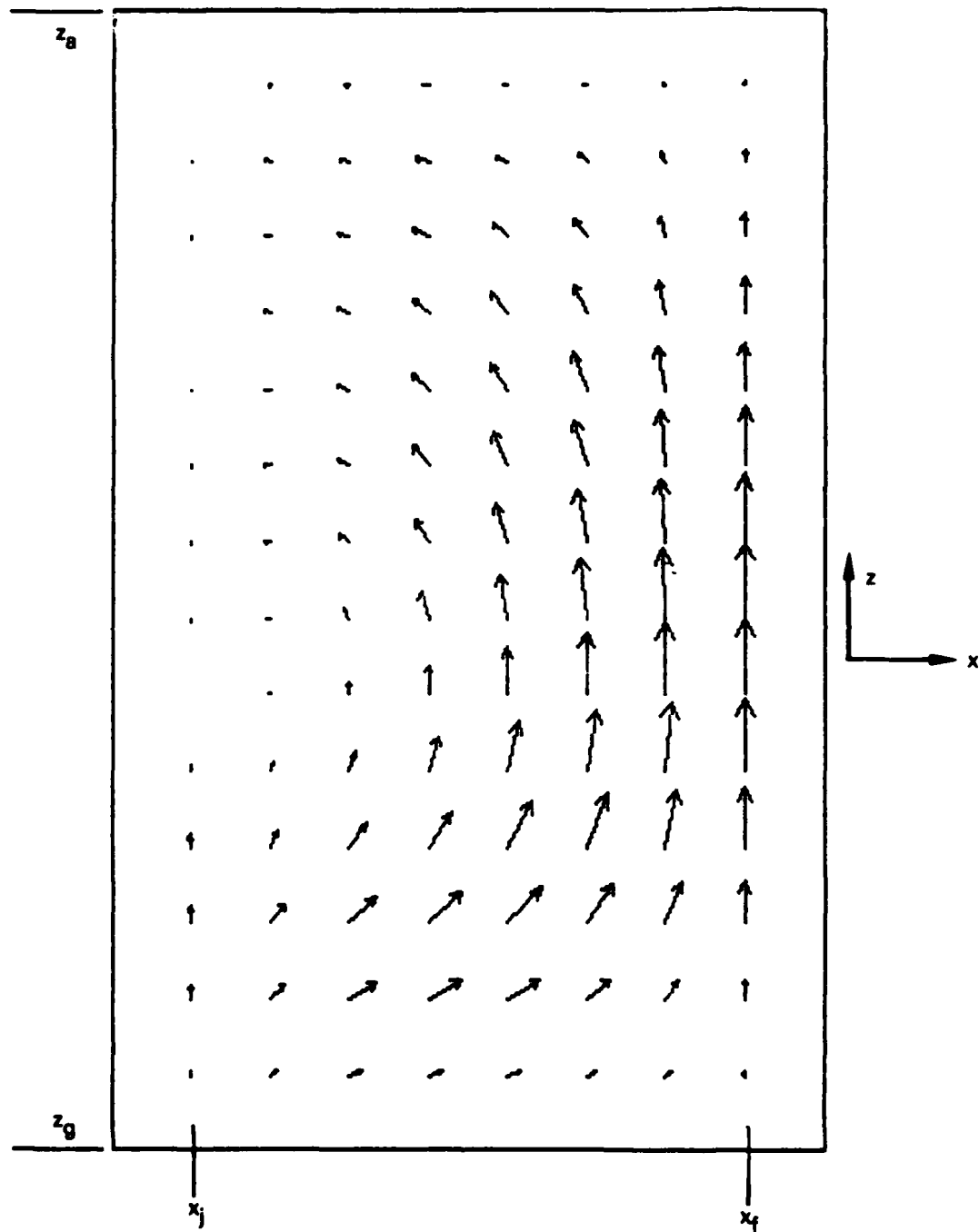


Figure 36. Example 4: Velocity Vectors in the Plane  $y = y_d$

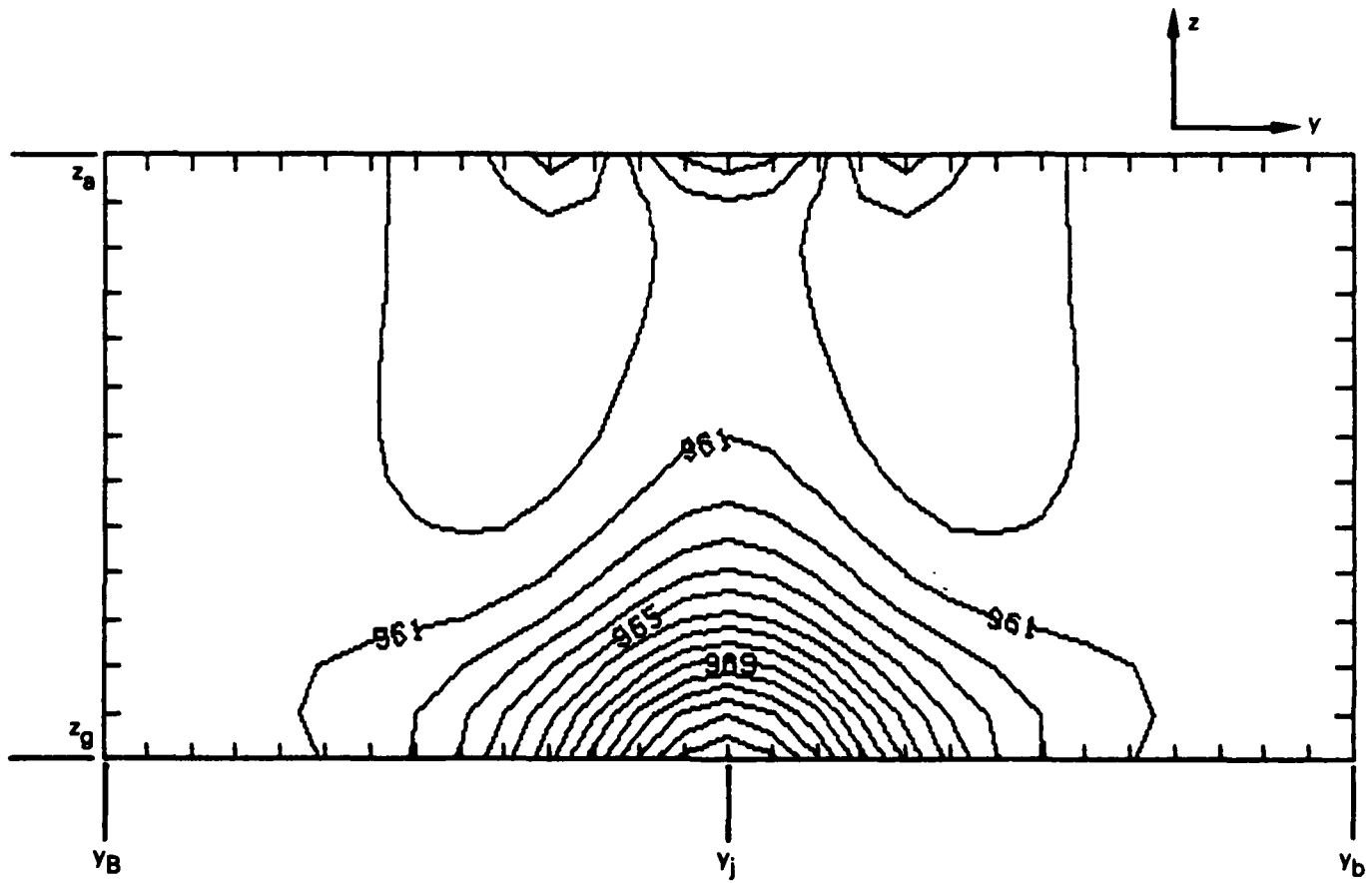


Figure 37. Example 4: Pressure Contours in the Plane  $x = x_j$

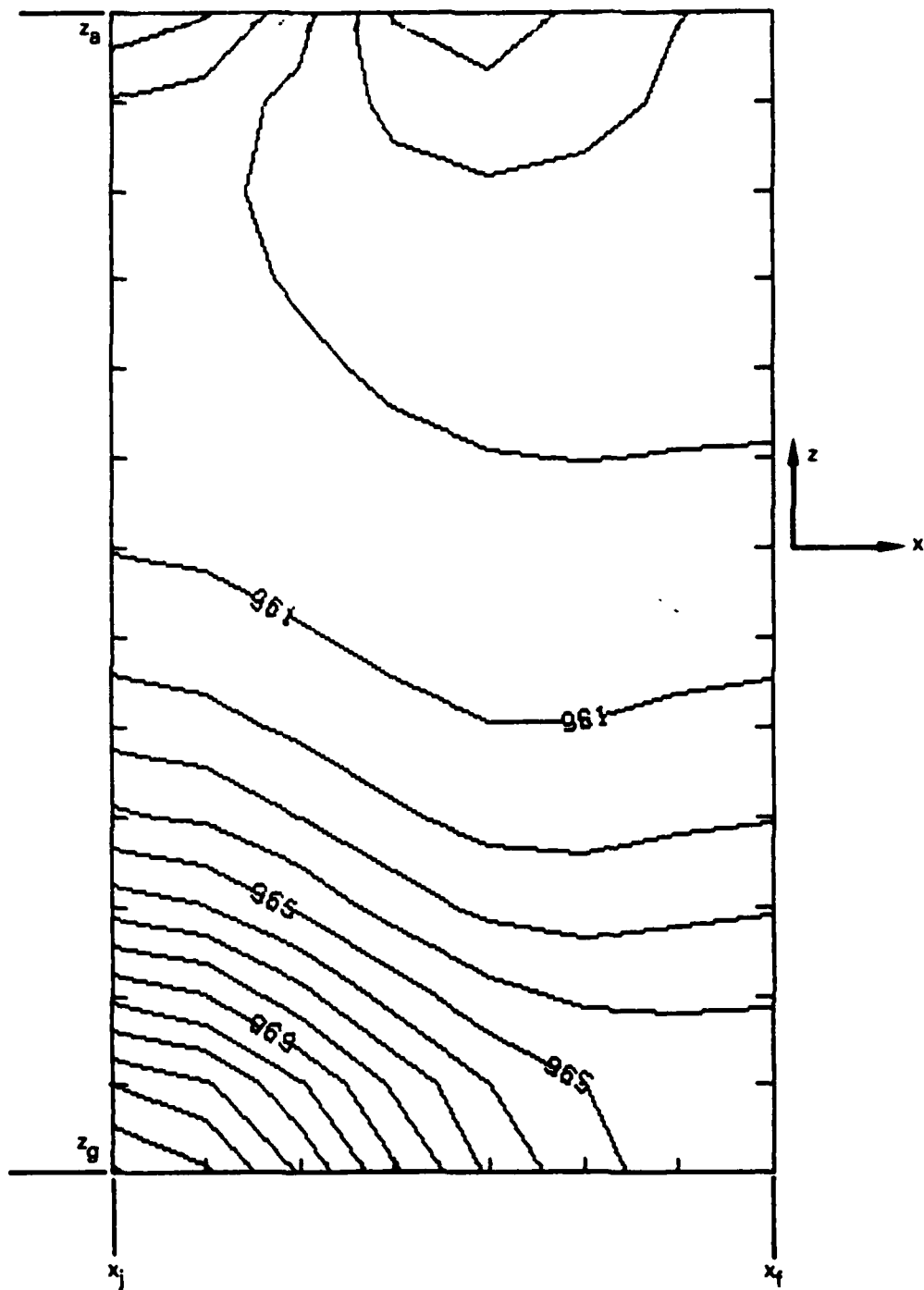


Figure 38. Example 4: Pressure Contours in the Plane  $y = y_j$

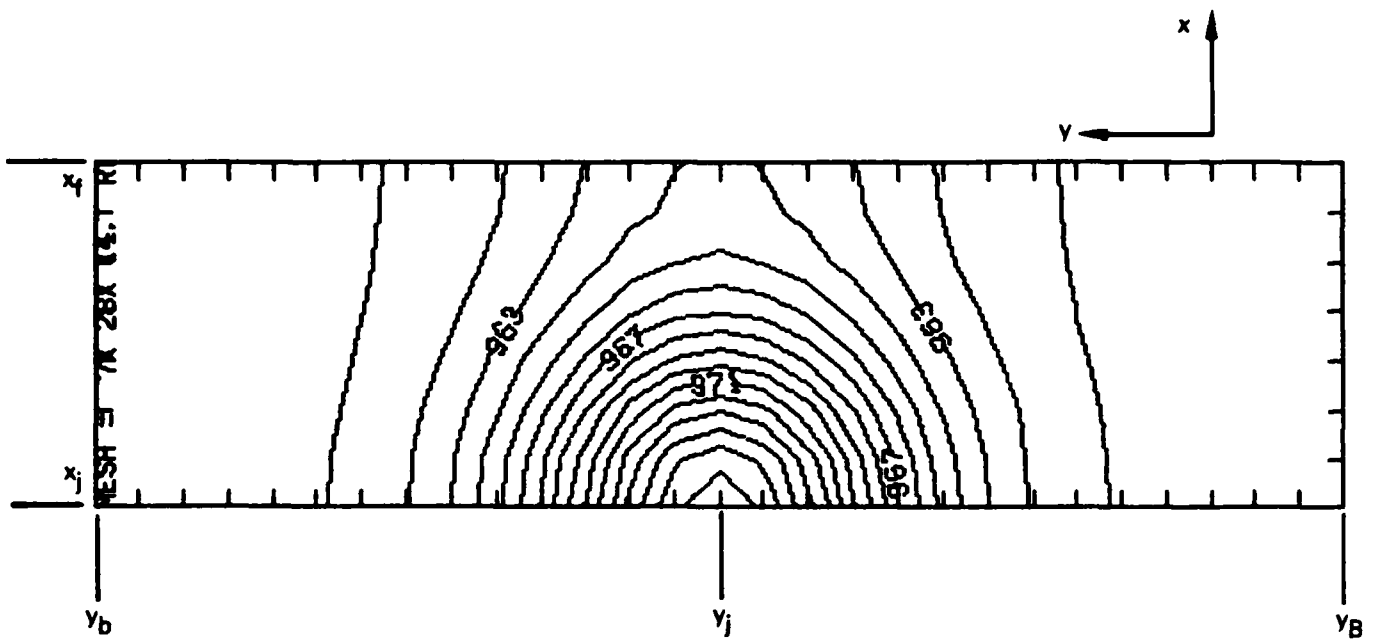


Figure 39. Example 4: Pressure contours in the Plane  $z = z_g$

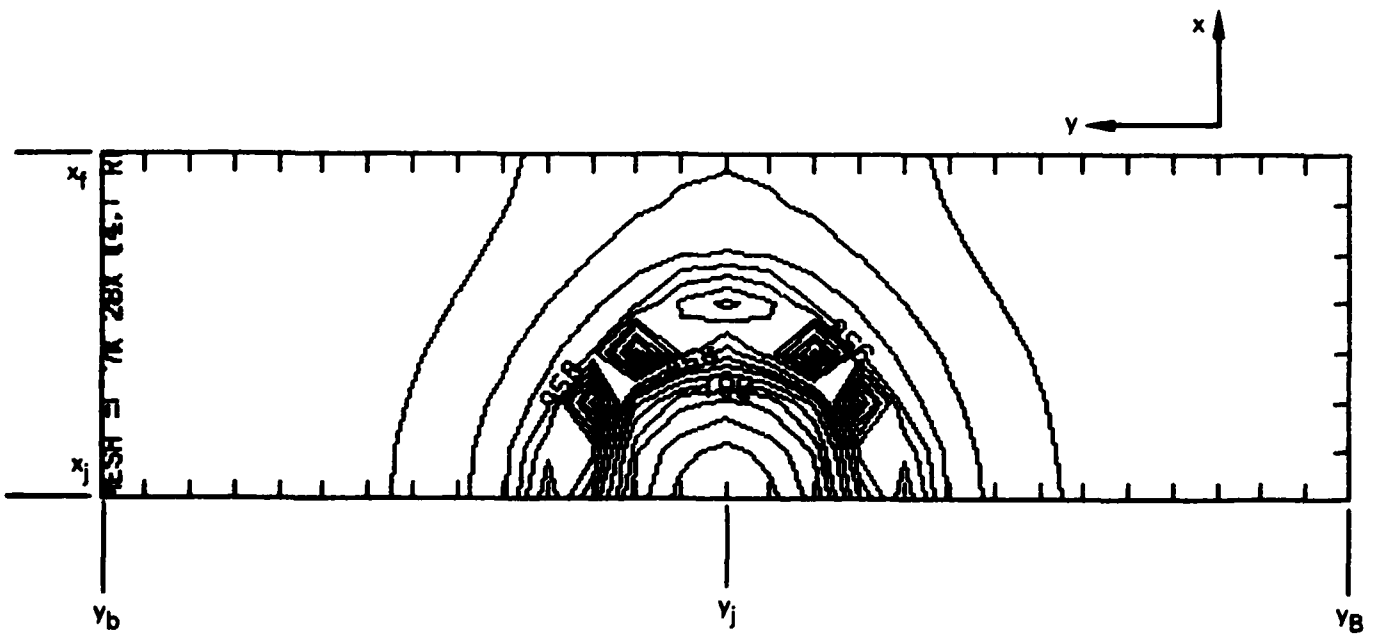


Figure 40. Example 4: Pressure Contours in the Plane  $z = z_g$

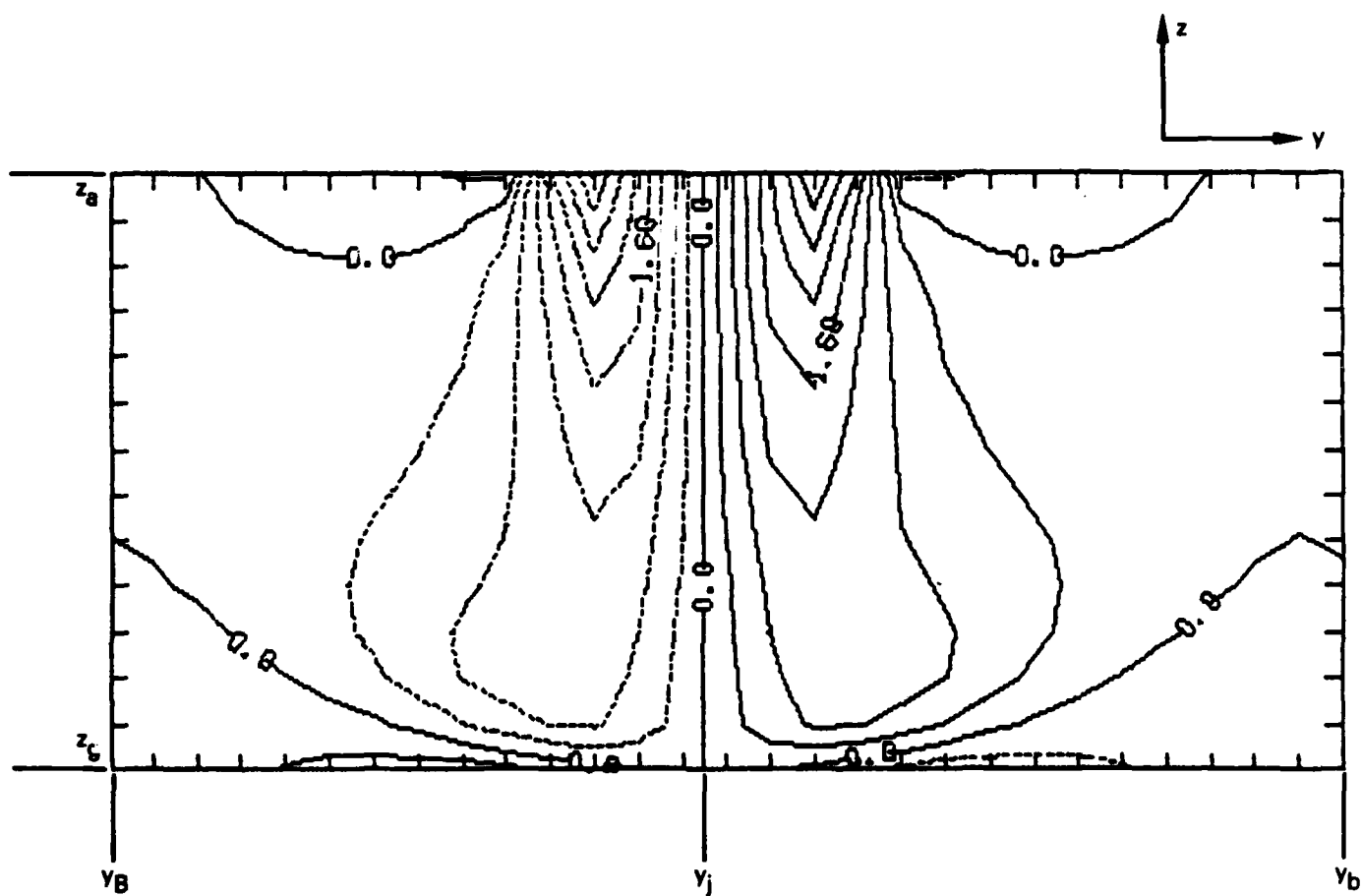


Figure 41. Example 4: x-Vorticity Component in the Plane  $x = x_j$

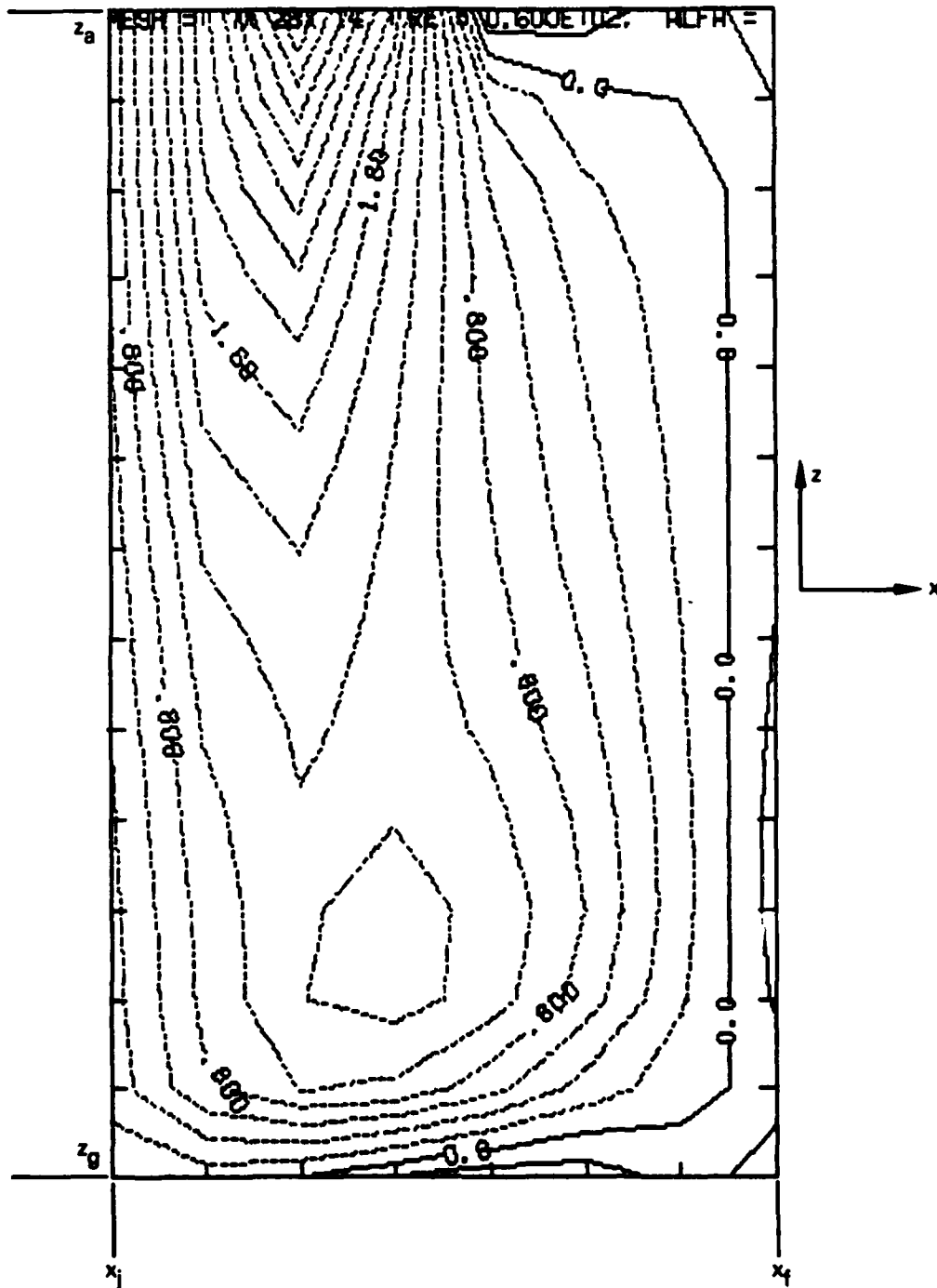


Figure 42. Example 4: y-Vorticity Component in the Plane  $y = y_j$

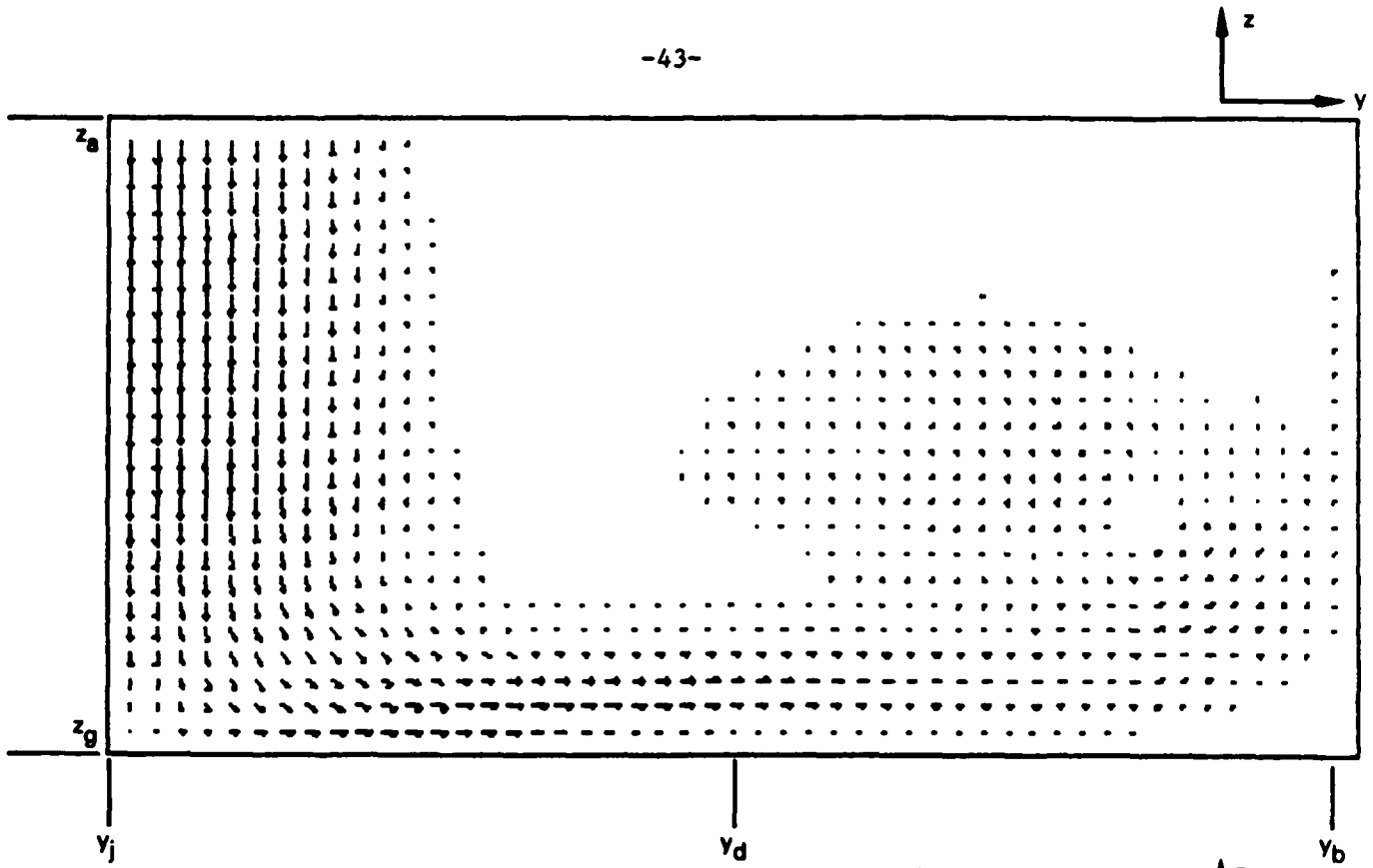


Figure 43. Example 5: Velocity Vectors in the Plane  $x = x_j$

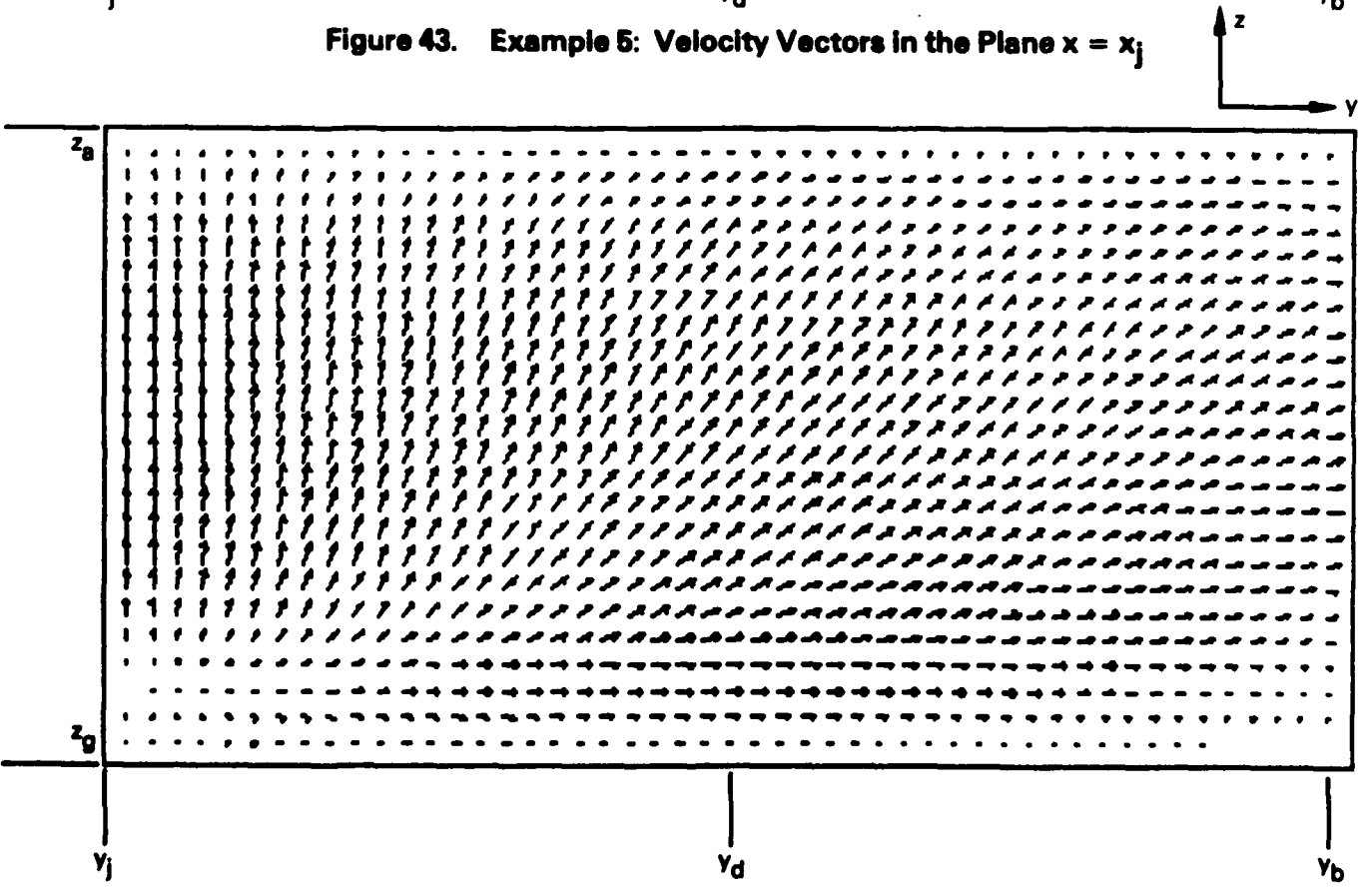


Figure 44. Example 5: Velocity Vectors in the Plane  $x = x_f$



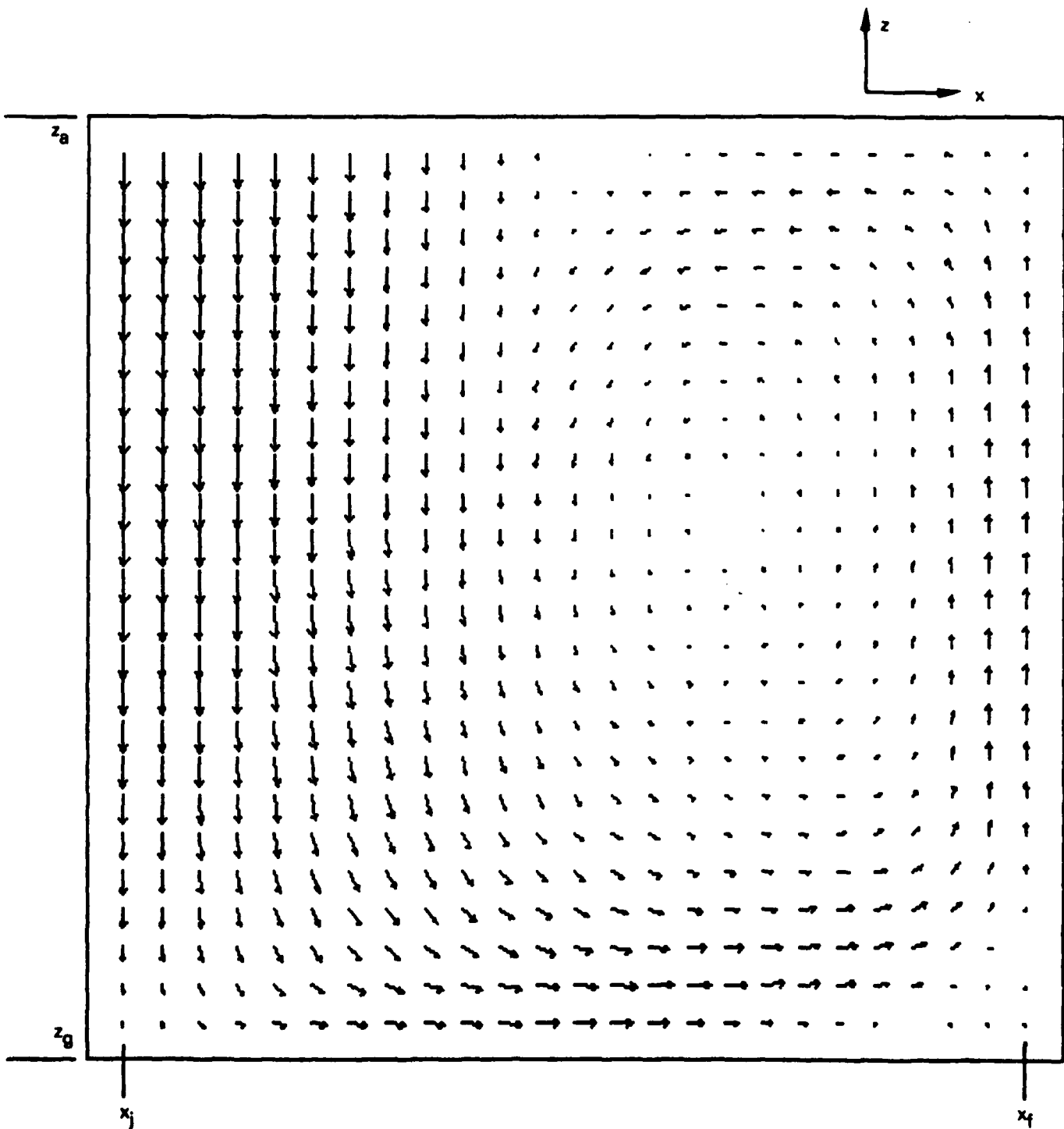


Figure 45. Example 5: Velocity Vectors in the Plane  $y = y_j$

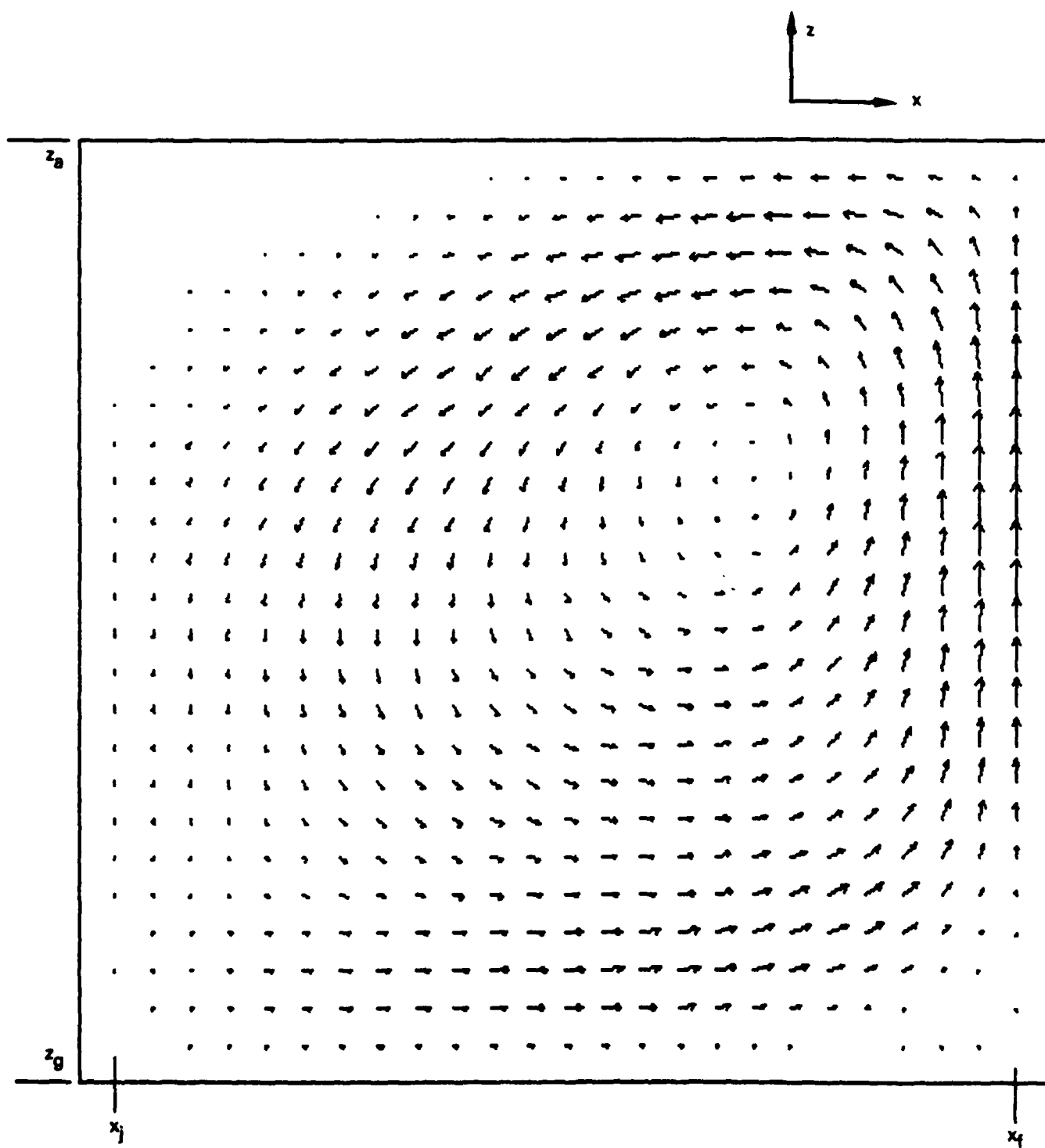
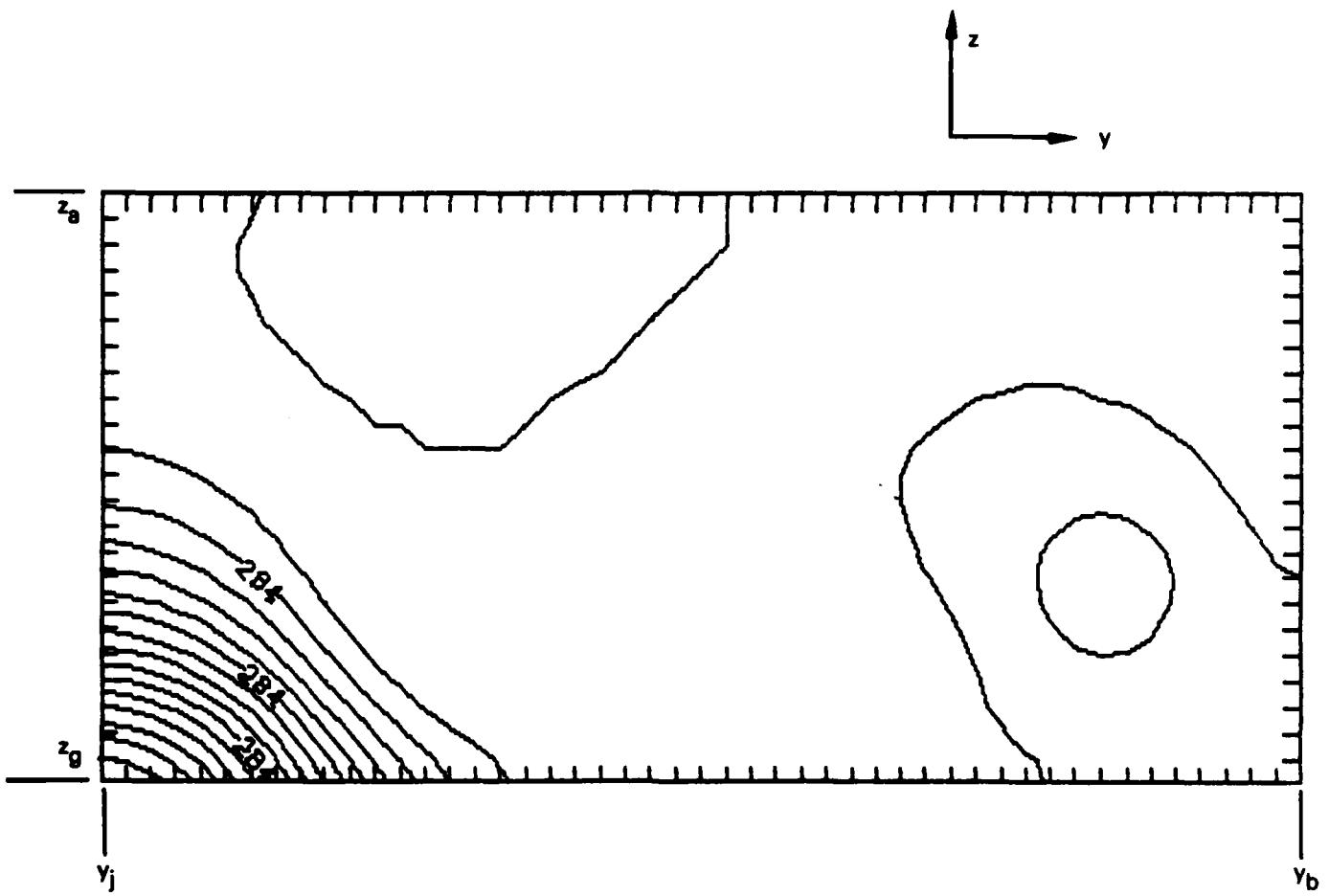
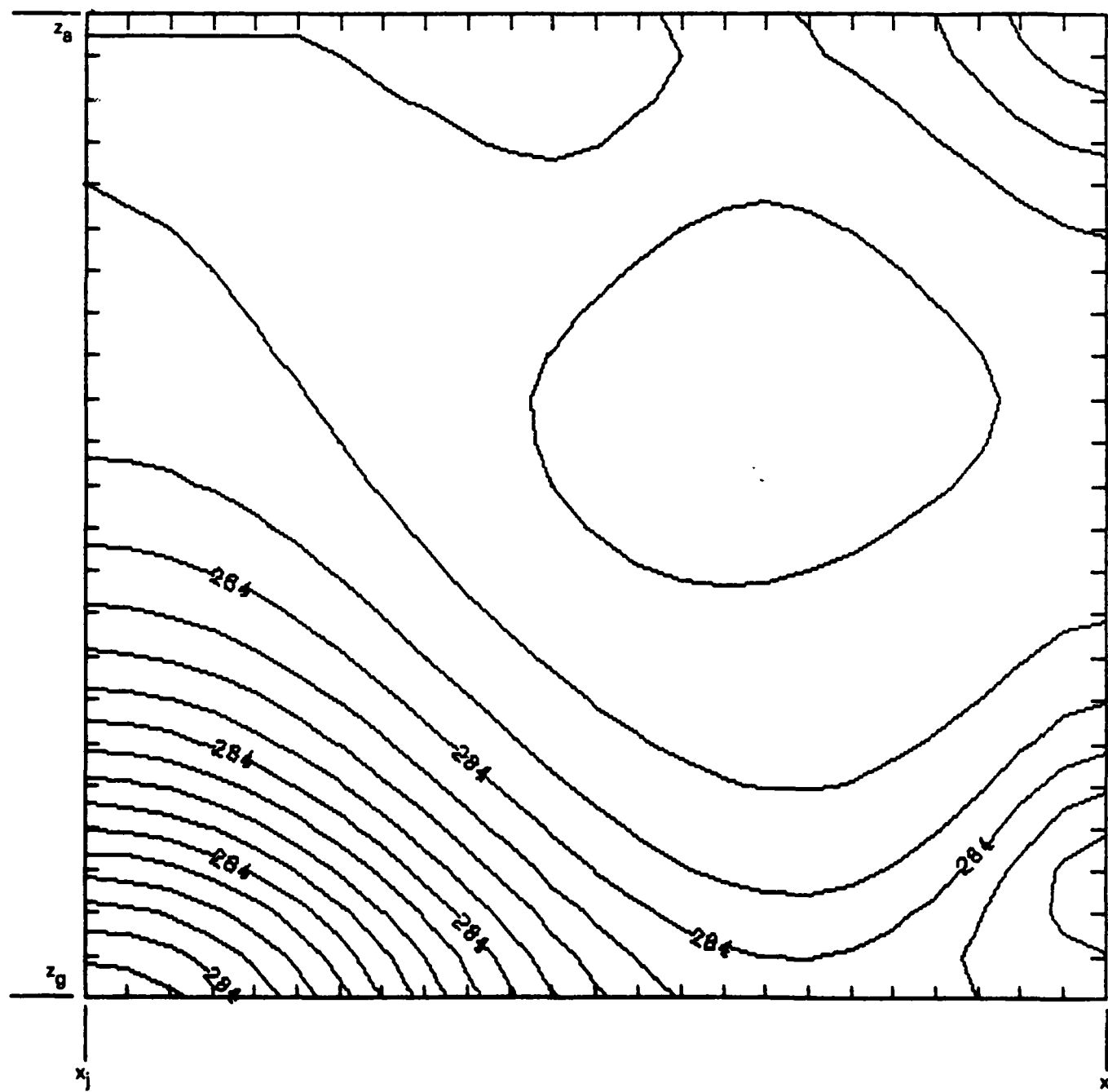


Figure 46. Example 5: Velocity Vectors in the Plane  $y = y_d$





**Figure 48. Example 5: Pressure Contours in the Plane  $y = y_j$**

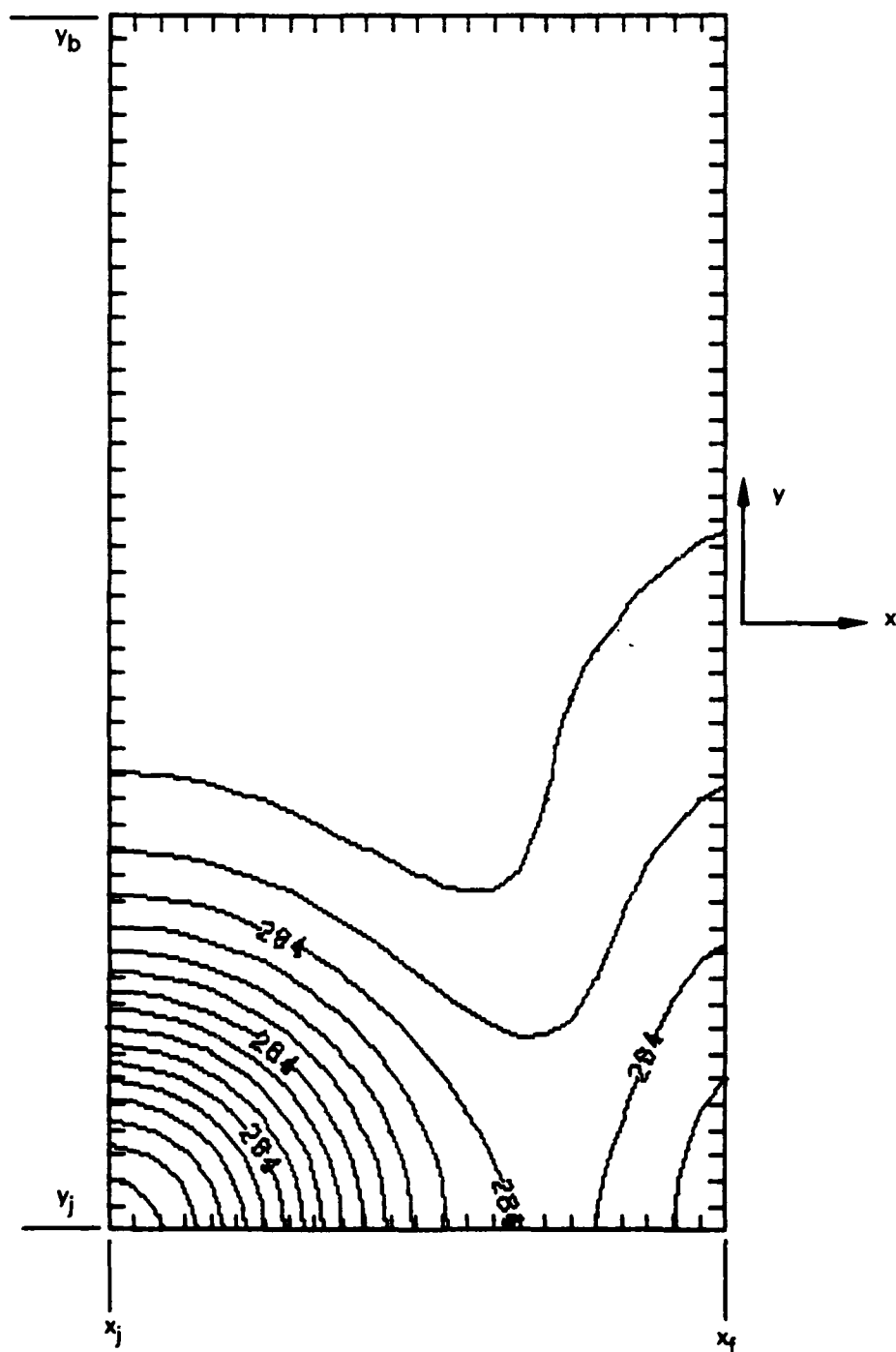


Figure 49. Example 5: Pressure Contours in the Plane  $z = z_a$

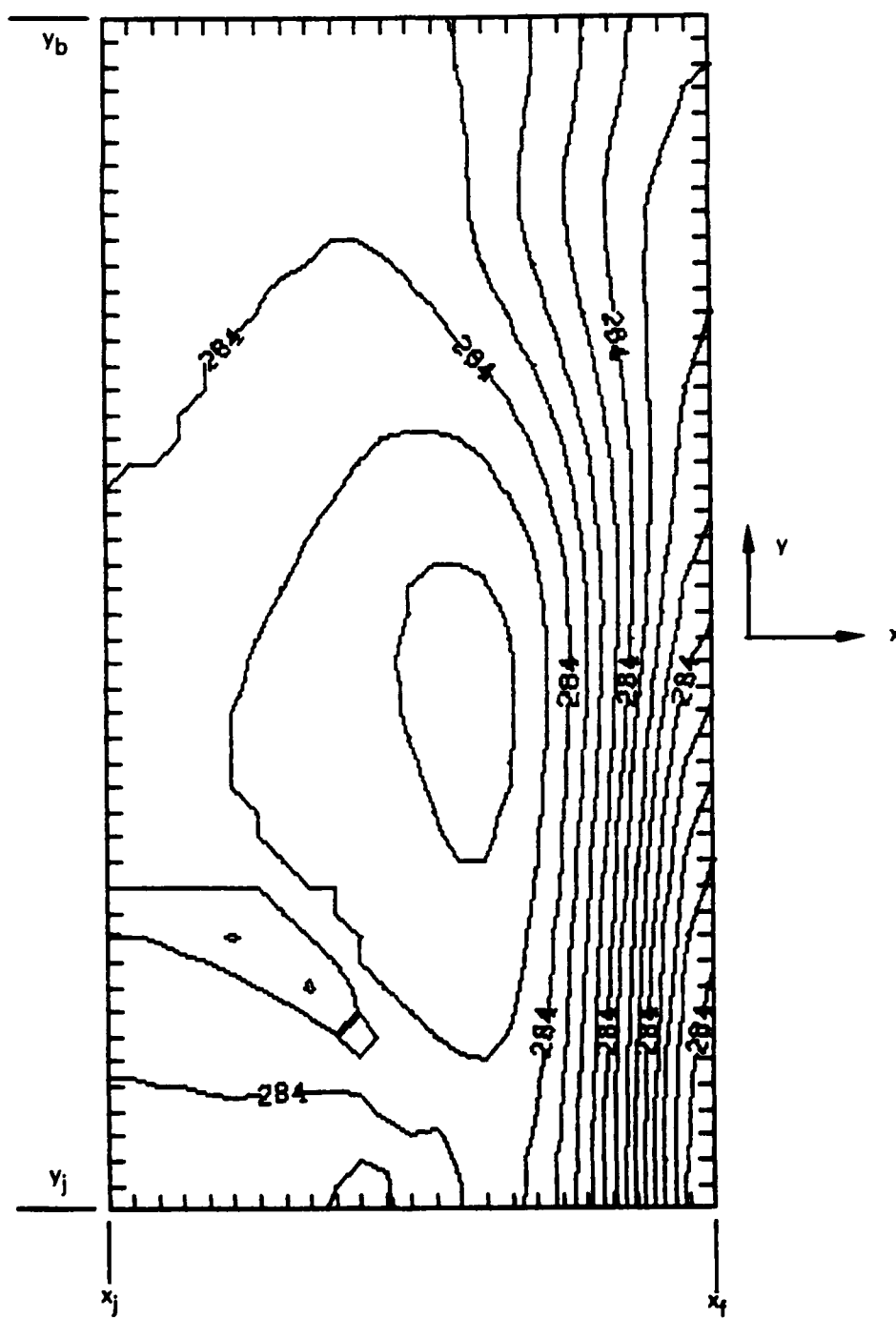


Figure 50. Example 5: Pressure Contours in the Plane  $z = z_a$



100

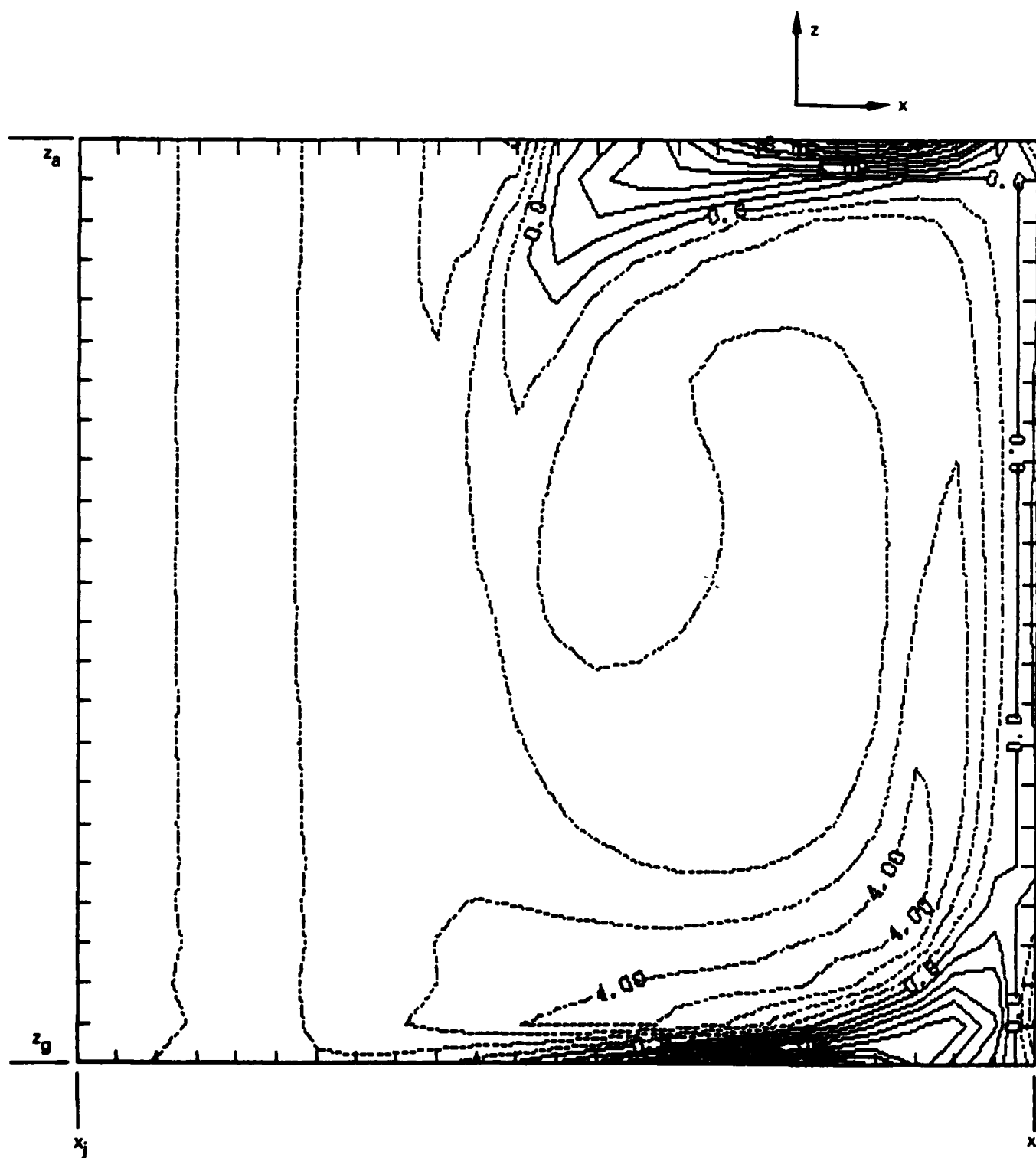


Figure 52. Example 5:  $y$ -Vorticity Component in the Plane  $y = y_j$



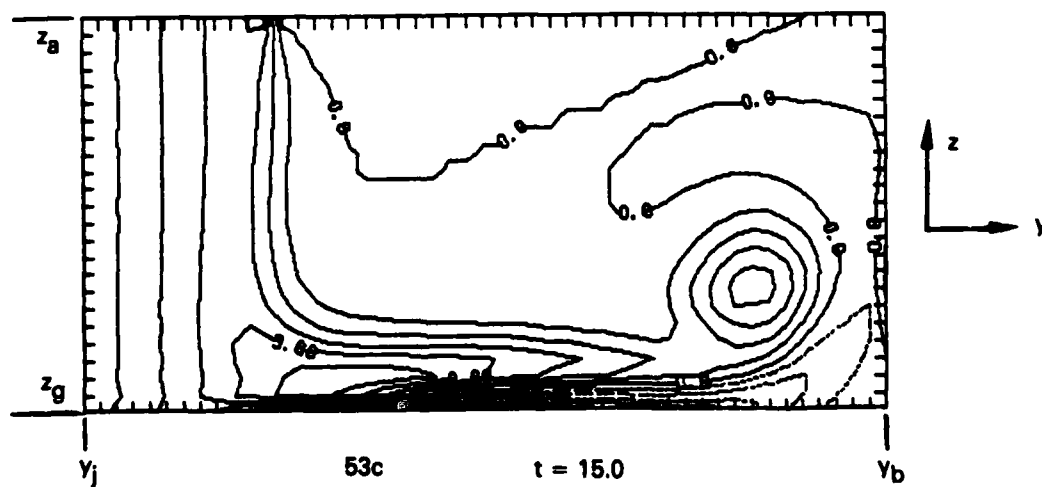
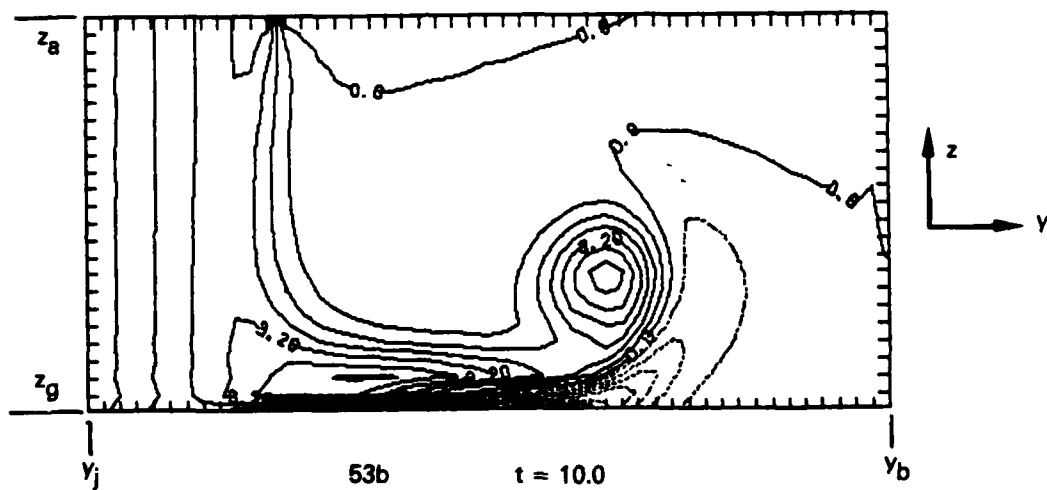
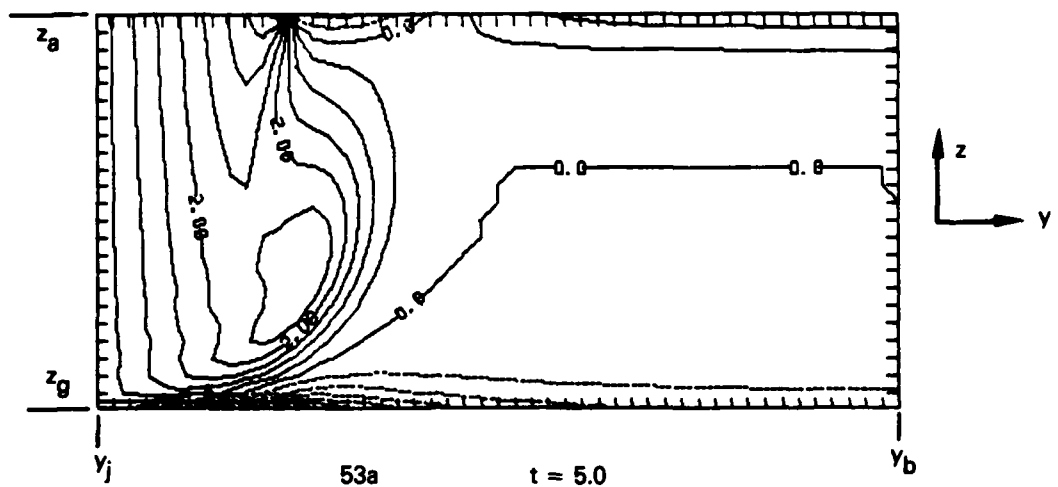


Figure 53. Initial Vortex Propagation in Example 5

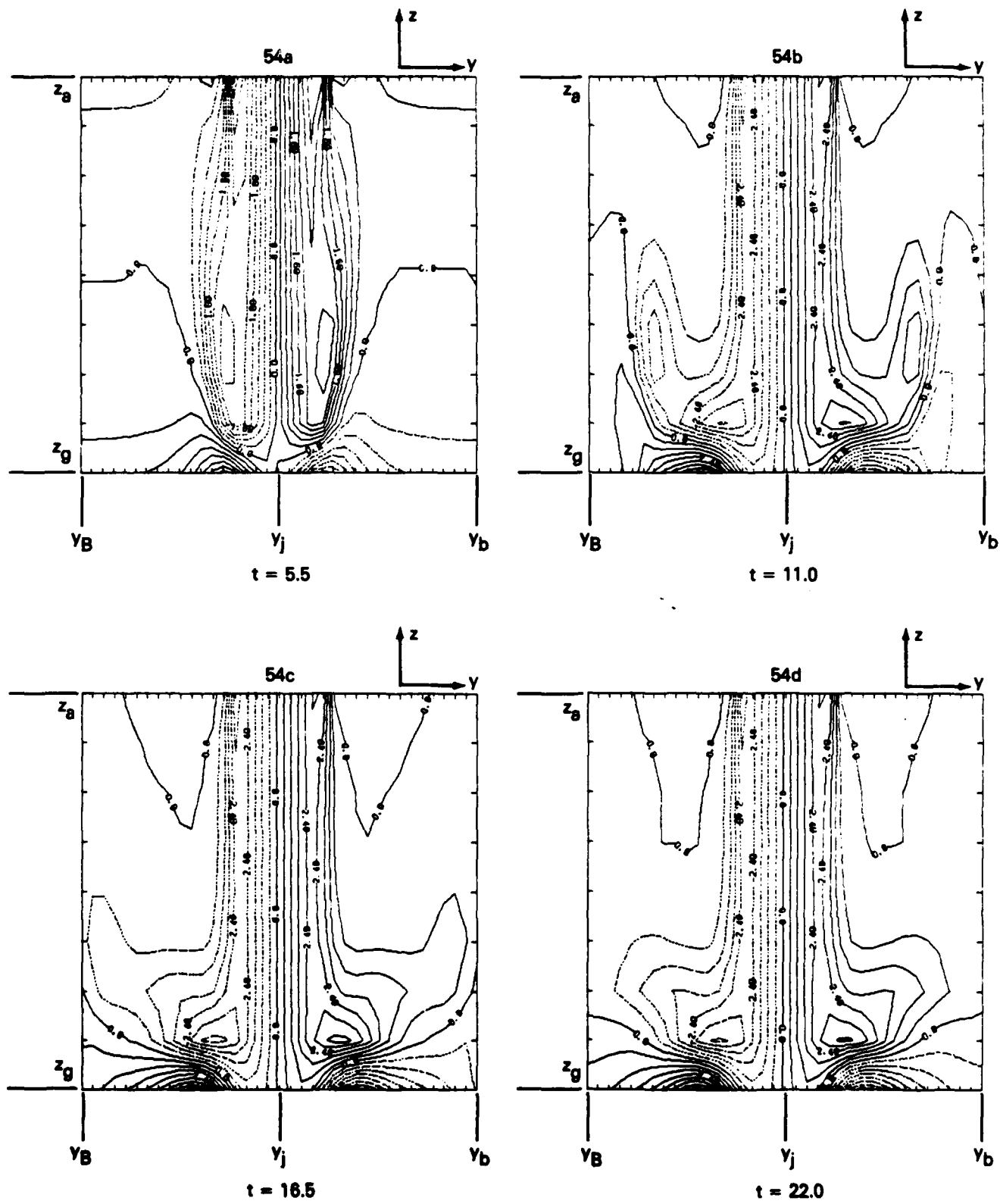


Figure 54. Initial Vortex Propagation in Example 1

**END**

**FILMED**

**2-85**

**DTIC**